

Supernova Remnants, Pulsar Wind Nebulae and Their Interaction

Cover: The Crab Nebula
in X-ray (*Chandra*), Optical (*VLT*), IR (*Keck*) and Radio (*VLA*).

© Copyright 2001 E. van der Swaluw

Printed by PrintPartners IPSkamp, Amsterdam

Alle rechten voorbehouden. Niets van deze uitgave mag worden verveelvoudigd, opgeslagen in een geautomatiseerd gegevensbestand, of openbaar gemaakt, in enige vorm, zonder schriftelijke toestemming van de auteur.

ISBN 90-393-2759-9

Supernova Remnants, Pulsar Wind Nebulae and Their Interaction

Supernova restanten, pulsar wind nevels
en hun interactie

met een samenvatting in het Nederlands

Proefschrift

ter verkrijging van de graad van doctor aan de Universiteit Utrecht
op gezag van de Rector Magnificus, Prof. Dr. W. H. Gispen,
ingevolge het besluit van het College voor Promoties
in het openbaar te verdedigen
op woensdag 6 juni 2001 des middags te 14.30 uur

door

Eric van der Swaluw

geboren op 4 augustus 1971 te 's-Hertogenbosch

Promotor: Prof. Dr. A. Achterberg
Sterrenkundig Instituut, Universiteit Utrecht

Contents

| | |
|---|-----------|
| 1 Pulsar Wind Nebulae and Supernova Remnants | 5 |
| 1.1 Introduction | 5 |
| 1.2 Observations of SNRs and PWNe | 7 |
| 1.2.1 Shell type remnants | 7 |
| 1.2.2 Plerionic type remnants | 11 |
| 1.2.3 Composite remnants | 12 |
| 1.3 The evolution of a supernova remnant | 15 |
| 1.3.1 The free expansion stage (duration 100 - 1,000 years) | 15 |
| 1.3.2 The Sedov stage (duration 10,000 years) | 15 |
| 1.3.3 The snowplow stage (duration 10,000-100,000 years) | 19 |
| 1.4 The evolution of a PWN inside a SNR | 22 |
| 1.4.1 The PWN in a SNR in the free expansion stage | 23 |
| 1.4.2 The PWN in a Sedov-stage remnant | 25 |
| 1.4.3 More advanced models of a PWN | 28 |
| 1.4.4 Excentric pulsars in SNRs | 31 |
| 1.4.5 Theory of bow shocks | 34 |
| 2 Hydrodynamical Modelling and Particle Acceleration | 41 |
| 2.1 Introduction | 41 |
| 2.2 Hydrodynamics | 41 |
| 2.2.1 Conservation laws for hydrodynamics | 41 |
| 2.2.2 Discretization of the conservation laws | 42 |
| 2.2.3 The Versatile Advection Code | 43 |
| 2.3 Particle Acceleration | 44 |
| 2.3.1 Introduction | 44 |
| 2.3.2 The transport equation | 45 |
| 2.3.3 Maximum energy | 47 |
| 2.3.4 Monte-Carlo Method | 49 |

| | | |
|----------|---|------------|
| 2.4 | Explicit schemes for shock acceleration | 51 |
| 2.5 | Implicit schemes for shock acceleration | 52 |
| 2.5.1 | test problem: acceleration by multiple shocks | 53 |
| 2.5.2 | Momentum-dependent diffusion | 56 |
| 2.6 | Towards multi-dimensional simulations | 58 |
| 2.6.1 | Practical limitations | 58 |
| 2.6.2 | Energy losses and the diffusion restriction | 59 |
| 3 | Pulsar Wind Nebulae in Supernova Remnants | 65 |
| 3.1 | Introduction | 66 |
| 3.2 | Pulsar Wind Nebula in a freely expanding Supernova Remnant . . | 67 |
| 3.3 | Pulsar Wind Nebula in a Sedov-Taylor remnant | 70 |
| 3.3.1 | The case of a constant wind luminosity | 70 |
| 3.3.2 | The case of a varying wind luminosity | 77 |
| 3.4 | Numerical simulations | 78 |
| 3.4.1 | Method | 78 |
| 3.4.2 | Evolution of the PWN-SNR system into the Sedov phase | 82 |
| 3.4.3 | The influence of reverse-shock reverberations | 82 |
| 3.4.4 | Subsonic expansion stage | 84 |
| 3.5 | Conclusions and discussion | 84 |
| 4 | Interaction of high-velocity Pulsars with old Supernova Remnants | 89 |
| 4.1 | Introduction | 90 |
| 4.2 | Physics of a PWN bow shock inside a SNR | 91 |
| 4.2.1 | Dynamics of the pulsar/SNR system | 91 |
| 4.2.2 | Pulsar Wind | 94 |
| 4.3 | Hydrodynamics of the PWN bow shock | 96 |
| 4.3.1 | Simulation Method | 96 |
| 4.3.2 | Starting a pulsar wind | 96 |
| 4.3.3 | Steady PWN and bow shock in a uniform medium | 97 |
| 4.3.4 | Interaction of the PWN with a shock | 101 |
| 4.4 | Conclusions | 105 |
| 5 | Non-thermal X-Ray Emission from young Supernova Remnants | 109 |
| 5.1 | Introduction | 110 |
| 5.2 | Particle acceleration at SNR blastwaves | 112 |
| 5.2.1 | SNR evolution | 112 |
| 5.2.2 | Shock acceleration | 113 |

| | | |
|----------|---|------------|
| 5.2.3 | Typical electron and photon energies | 115 |
| 5.3 | Simulation method | 118 |
| 5.3.1 | SNR Hydrodynamics | 118 |
| 5.3.2 | Magnetic fields | 120 |
| 5.3.3 | Energetic particles | 122 |
| 5.4 | Simulation results | 124 |
| 5.5 | Discussion and conclusions | 130 |
| 6 | Rejuvenating Shells of Supernova Remnants by Pulsar Winds | 133 |
| 6.1 | Introduction | 134 |
| 6.2 | Rejuvenation | 135 |
| 6.2.1 | Diffusion of radio electrons | 137 |
| 6.3 | Comparison with observations | 139 |
| 6.3.1 | CTB80 and PSR 1951+32 | 140 |
| 6.3.2 | G5.4-1.2 and PSR B1757-24 | 140 |
| 6.3.3 | G341.2+0.9 and PSR 1643-43 | 140 |
| 6.4 | Numerical Simulations | 142 |
| 6.5 | Discussion | 145 |
| 7 | Inferring Initial Spin Periods for Neutron Stars in Composite Remnants | 151 |
| 7.1 | Introduction | 152 |
| 7.2 | Evolution of a PWN in a SNR | 153 |
| 7.2.1 | Analytical Relations | 154 |
| 7.2.2 | Hydrodynamical Simulations | 155 |
| 7.3 | Inferring Initial Spin Rates | 156 |
| 7.4 | Discussion | 158 |
| 8 | Nederlandse Samenvatting | 167 |
| 8.1 | Supernova's en supernova restanten | 167 |
| 8.2 | Pulsars en pulsar winden | 168 |
| 8.3 | De interactie tussen een pulsar wind nevel en een supernova restant | 168 |
| 8.4 | Supernova restanten: kosmische deeltjesversnellers | 169 |
| 8.5 | Ter afsluiting | 170 |
| | Curriculum Vitae | 171 |
| | Dankwoord | 173 |

Chapter 1

Pulsar Wind Nebulae and Supernova Remnants

1.1 Introduction

Supernovae are one of the most energetic explosive events in our Galaxy and other galaxies. These events take place when massive stars end their life. The stellar core collapses and they blow off their outer layers. The only thing which remains of the exploded star is a high density neutron star, which may manifest itself as a pulsar, or possibly a black hole. If the supernova explosion is asymmetric, the pulsar must gain a velocity to conserve total momentum. This thesis will deal with phenomena that take place after the supernova explosion. Another mechanism which can cause a supernova explosion is the disruption of a white dwarf in a binary. These explosions will however not result in a neutron star, therefore we will not consider these events in this thesis.

In the supernova explosion there is an energy release of roughly 10^{53} erg; 99% of this energy is radiated away in the form of neutrinos. This means that the total *mechanical* energy of the supernova remnant(SNR) is about 10^{51} erg. This mechanical energy provides the kinetic energy of the SNR expansion and the thermal energy of the SNR interior.

The expansion of the SNR can be divided in four stages (Woltjer 1972). In this chapter we will discuss all these different stages. We will also discuss the case when a pulsar wind is embedded within the interior of the SNR.

In the first stage, the *free expansion stage*, the mass of the SNR essentially consists of the ejected mass, M_{ej} , of the progenitor star. These ejecta expand freely, where the expansion rate is controlled by the conservation of the kinetic energy. The expansion speed exceeds the sound speed of the interstellar medium (ISM) and a shock will be formed. During the expansion, the SNR will sweep up matter from the ISM, leading to an increase of the mass of the SNR. It will not be long before the swept-up mass $M(t)$ exceeds the ejected mass M_{ej} . From this point on the expanding SNR is described by the Sedov solution (Sedov 1959).

In contrast to the free expansion stage, which lasts only ~ 100 -1,000 years, the Sedov stage lasts much longer, around $\sim 10,000$ years. In this stage of the SNR expansion the ram pressure of the swept-up material is balanced by the internal pressure. The expansion rate is controlled, as before, by energy conservation: radiation losses can still be neglected.

Ultimately the total mechanical energy of the SNR decreases due to significant radiation losses. At this point the shell of swept-up interstellar gas will cool down and will be driven through the ISM by the pressure of the interior of the SNR. This stage is called the pressure-driven snowplow stage. This stage is followed by the momentum-conserving snowplow stage, when the pressure of the interior of the SNR becomes comparable with the pressure of the ISM: the SNR will start merging with the ISM.

For those SNRs which contain a pulsar, the evolution can be influenced by the presence of a pulsar wind nebula (PWN). A PWN is driven by the spindown energy from a rapidly rotating pulsar. Part of this energy provides the pressure which pushes against the gas of the SNR interior. This leads to the formation of a (relativistically hot) bubble around the pulsar.

The main subject of this thesis is the interaction between the PWN and the SNR. This chapter consists of a short overview of SNRs and PWNe from an observational point of view, which is followed by a theoretical discussion of the several evolutionary stages of a SNR and a PWN.

1.2 Observations of SNRs and PWNe

Supernova remnants can be observed from radio frequencies up to X-ray frequencies. From the morphology of a specific remnant and the spectral information at radio frequencies, one can classify it in a basic category. In the following section I briefly discuss these categories.

1.2.1 Shell type remnants

Shell type remnants are characterised by extended emission at both X-ray frequencies and radio frequencies. The morphology of these type of remnants is a roughly spherical shell. I will make a distinction between observations at radio frequencies and at X-ray frequencies.

Radio emission

Most of the SNRs are of this category. According to Green's catalogue which contains 225 SNRs (Green 2000), there are about 193 galactic remnants of this type, although the morphology can be very distinct. At radio frequencies the emission is clearly nonthermal, with a spectrum that can be characterized by a single power law, $S_\nu \propto \nu^{-\alpha}$, over several orders of magnitude in frequency. The power law index varies from $\alpha = 0.6$ for young remnants to $\alpha = 0.5$ for the older ones. The nonthermal emission is attributed to synchrotron radiation, due to relativistic electrons gyrating around the magnetic fields in the shells of the SNR. These relativistic electrons are probably produced by the mechanism known as diffusive shock acceleration (DSA) (see chapter 2 for a detailed discussion). The idea of DSA is that particles can cross the shock many times due to scattering in a turbulent magnetic field. Each time a particle cycles across the shock it gains energy, but at each crossing cycle there is a finite chance of escape. In this way particles can be accelerated quite efficiently, where simplified DSA predicts a resulting momentum distribution $N(p) \propto p^{-s}$ (with $s = (r + 2)/(r - 1)$ and r is the shock compression ratio). The power law index α is related to the power law index s by $\alpha = (s - 1)/2$, which yields a power law index $\alpha = 0.5$ for a strong shock with compression ratio $r = 4$. This is near the observed value for the spectral distribution of older remnants, which seems to confirm the idea of DSA taking place at the blastwaves bounding SNRs.

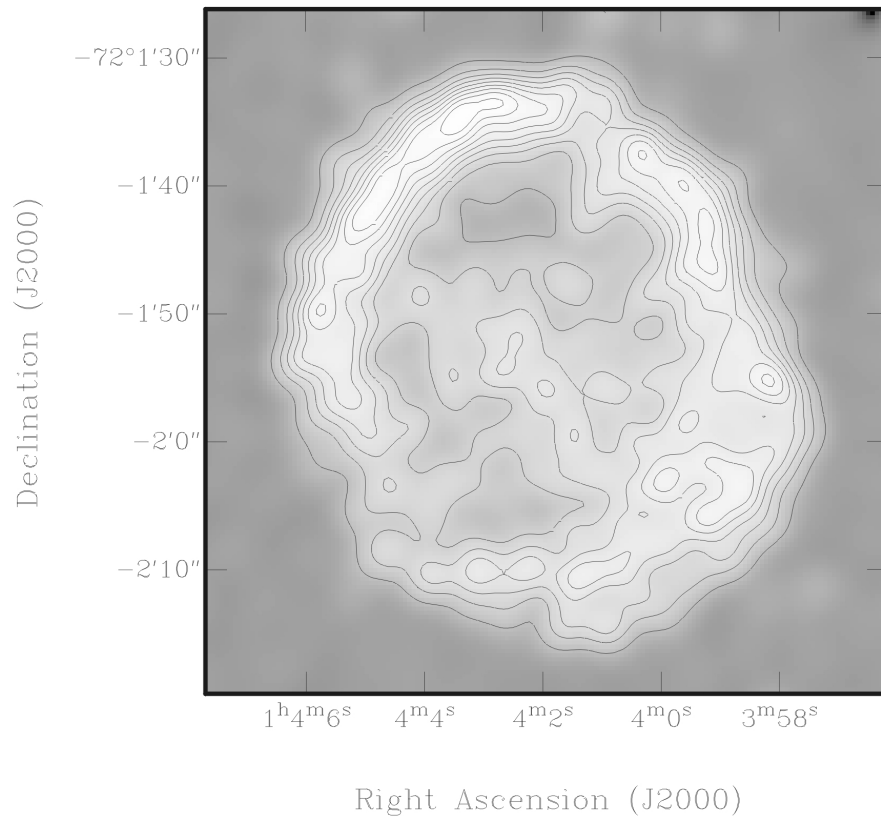


Figure 1.1: *Radio image (at 6 cm) of SNR 0102 in the LMC (Amy & Ball 1993). The observations were performed with the ATCA instrument. The contours were drawn at 0.1,0.2,..0.9 the peak brightness. The greyscaling on the other hand is displayed logarithmically. This is a typical example of a shell type remnant.*

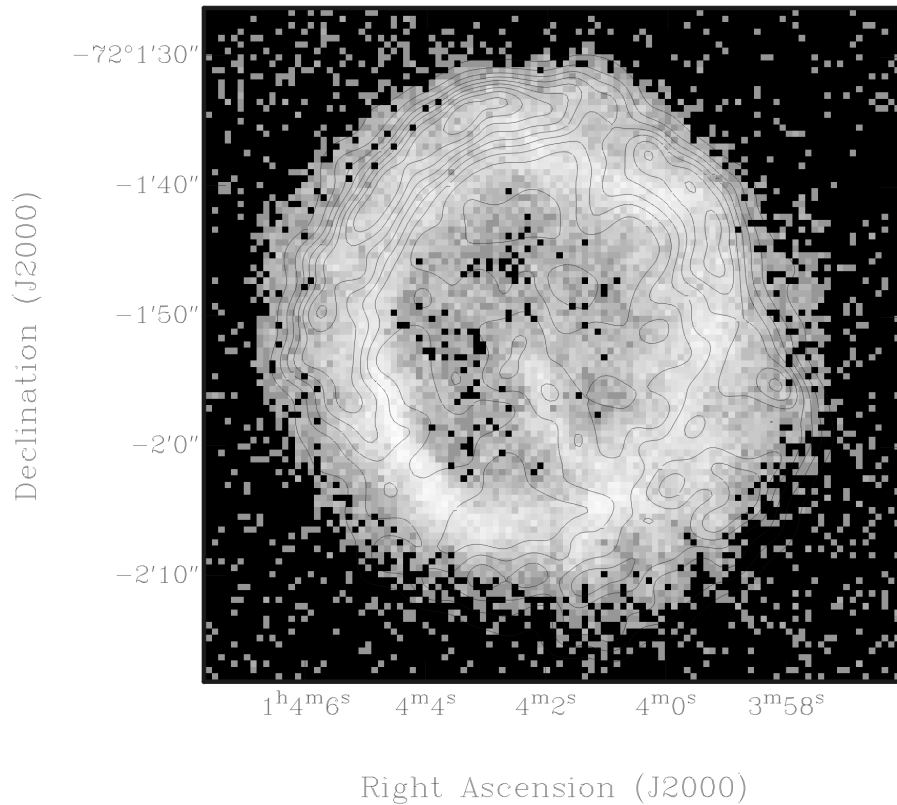


Figure 1.2: Same data as in figure 1. Here the greyscaling corresponds with the X-ray data taken from the Chandra archive. One can see that in this remnant the peaks in the radio and the X-ray frequencies are not at the same positions.

In the free expansion stage the material of the SNR consists mainly of expanding ejecta, bounded by a forward shock. This forward shock is accompanied by a reverse shock, due to the deceleration of the SNR by the ISM. The reverse shock is driven back into the interior of the SNR at a later stage, heating the interior so that the SNR makes the transition to the Sedov-Taylor stage.

Radio observations of SNRs clearly show the presence of the forward shock, which propagates in the ISM. Clear evidence for the presence of a reverse shock, which is driven in the ejected material of the progenitor star, has never been observed in any SNR at these frequencies. This implies that DSA is not efficient at the reverse shock. The reason for this is the much lower value of the magnetic field strength in the ejected material, which slows down the acceleration process significantly. This underlines the importance of a strong magnetic field in the medium in which a shock propagates, in order to make the shock an efficient accelerator. This may also explain the gap between *very young* remnants like SN 1987A with ages of ~ 10 years and *young remnants* like CasA with ages of ~ 100 years: in the first few hundred years, the forward shock of the remnant is propagating in the bubble of material from the progenitor stellar wind. Again the magnetic field strength seems to be too low to let the shock act as an efficient accelerator. However, when the forward shock has caught up with the front of the stellar wind bubble, it starts to propagate through the medium of the ISM. In this medium the magnetic field is sufficiently strong so that electrons can be accelerated efficiently to radio emitting frequencies.

X-ray emission

At X-ray frequencies most of the observed radiation from SNRs has a strong thermal component. The thermal radiation comes from the hot shocked gas inside the remnant at temperatures of $\propto 10^6 - 10^7$ Kelvin, from material located between the forward shock and the reverse shock. The radiation mechanism responsible for thermal emission from this hot material are severe: thermal bremsstrahlung, line emission and free-bound emission. The emitting gas can be both the ejected material from the progenitor star and the swept-up interstellar gas. For young remnants, the X-ray emission is dominated by shocked ejecta. With the XMM-Newton satellite, it is possible to investigate the distribution of the heavy elements of the ejecta in a SNR like Tycho (Decourchelle et al. 2001). In older remnants, the temperatures of the gas decreases, due to the deceleration of the blastwave, which makes these remnants harder to detect at X-ray frequencies.

Some remnants are peculiar, such as W44, which has a centrally peaked X-ray surface brightness. Cox et al (1999) suggest that thermal conduction has transported energy to the center of the remnant. There are several other remnants with a similar morphology in X-rays (W28, 3C400.2, Kes 27, MSH 11-61A, 3C391, and CTB 1)(Rho 1995).

The recent discovery of nonthermal X-ray emission from SNRs have provided evidence for particle acceleration at SNR shocks up to energies of 10-100 TeV. The X-ray emission from SN1006 (Koyama et al. 1995) and G347.3-0.5 (Koyama et al. 1997, Slane et al. 1999) is dominated by this nonthermal component. Cas A, Kepler, Tycho and RCW 86 (Allen, Gotthelf, & Petre 1999) also show a nonthermal component, but in these systems there is also a significant thermal component. Very recently another nonthermal shell-type SNR, G266.2-1.2 (Slane et al. 2001) has been added to the list of SNRs which are dominated by a nonthermal component. This is strong evidence for the scenario that cosmic rays up to the knee (around 10^{15} eV) of the cosmic ray spectrum, indeed originate from shocks bounding SNRs. The cosmic ray spectrum observed at Earth has a power law spectrum in energy, $N(E)dE \propto E^{-s}dE$, with $s = 2.75$, which has been modified by the transport of cosmic rays in our galaxy. The source spectrum of these particles should have an index close to the value of $s = 2.2$ (Drury et al. 1994). This is again remarkably close to the value of $s = 2.0$ expected from DSA.

1.2.2 Plerionic type remnants

A plerion is a filled-center remnant (Weiler & Panagia 1978) at radio and X-ray frequencies. It is thought to contain a pulsar, which converts a significant fraction of its spin-down energy into a pulsar wind. The kinetic energy of this wind, which is believed to be relativistic with a bulk Lorentz factor $\gamma_w \propto 10^4 - 10^6$, is converted into a relativistically hot plasma at a termination shock. This hot plasma is believed to be the source of the observed plerionic emission. At radio frequencies, a plerionic component can be distinguished from a shell-type component by its center-filled morphology and a flat spectrum, ($-0.3 \leq \alpha \leq 0$, $S_\nu \propto \nu^{-\alpha}$). In the galaxy there are 9 naked¹ plerionic systems known, of which the Crab nebula is the best-known example.

A similar system is 3C58, except that in this plerion no pulsar has been detected. Although all plerions are thought to be driven by a pulsar, this does

¹Plerions without an observable shell.

not mean that the pulsar itself is always detected: so far 10 of the 32 known galactic plerions contain a detectable pulsar. In general pulsars are thought to have a proper motion with respect to the site of the supernova explosion. This can be due to the asymmetric supernova explosion of the progenitor star. Measurements of pulsar velocities show a range from 100-1000 km/sec (see e.g. Lyne & Lorimer 1994, Hartman 1997). This has two consequences: (1) the position of the pulsar is not always at the center of the plerion, and (2) the pulsar is not necessarily located at the brightest part of the plerion. It can be displaced with respect to the region where the pulsar wind deposited most of its rotational energy. Due to the large synchrotron lifetime of the electrons at radio frequencies compared with the age of the plerion, this region can still have the largest surface brightness. At X-ray frequencies, the pulsar's position is located at the brightest spot. Here the synchrotron lifetime is shorter than the age of the plerion. This gives an indication of the pulsar's position in the SNR, even when the pulsar itself has not been detected.

1.2.3 Composite remnants

Composite remnants are by far the most interesting category for this thesis. In the Galaxy there are 23 of these systems known. In this type both the plerionic component and the shell component are present. The properties of the plerionic nebula and the outer shell are the same as described above. Probably the best examples for the composite remnants are 0540 in the Small Magellanic Cloud, and MSH15-56 in the Galaxy.

A sub-class of composite remnants are those where the pulsar wind seems to interact with the SNR shell. The prototypes for this kind of system is the remnant CTB80. In this system it seems like the pulsar is about to penetrate the shell of the SNR, although this could be a projection effect. If the latter is indeed the case the pulsar has already broken out of the shell. Another system which has become more controversial recently, is G5.4-1.2. In this remnant the morphology suggests that the pulsar has already broken out of its associated SNR shell. However recent measurements by Gaensler and Frail (2000) yield a proper motion for the pulsar which is too small for the pulsar to have originated from the center of the remnant, if the age of the system is given by the characteristic age of the pulsar. This suggest that *either* the pulsar and the SNR are not associated *or* the characteristic age of the pulsar seriously underestimates the true age of the pulsar. Quite recently observations in both radio and X-rays seem to suggest that IC443 is a similar kind of system (Keohane, private communication).

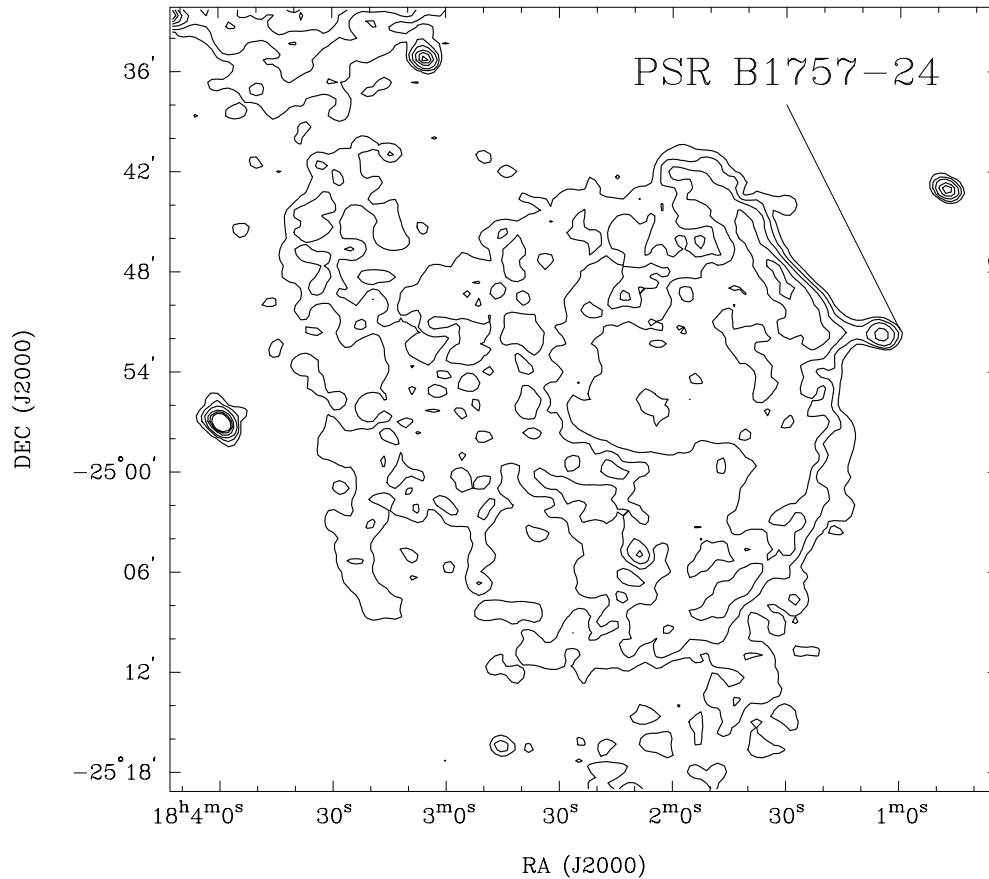


Figure 1.3: Example of a SNR, where the morphology suggests that the pulsar (whose position is marked is at the head of the compact nebula G5.27-0.90) has broken out of the associated SNR shell. The data were taken with the VLA (= Very Large Array), at an observing wavelength of 90 cm; contours are at levels of 10, 25, 50, 100, 150 and 200 mJy beam^{-1} , and the peak intensity is 150 mJy beam^{-1} . The resolution of the image is $60'' \times 45''$ (figure supplied by Bryan Gaensler).

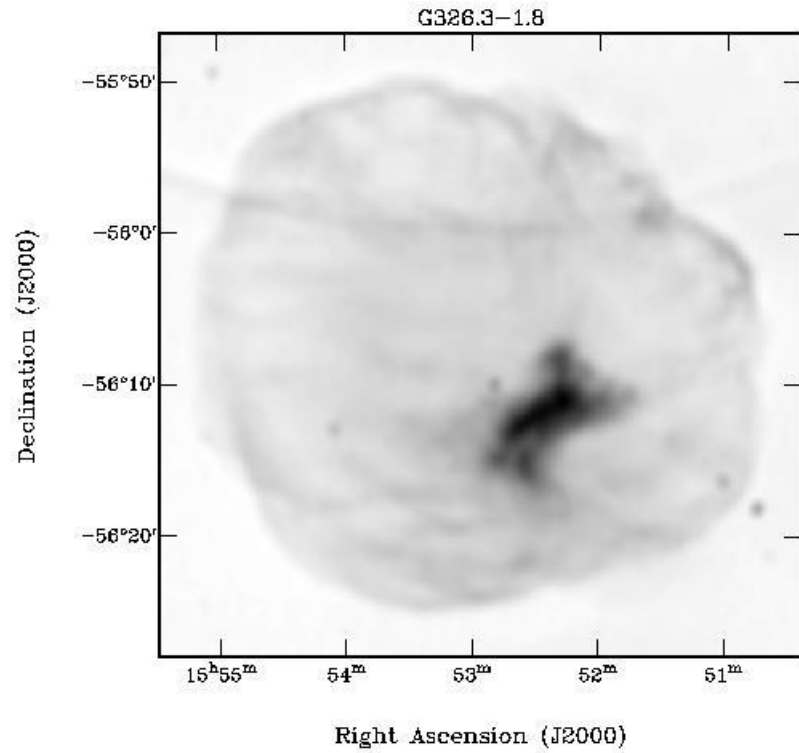


Figure 1.4: *Example of a composite remnant G326.3-1.8(MSH15-56). It was produced from observations made at 0.843 GHz with a resolution of 43'' using the Molonglo Observatory Synthesis Telescope (MOST) (Whiteoak & Green 1996). The bright region corresponds with the plerionic component. The sphere in which the bright (plerionic) component is embedded corresponds with the rest of the SNR.*

The morphology in these kind of systems seems to suggest an interaction between the active pulsar wind and the old SNR shell for these interacting composites: the high-velocity pulsar re-energizes its associated shell (Shull et al. 1989).

In order for this process to occur the pulsar and the SNR shell have to be physically associated and not be due to an apparent projection effect. If the pulsar and the SNR shell are indeed associated, then the next question is whether the pulsar wind is indeed capable of reenergizing the old SNR shell. This question is addressed in the chapters 4 and 6 of this thesis.

Pulsars which catch up with the SNR shell, move supersonically at the time they cross the rim of the SNR. As a result the pulsar wind nebula is deformed, and preceded by a bow shock. Systems like CTB80, G5.4-1.2 and IC443 can be described as these kind of bow shocks.

1.3 The evolution of a supernova remnant

1.3.1 The free expansion stage (duration 100 - 1,000 years)

The supernova explosion generates a shock wave which first will propagate through the outer layers of the progenitor star. The free expansion stage starts when this shock reaches the edge of the atmosphere of the star. In the expanding debris, almost all mechanical energy of the SNR, E_0 , is converted into kinetic energy. Since the mass from the ejecta is still much larger compared then the swept-up mass from the ISM, this results in an almost constant expansion velocity determined by the kinetic energy, E_0 . The expansion proceeds according to

$$R_{\text{snr}} = V_{\text{snr}}t; \quad V_{\text{snr}} \simeq \sqrt{\frac{2E_0}{M_{\text{ej}}}}. \quad (1.1)$$

1.3.2 The Sedov stage (duration 10,000 years)

In the Sedov stage, the swept-up mass of ISM material (mass density ρ_0) exceeds the mass M_{ej} of the ejecta. The interior of the remnant has been heated by the reverse shock, and the remnant is bounded by a strong blast wave.

One can derive the expansion law in the Sedov stage from a simple approximation. The mass of the remnant is

$$M(t) \approx \frac{4\pi}{3} \rho_0 R_{\text{snr}}^3, \quad (1.2)$$

while the typical energy of the remnant is

$$E_{\text{snr}} = \frac{1}{2} M u^2 + \left(\frac{4\pi}{3} R_{\text{snr}}^3 \right) \frac{P}{(\gamma - 1)}. \quad (1.3)$$

The first term in this expression is the kinetic energy of the shell of swept-up material. The typical velocity is the velocity behind the strong blast wave,

$$u \approx \frac{2}{\gamma + 1} \left(\frac{dR_{\text{snr}}}{dt} \right), \quad (1.4)$$

which follows for the shock jump conditions for a strong shock propagating into a cold medium (Landau & Lifshitz 1959). Here γ is the adiabatic heat ratio of the gas, usually taken to be $\gamma = 5/3$.

The second term is the thermal energy of the interior, here approximated as a sphere of radius R_{snr} with constant pressure P . Because of the high sound speed in this interior, there must be approximate pressure equilibrium with the shell of shocked interstellar gas so that

$$P = \frac{2}{\gamma + 1} \rho_0 \left(\frac{dR_{\text{snr}}}{dt} \right)^2. \quad (1.5)$$

Here we use the postshock pressure in the SNR. Substituting relations (1.4) and (1.5) into (1.3), and assuming that radiative losses can be neglected so that

$$E_{\text{snr}} = E_0, \quad (1.6)$$

one finds

$$E_0 = C_\gamma M(t) \left(\frac{dR_{\text{snr}}}{dt} \right)^2, \quad (1.7)$$

where

$$C_\gamma = \frac{4\gamma}{(\gamma - 1)(\gamma + 1)^2}.$$

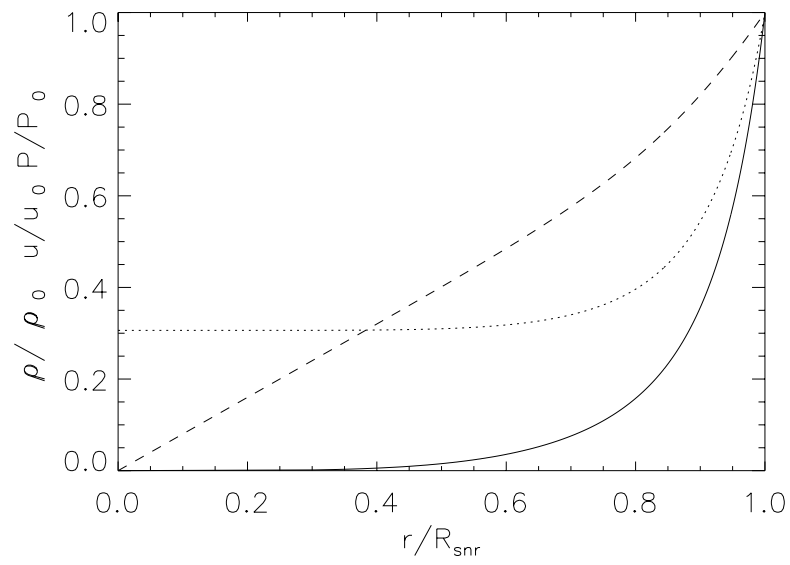


Figure 1.5: *The profiles of the pressure (dotted line), velocity (dashed line) and the density (solid line) in a Sedov SNR. Here the radius has been normalised to the radius of the SNR, R_{SNR} and the physical quantities have been normalised to the postshock quantities.*

In this approximation, the ratio of internal to kinetic energy of the remnant is constant and the total energy is conserved. The internal pressure decreases due to the expansion. By using the equations (1.2) and (1.7), it is possible to derive an equation for the radius of the SNR (see also Zel'dovich and Raiser 1966). This yields:

$$R_{\text{snr}}(t) = \xi_0 \left(\frac{E_0 t^2}{\rho_0} \right)^{1/5} \quad (1.8)$$

$$\bar{\xi}_0 = \left(\frac{75(\gamma - 1)(\gamma + 1)^2}{64\pi\gamma} \right)^{1/5} .$$

This derivation is only an approximation. A full solution solves the equations of fluid flow in spherical symmetry:

$$\frac{\partial \rho}{\partial t} + \frac{1}{r^2} \frac{\partial}{\partial r} (r^2 \rho u) = 0 , \quad (1.9)$$

$$\frac{\partial u}{\partial t} + u \frac{\partial u}{\partial r} + \frac{1}{\rho} \frac{\partial p}{\partial r} = 0 , \quad (1.10)$$

$$\frac{\partial}{\partial t} \left[\rho \left(\epsilon + \frac{1}{2} u^2 \right) \right] + \frac{1}{r^2} \frac{\partial}{\partial r} \left[r^2 \rho u \left(\epsilon + \frac{P}{\rho} + \frac{1}{2} u^2 \right) \right] = 0 . \quad (1.11)$$

As shown by Sedov (1959), this set of equations can be simplified by making the assumption of a *similarity solution*, where fluid quantities depend on the two independent variables, the radius r and time t , in the dimensionless combination (similarity variable)

$$\xi = \left(\frac{\rho_0}{E_0 t^2} \right)^{1/5} r , \quad (1.12)$$

with the outer blast wave at a fixed value $\xi = \xi_0$ so that

$$R_{\text{snr}}(t) = \xi_0 \left(\frac{E_0 t^2}{\rho_0} \right)^{1/5} . \quad (1.13)$$

This is the same relation as derived above in (1.8).

Writing the radial velocity u , density ρ and pressure P as

$$\begin{aligned} u(r, t) &= \frac{r}{t} V(\xi), \\ \rho(r, t) &= \rho_0 \tilde{\rho}(\xi), \\ P(r, t) &= \rho_0 \left(\frac{r}{t}\right)^2 \tilde{P}(\xi), \end{aligned} \quad (1.14)$$

equations (1.9)-(1.11) are converted to a set of ordinary differential equations for the dimensionless variables $V(\xi)$, $\tilde{\rho}(\xi)$ and $\tilde{P}(\xi)$. Now that all quantities are known as a function of radius, it is possible to calculate the correct value of ξ_0 . Integrating the fluid energy density over the volume and equating the total energy to the mechanical explosion energy E_0 one finds $\xi_0 \simeq 1.1516$ for $\gamma = 5/3$ (Sedov 1959). This yields the full solution for the expansion of the SNR in the Sedov stage:

$$R_{\text{snr}}(t) = \xi_0 \left(\frac{E_0 t^2}{\rho_0}\right)^{1/5} \simeq 1.15 \left(\frac{E_0 t^2}{\rho_0}\right)^{1/5}, \quad (1.15)$$

$$V_{\text{snr}}(t) = \frac{dR_{\text{snr}}(t)}{dt} = \frac{2}{5} \frac{R_{\text{snr}}(t)}{t}. \quad (1.16)$$

Figure 1.5 shows the profiles of the pressure, velocity and density of a Sedov solution.

1.3.3 The snowplow stage (duration 10,000-100,000 years)

The Sedov solution is a quite accurate approximation as long as cooling due to radiation losses can be neglected and the total energy is conserved. A transition takes place when radiation losses become important in the shell of the swept-up material. At this point, the swept-up mass collapses into a thin, dense layer, but the interior of the SNR still expands adiabatically. The interior pressure pushes the thin shell through the ISM, like a snowplow would. Due to the work done the internal energy E_T is no longer constant, and is controlled by the following two equations, assuming a sphere of uniform pressure:

$$\frac{dE_T}{dt} = -4\pi R_{\text{snr}}^2 P \left(\frac{dR_{\text{snr}}}{dt} \right) \quad (1.17)$$

$$\frac{4\pi}{3} R_{\text{snr}}^3 P = (\gamma - 1) E_T . \quad (1.18)$$

By combining (1.17) and (1.18) we can express the internal energy from the SNR as a function of the radius R_{snr} . If we take the quantities R_0 and E_{T0} as the values at the moment of the transition from the Sedov to the snowplow stage, and restrict ourselves to the case $\gamma = 5/3$, we find:

$$E_T = E_{T0} \left(\frac{R_0}{R_{\text{snr}}} \right)^2 . \quad (1.19)$$

Because the shell of the SNR is driven outwards by the interior pressure, the equation of motion of the shell is given by:

$$\frac{d}{dt}(MV_{\text{snr}}) = 4\pi R_{\text{snr}}^2 P. \quad (1.20)$$

If we now substitute equation (1.2) into the equation of motion and use (1.19) to express P in terms of E_T we get the following differential equation for the radius of the SNR as a function of time:

$$\frac{d^2}{dt^2} (R_{\text{snr}}^4) = \frac{6E_{T0}R_0^2}{\pi\rho_0 R_{\text{snr}}^3}. \quad (1.21)$$

Inserting a power law, $R_{\text{snr}}(t) \propto t^\alpha$, we find the following solution, using $E_{T0} = \epsilon E_0$:

$$R_{\text{snr}}(t) = \left(\frac{147\epsilon E_0 R_0^2}{4\pi\rho_0} \right)^{1/7} t^{2/7}. \quad (1.22)$$

For times much later than the transition time from the Sedov to the snowplow phase, the exact solution, obtained from integration of equation (1.21), with the appropriate boundary conditions, relaxes to this power-law form. The quantity ϵ is the fraction of the initial mechanical energy remaining in the form of the internal energy of the interior at the moment of transition. We use $\epsilon \simeq 0.2-0.3$ (Blinnikov et al. 1983). The other quantity to be determined is the value of

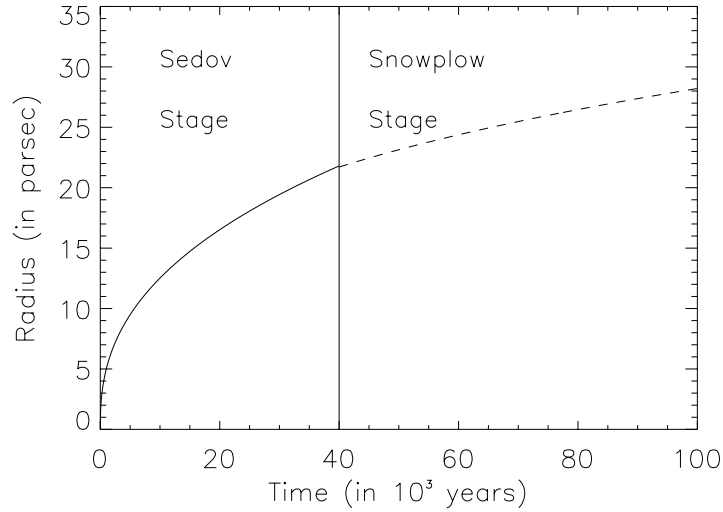


Figure 1.6: Radius of the SNR in the Sedov stage (solid line), and in the snowplow stage (dashed line). Here $E_0 = 10^{51}$ erg, $n_0 = 1$ and $\epsilon = 0.2$. The transition from the Sedov stage to the snowplow stage takes place after $\pm 40,000$ years, and at a radius $R_{\text{SNR}} \simeq 21$ parsec.

R_0 , which marks the radius of the beginning of the snowplow stage. We use the expression from Falle (1981):

$$R_0 = 20 E_{51}^{0.295} n_0^{-0.409} \text{ pc.} \quad (1.23)$$

Here $E_{51} = E_0 / (10^{51} \text{ erg})$ and n_0 is the number density of atoms (in cm^{-3}) in the ISM. In Figure 1.6 we show the radius of the SNR in the Sedov stage and in the snowplow stage for typical parameters.

The next stage will mark the beginning of the end of the SNR where it merges with the ISM. This last stage starts when the pressure in the interior of the SNR becomes comparable with the pressure of the ISM. There will be no force acting on the shell of the SNR, so momentum is conserved, while the shock of the SNR continues to sweep up interstellar gas:

$$M(t)V_{\text{SNR}}(t) = \text{constant} , \quad (1.24)$$

from which one can deduce that

$$\frac{dR_{\text{snr}}}{dt} \propto R_{\text{snr}}^{-3}. \quad (1.25)$$

By assuming a power-law solution, $R_{\text{snr}}(t) \propto t^\alpha$, one gets:

$$R_{\text{snr}}(t) \propto t^{1/4}. \quad (1.26)$$

This last stage is called the momentum-conserving snowplow, after which the SNR merges completely with the ISM, leaving behind a cavity with a higher temperature than the surrounding ISM. The event of merging takes place ~ 750.000 years after the supernova explosion (Cioffi 1990).

1.4 The evolution of a PWN inside a SNR

The expansion of a PWN is driven by the high interior pressure of the nebula. This pressure is the energy of a pulsar wind which has been thermalised in a termination shock. It is commonly assumed that the mechanical luminosity of the pulsar wind equals the observed spindown luminosity of the pulsar: the loss of rotational energy of the neutron star. The PWN pushes ahead a shell of swept-up material (see figure 1.7) The energy input by the pulsar is often modelled using the rotating dipole model, where the luminosity varies with time as

$$L = \frac{L_0}{\left(1 + \frac{t}{\tau}\right)^p} \quad \text{with } p = 2. \quad (1.27)$$

Here $p \equiv (n + 1)/(n - 1)$ with n is the braking index of the pulsar, which is defined in terms of the pulsar's angular velocity Ω , and its derivatives $\dot{\Omega} = d\Omega/dt$ and $\ddot{\Omega} = d^2\Omega/dt^2$ as

$$n \equiv \frac{\Omega \ddot{\Omega}}{\dot{\Omega}^2}.$$

Throughout this thesis we will use a braking index of $n = 3$ which yields $p = 2$. In this way the luminosity decays as t^{-n} for values of $t \gg \tau$. The most important approximation we make in the following discussion of a pulsar wind is by taking a constant luminosity when $t < \tau$ and setting the luminosity equal to zero afterwards. We will derive an expression for the radius of a PWN in the free expansion stage and the Sedov stage, assuming that the pulsar is located at the center of the SNR.

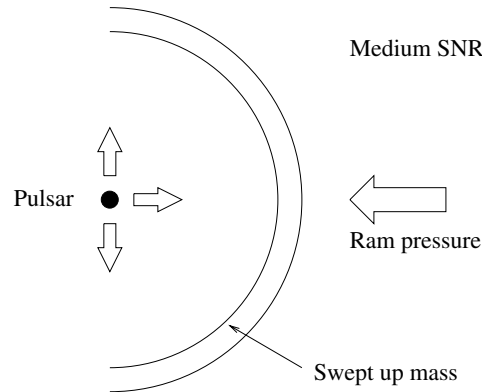


Figure 1.7: The spindown energy of the pulsar pushes ahead a shell which contains the swept up mass from the ambient medium. As long as the kick velocity of the pulsar is small compared with the local sound velocity, ram pressure will not influence the system.

1.4.1 The PWN in a SNR in the free expansion stage

We assume that the initial expansion of the PWN is supersonic, and check this assumption *a posteriori*. In this case, we can generalize equation (1.7), used for the description of the expansion of the SNR. We replace the energy E_0 by the integrated luminosity driving the pulsar wind. Assuming a constant driving luminosity L_0 , the total amount of energy put into the PWN equals $E_{\text{pwn}} = L_0 t$. Substituting this in (1.7), one gets:

$$R_{\text{pwn}}(t) = \tilde{C} \left(\frac{L_0 t^3}{\rho(t)} \right)^{1/5}. \quad (1.28)$$

Where \tilde{C} is a constant of order of unity. The density of the ambient medium is no longer constant, but depends on time due to the expansion of the SNR. As a rough estimate we take:

$$\rho(t) = \left(\frac{3M_{\text{ej}}}{4\pi R_{\text{snr}}^3(t)} \right)^{1/3}. \quad (1.29)$$

Using that $R_{\text{snr}} \propto t$ in the *free expansion stage*, together with (1.28) and (1.29), we get an expression for the radius of the PWN, which scales as:

$$R_{\text{pwn}}(t) = \tilde{C} \left(\frac{L_0 t}{E_0} \right)^{1/5} R_{\text{snr}}(t) \propto t^{6/5}. \quad (1.30)$$

The velocity of the edge of the PWN is given by,

$$V_{\text{pwn}}(t) = \frac{6}{5} \frac{R_{\text{pwn}}(t)}{t}, \quad (1.31)$$

and we can check whether the expansion is indeed supersonic. By calculating the Mach number \mathcal{M} : the ratio between the velocity of the PWN and the local sound velocity c_s .

In order to find c_s we must estimate the pressure inside the SNR. If the expansion is adiabatic we have $P\rho^{-\gamma} = \text{constant}$. Using $\gamma = 5/3$ this implies that the pressure scales as:

$$P(t) = P_0 \left(\frac{R_*}{R_{\text{snr}}(t)} \right)^5. \quad (1.32)$$

If we take R_* to be the radius R_* of the exploding star, and use the fact that, immediately after the explosion, most of the energy is still internal energy so that

$$P_0 \simeq 3(\gamma - 1)E_0/4\pi R_*^3, \quad (1.33)$$

we find:

$$P(t) \simeq \frac{3E_0(\gamma - 1)}{4\pi R_{\text{snr}}^3(t)} \left(\frac{R_*}{R_{\text{snr}}(t)} \right)^2. \quad (1.34)$$

The typical sound speed, $c_s = \sqrt{\gamma P/\rho}$, now follows as:

$$c_s = \left(\frac{\gamma(\gamma - 1)E_0}{M_{\text{ej}}} \right)^{1/2} \left(\frac{R_*}{R_{\text{snr}}(t)} \right) = \left(\frac{\gamma(\gamma - 1)}{2} \right)^{1/2} \frac{R_*}{t}. \quad (1.35)$$

The Mach number associated with the expansion of the PWN is typically

$$\mathcal{M} = \frac{3}{\sqrt{5}} \frac{R_{\text{pwn}}}{R_*} \gg 1, \quad (1.36)$$

where we take $\gamma = 5/3$. This leads us to the conclusion that the expansion of the PWN is indeed supersonic provided $R_{\text{pwn}} \gg R_*$, as is the case.

1.4.2 The PWN in a Sedov-stage remnant

During the free expansion stage a reverse shock is driven back into the interior of the SNR. Once the reverse shock has reached the center of the SNR, the SNR can be approximated by the Sedov stage. This reverse shock reheats the ejecta and as a result the sound velocity increases. Therefore the expansion of the PWN will be subsonic.

Driven pulsar wind nebula

The assumption of a subsonic expansion rate implies that the internal pressure of the PWN, P_i , roughly equals the pressure $P(R, t)$ inside the remnant at radius R_{pwn} :

$$P_i(t) \approx P(R_{\text{pwn}}, t). \quad (1.37)$$

We assume that the interior sound speed inside the PWN is so large such that the pressure can be considered uniform to lowest order. The expansion law then follows from the first law of thermodynamics,

$$dE_T = dQ - P_i dV_{\text{pwn}}.$$

Here E_T is the internal (thermal) energy of the PWN, and V_{pwn} its volume. Approximating the PWN as a homogeneous sphere, and assuming that the pulsar supplies energy at a constant rate L_0 so that $dQ = L_0 dt$, one has:

$$\frac{d}{dt} \left(\frac{4\pi}{3} \frac{P_i R_{\text{pwn}}^3}{(\gamma - 1)} \right) = L_0 - 4\pi R_{\text{pwn}}^2 P_i \left(\frac{dR_{\text{pwn}}}{dt} \right). \quad (1.38)$$

This equation has a simple power-law solution ($R_{\text{pwn}} \propto t^\alpha$) provided the pressure imposed on the PWN (Eqn. 1.37) varies as a power-law in time. The pressure well inside a Sedov remnant behaves in this manner: it is almost uniform for $R < 0.5R_{\text{snr}}$, and varies with time as

$$P(R, t) = \tilde{C} \left(\frac{E_0}{R_{\text{snr}}^3} \right) \propto t^{-6/5}. \quad (1.39)$$

The constant $\tilde{C} \approx 0.074$. As long as $R_{\text{pwn}} \ll R_{\text{snr}}$ relations (1.37)-(1.39) yield an expansion law that can be written as

$$R_{\text{pwn}}(t) = \bar{C} \left(\frac{L_0 t}{E_0} \right)^{1/3} R_{\text{snr}} \propto t^{11/15}. \quad (1.40)$$

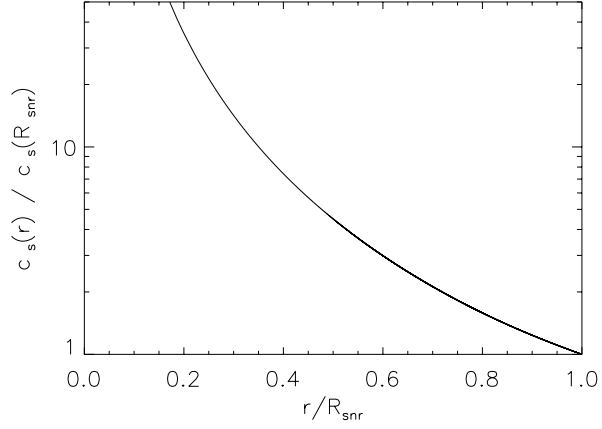


Figure 1.8: *The sound speed in the SNR interior, normalised to the sound speed at the edge of the SNR.*

The constant \bar{C} takes the values $\bar{C} \approx 0.954$ if the PWN material is non-relativistic ($\gamma = 5/3$) and $\bar{C} \approx 0.851$ if the PWN material is relativistically hot ($\gamma = 4/3$). The sound speed inside a Sedov remnant satisfies (see figure 1.8)

$$c_s \geq 0.22 \left(\frac{R_{\text{snr}}}{t} \right), \quad (1.41)$$

where the minimum value is reached at the edge of the remnant. The Mach number $\mathcal{M} = c_s^{-1} (dR_{\text{pwn}}/dt)$ of the expansion follows from (1.40) and (1.41) as

$$\mathcal{M} \leq \mathcal{M}_{\text{max}} = 3.128 \left(\frac{L_0 t}{E_0} \right)^{1/3}. \quad (1.42)$$

For all observed systems (see Table 1.1) one can estimate $\mathcal{M}_{\text{max}} \ll 1$ from the observed pulsar spindown luminosity, the inferred age of the system and the (assumed) mechanical explosion energy $E_0 \approx 10^{51}$ erg. One finds that the assumption of subsonic expansion is a reasonable one.

Table 1.1: *Properties of pulsars with a PWN, this table has been taken from Frail & Scharringhausen(1997).*

| PSR | \dot{E} (ergs s ⁻¹) | PWN | distance (kpc) | Age (kyr) |
|----------|-----------------------------------|--------------|----------------|-----------|
| B0531+21 | 4.5×10^{38} | Crab Nebula | 2.0 | 1.3 |
| B1509-58 | 1.8×10^{37} | G 320.4-1.2 | 4.2 | 1.5 |
| B0540-69 | 1.5×10^{38} | SNR 0540-693 | 55.0 | 1.7 |
| B0833-45 | 6.9×10^{36} | Vela X | 0.5 | 11 |
| B1757-24 | 2.6×10^{36} | G 5.27-0.90 | 4.5 | 15 |
| B1853+01 | 4.3×10^{35} | W 44 | 3.0 | 20 |
| B1951+32 | 3.7×10^{36} | CTB 80 | 2.5 | 107 |

The adiabatic stage

In our simple model, where the mechanical luminosity driving the expansion of the PWN vanishes for $t > \tau$, the expansion slows down after $t = \tau$. Assuming once again subsonic expansion into a Sedov SNR ($R_{\text{snr}} \propto t^{2/5}$), the expansion law in this stage follows from (1.38) with $L_0 = 0$, which implies the adiabatic pressure-radius relation

$$P_i R_{\text{pwn}}^{-3\gamma} = \text{constant} . \quad (1.43)$$

Combining this with the (approximate) condition of pressure equilibrium (Eqn. 1.37) one finds that the radius of the PWN scales as

$$R_{\text{pwn}} \propto R_{\text{snr}}^{1/\gamma} \propto t^{2/5\gamma} . \quad (1.44)$$

The radius of the PWN at $t = \tau$ follows from (1.40),

$$R_{\text{pwn}}(\tau) = \bar{C} \left(\frac{E_*}{E_0} \right)^{1/3} R_{\text{snr}}(\tau) , \quad (1.45)$$

where $E_* \equiv L_0 \tau$ is the total amount of energy injected by the pulsar into the PWN. This gives the expansion law in the adiabatic phase:

$$R_{\text{pwn}}(t) = \bar{C} \left(\frac{E_*}{E_0} \right)^{1/3} R_{\text{snr}}(\tau) \left(\frac{t}{\tau} \right)^{2/5\gamma} . \quad (1.46)$$

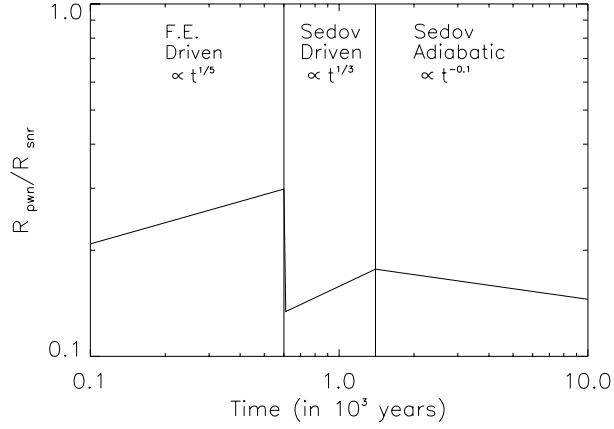


Figure 1.9: The evolution of the ratio $R_{\text{pwn}}/R_{\text{snr}}$ as a function of time throughout the different evolutionary stages. We have taken the timescales such that the reverse shock hits the PWN at a time, $t = 600$ years, and the pulsar wind has a constant luminosity of order $\sim 10^{38}$ ergs/sec when $t \leq 1400$ years.

If the PWN material is non-relativistic ($\gamma = 5/3$) one has $R_{\text{pwn}} \propto t^{6/25}$, if it is relativistically hot ($\gamma = 4/3$) the nebula expands as $R_{\text{pwn}} \propto t^{3/10}$. In both cases the expansion slows down, and the ratio $R_{\text{pwn}}/R_{\text{snr}}$ decreases with time as long as $\gamma > 1$.

1.4.3 More advanced models of a PWN

The Kennel & Coroniti Model

A more detailed model of a PWN was given by Kennel & Coroniti (K&C) (1984): a steady state spherically symmetric, magnetohydrodynamical model of the Crab nebula. One can find a schematic picture of their model in figure 1.10. In their model the highly relativistic pulsar wind constitutes a positronic plasma, which was created in the magnetosphere of the pulsar. This relativistic wind is terminated by a strong MHD shock, decelerating the flow and thermalizing the wind. The magnetization parameter σ , which determines the ratio of the electromagnetic energy flux, $vB^2/4\pi$ to the particle energy flux, $nv\Gamma mc^2$, where n is the particle density and Γmc^2 is the energy per particle, $\Gamma = \sqrt{1 - \beta^2}$ is the Lorentzfactor and $\beta = v/c$ is the dimensionless three speed and B is the

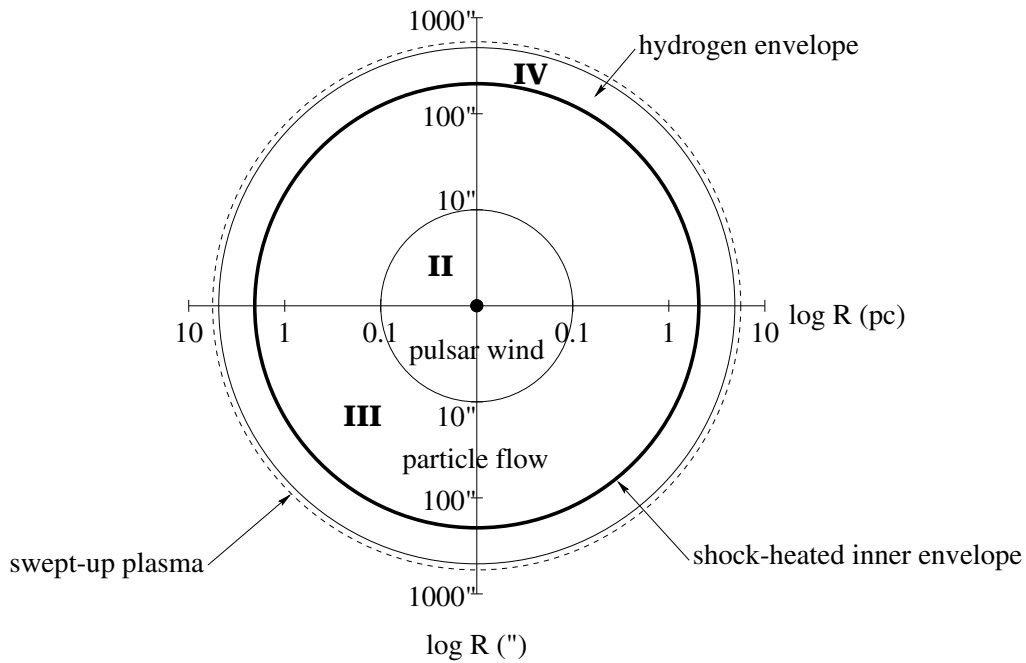


Figure 1.10: Schematic picture of the Kennel & Coroniti model. The dot is the pulsar plus magnetosphere, where the positronic plasma is created. Region II is the region which contains the pulsar wind. At $R = 0.1$ pc the wind is terminated by a strong MHD shock, so the flow is decelerated in region III, which is the synchrotron emitting nebula. Region IV is the SNR in which the PWN is embedded. The SNR itself is bounded by a strong shock, which propagates into the interstellar medium. The scale on the y-axis applies for the Crab Nebula at a distance of $D \simeq 2$ kpc.

magnetic field strength. The associated magnetization parameter σ equals:

$$\sigma = \frac{B^2}{4\pi n\Gamma mc^2}. \quad (1.47)$$

It appears in the Rankine-Hugoniot jump conditions used to determine the upstream and downstream parameters at this MHD shock. This magnetization parameter determines the efficiency of converting the energy contained by the pulsar wind into synchrotron radiation. Beyond this shock lies the shock heated PWN which emits this synchrotron radiation, The PWN itself is embedded in the surrounding SNR. K&C assume pressure balance at the boundary of the PWN. Figure 1.10 gives a schematic picture of the four regions of the K&C model.

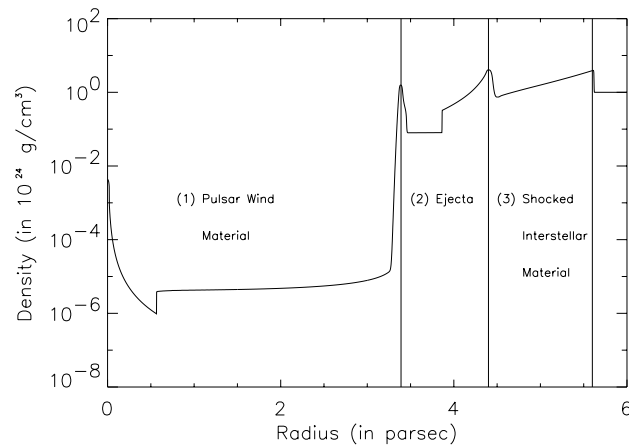


Figure 1.11: *The density profile of a supernova remnant containing a centered pulsar wind. One can identify the pulsar wind termination shock at $r \simeq 0.5$, the PWN shock at $r \simeq 3.4$, the reverse shock at $r \simeq 3.8$ and the forward shock at $r \simeq 5.6$. The expansion of the PWN is in its supersonic stage of its evolution.*

The Begelman & Li Model

The Begelman & Li model (1992) is an extension of the K&C model, both models for the Crab nebula. Instead of a spherical symmetric model (r, θ, ϕ) , the model of Begelman & Li is an axially symmetric model (r, z, θ) , which allows to include the influence of the toroidal magnetic field on the dynamics of the PWN. This introduces a pressure difference across the interior and the exterior of the pulsar wind bubble, which depends on the angle θ . This results in an elongation of the PWN as is observed for the Crab nebula. Furthermore they connect the observed elongation of the Crab nebula to the aforementioned magnetization parameter σ , which is shown to be consistent with the K&C model.

Hydrodynamical simulations of PWNe

In chapter 3 we perform hydrodynamical simulations of a centered PWN inside a SNR. An example of the resulting density profile is shown in the figure 1.11: in these simulations the pulsar wind is centered at $r = 0$. The cold freely expanding wind is thermalised by a strong shock ($r \simeq 0.5$), which decelerates the flow. The PWN itself is bounded by a strong shock propagating through

the freely expanding ejecta of the progenitor star ($r \simeq 3.4$). The SNR is in its transition from the freely expanding stage to the Sedov-Taylor stage. In this stage of its evolution there are two shocks present: the reverse shock propagating into the unshocked ejecta ($r \simeq 3.8$) and the forward shock of the SNR ($r \simeq 5.6$).

1.4.4 Excentric pulsars in SNRs

In the previous Sections, I considered a PWN located centrally in an expanding SNR. Here I consider the case where the pulsar, after its birth event, has a velocity V_{psr} . Observations of the proper motion of pulsars by interferometric means (Harrison et al. 1993, Bailes et al. 1990) show transverse velocities in the range of $V_{\text{psr}} \sim 100 - 500$ km/s, while indirect estimates based on pulsar-SNR associations yield velocities in the range $V_{\text{psr}} \sim 100 - 2000$ km/s (Frail et al. 1994).

The expansion velocity of a SNR in the free expansion stage is of order 10,000 km/s, much larger than the inferred pulsar velocities. This means that the pulsar will only reach the edge of the SNR (if at all) in the Sedov phase or later, in the snow plow phase.

In the Sedov phase, where $R_{\text{snr}} \propto t^{2/5}$ the condition $V_{\text{psr}}t = R_{\text{snr}}$ fixes the ratio of the pulsar velocity and the expansion velocity of the remnant at the moment that the pulsar reaches the outer edge:

$$V_{\text{psr}} \bigg/ \frac{dR_{\text{snr}}}{dt} = \frac{5}{2}. \quad (1.48)$$

Notice that this ratio is *independent* of time and other parameters such as the explosion energy E_0 and density ρ_0 of the interstellar medium. The material at the edge of the SNR moves with the post-shock velocity,

$$u(R_{\text{rms}}) = \frac{2}{\gamma + 1} \frac{dR_{\text{snr}}}{dt} = \frac{3}{4} \frac{dR_{\text{snr}}}{dt}, \quad (1.49)$$

where I assume $\gamma = 5/3$. The relative velocity between pulsar and SNR material then equals

$$V_{\text{rel}} = V_{\text{psr}} - u(R_{\text{rms}}) = \frac{7}{4} \frac{dR_{\text{snr}}}{dt}. \quad (1.50)$$

Since the sound speed at the edge of the remnant is

$$c_s(R_{\text{snr}}) \simeq 0.56 \left(\frac{dR_{\text{snr}}}{dt} \right) ,$$

the pulsar moves supersonically with respect to the SNR material the moment it reaches the edge of the SNR:

$$\mathcal{M}_{\text{psr}} = \frac{V_{\text{rel}}}{c_s} \approx 3.182 . \quad (1.51)$$

Again this quantity is independent of time and other parameters. In the next section we will discuss the physics of bow shocks moving in a medium with a constant density and a negligible pressure.

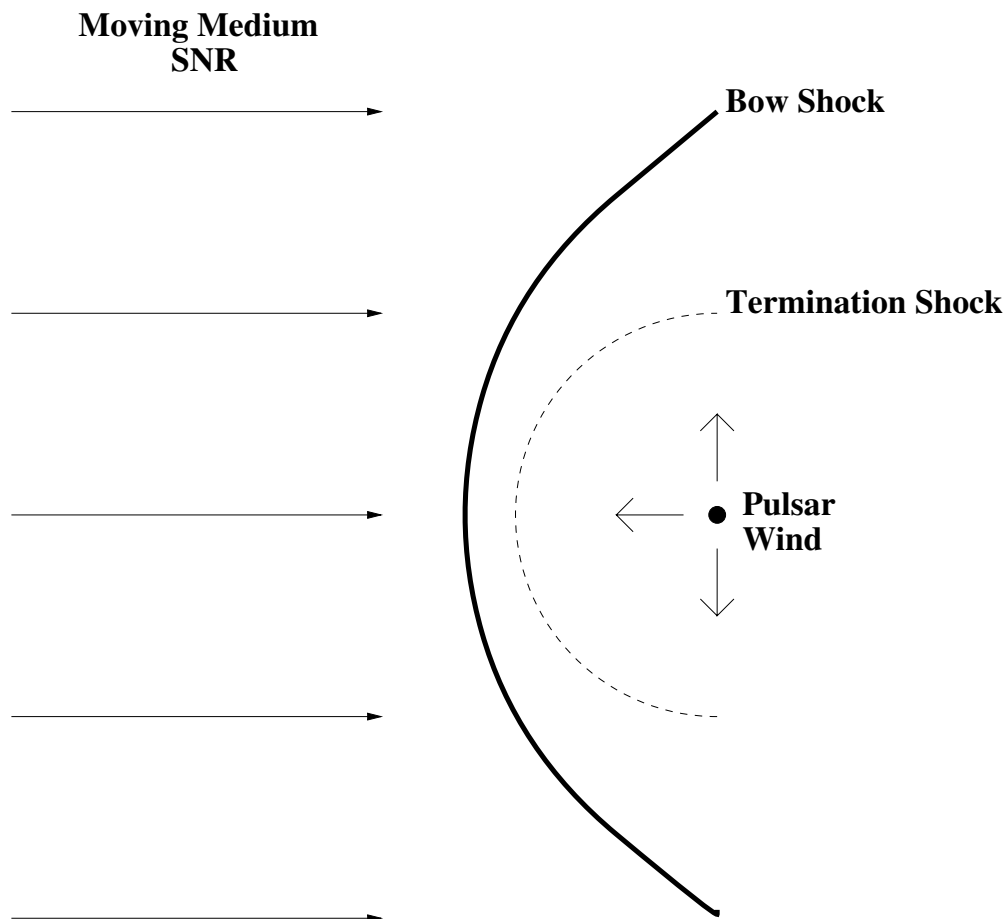


Figure 1.12: Overview of the bow shock structure of a pulsar wind nebula moving through a uniform medium, from the point of view of the pulsar.

1.4.5 Theory of bow shocks

For a pulsar moving with a constant velocity through a medium with a constant density, the morphology is depicted in figure 1.12. The pulsar wind, driven by the spindown energy, is terminated by a wind termination shock. The pulsar wind nebula itself has been deformed to a bow shock due to the supersonic motion of the pulsar. By neglecting the pressure of the ISM, and only include ram pressure, it is possible to derive an equation for the radius of the wind termination shock, r_s . We will first consider a non-relativistic wind, followed by the relativistic limit.

We consider a constant mass injection, \dot{M} , by the pulsar wind. The density, ρ_w , in the pulsar wind region due to mass conservation is given by:

$$\rho_w \simeq \frac{\dot{M}}{4\pi r^2 V_w}. \quad (1.52)$$

Here the velocity of the pulsar wind is denoted as V_w . When the surrounding medium of the pulsar wind region is uniform and constant, we can use ram-pressure equilibrium, $\rho_{\text{ISM}} V_{\text{psr}}^2 = \rho_w V_w^2$, to determine the radius of the wind termination shock:

$$r_s = \left(\frac{\dot{M} V_w}{4\pi \rho_{\text{ISM}} V_{\text{psr}}^2} \right)^{1/2} \quad (1.53)$$

The above equation is a non-relativistic equation. A pulsar wind is relativistic ($\Gamma = 10^{5-6}$), therefore we transform the above equation to an equation which approximates the relativistic solution for the radius r_s . This is done by taking the limit $V_w \rightarrow c$, and multiply the energy and momentum by a factor c to approximate the conversion to the associated relativistic counterparts of energy and momentum. This yields:

$$r_s = \left(\frac{\dot{E}_{\text{psr}}}{4\pi \rho_{\text{ISM}} V_{\text{psr}}^2 c} \right)^{1/2} \quad (1.54)$$

This equation is slightly modified, by solving the problem for a relativistic (wind) flow. In that case the radius of the wind termination shock becomes:

$$r_s = \left(\frac{\dot{E}_{\text{psr}}}{2\pi \rho_{\text{ISM}} V_{\text{psr}}^2 c} \right)^{1/2}. \quad (1.55)$$

A more detailed calculation of bow shocks can be found in recent work done by Wilkin (2000). In chapter 4 of this thesis, we perform hydrodynamical simulations of bow shocks in a medium with a constant density.

Bibliography

- [1] Allen, G.E., Gotthelf, E.V., Petre, R. 1999, "Evidence of 10-100 Tev Electrons in Supernova Remnants" in Proceedings of the 26th International Cosmic Ray Conference, Salt Lake City, 17-25 August 1999, Edited by D. Kieda, M. Salamon, and B. Dingus, Vol.3, 480-483
- [2] Amy, S.W., Ball, L. 1993, ApJ, 411, 761
- [3] Bailes, M., Manchester, R. N., Kesteven, M. J., Norris, R. P., Reynolds, J. E. 1990, MNRAS 247, 322
- [4] Begelman, M.C., Li, Z. 1992, ApJ, 397, 187
- [5] Blinnikov, S.I., Imshennik, V.S., Utrobin, V.P. 1982, Sov.Astron.Lett., 8, 361
- [6] Cioffi, D.F. 1990, Physical Processes in Hot Cosmic Plasmas, Proc. of the NATO Advanced Research Workshop Physical Processes in Hot Cosmic Plasmas, Editors, Wolfgang Brinkmann, Andrew C. Fabian, Franco Giovannelli, Kluwer Academic Publishers, Dordrecht
- [7] Claas, J. 1990, *X-Ray Observations of Supernova Remnants (PhD thesis)*
- [8] Cox, Donald P., Shelton, R. L., Maciejewski, W., Smith, Randall K., Plewa, T., Pawl, A., Rzyzcka, M. 1999, ApJ, 524, 179
- [9] Decourchelle, A., Sauvageot, L.J., Audard, M., Aschenbach, B., Sembay, S., Rothenflug, R., Ballet, J., Stadlbauer, T., West, R.G. 2001, *astro-ph /0012288*
- [10] Drury, L. O'C., Aharonian, F. A., Völk, H. J. 1994, A&A, 287, 959
- [11] Falle, S.A.E.G. 1981, Mon.Not.R.Astron.Soc., 195, 1011

- [12] Frail, D.A., Scharringhausen, B.R. 1997, ApJ, 480, 364
- [13] Frail, D.A., Goss, W.M., Whiteoak, J.B.Z. 1994, ApJ, 437, 781
- [14] Gaensler, B. M., Frail, D. A. 2000, Nature, 406, 158
- [15] Green D.A., 2000, *A catalogue of galactic Supernova Remnants (2000 August version)*, Cambridge: Mullard Radio Astronomy Observatory
(<http://www.mrao.cam.ac.uk/surveys/snrs/>)
- [16] Harrison, P.A., Lyne, A.G., Anderson, B. 1993, MNRAS, 261, 113
- [17] Hartman, J. W. 1997, A&A, 322, 127
- [18] Kennel, C.F., Coroniti, F.V. 1984, ApJ, 283, 694
- [19] Koyama, K., Petre, R., Gotthelf, E.V., Hwang, U., Matsura, M., Ozaki, M., & Holt, S.S., 1995, Nature, 378, 255
- [20] Koyama, K., Kinugasa, K., Matsuzaki, K., Nishiuchi, M., Sugizaki, M., Torii, K., Yamauchi, S., Aschenbach, B. 1997, PASJ, 49, L7
- [21] Landau, L.D., Lifshitz, E.M. 1959, *Fluid Mechanics; Course of theoretical physics*, Oxford, Pergamon Press
- [22] Lyne, A. G., Lorimer, D. R. 1994, Nature, 369, 127
- [23] Rho, J. 1995, Ph.D. thesis, University Maryland
- [24] Sedov, L.I. 1959, *Similarity and Dimensional Methods in Mechanics*, Academic Press, New York
- [25] Shull, J. M., Fesen, R. A., Saken, Jon M. 1989, ApJ, 346, 860
- [26] Slane, P., Hughes, John P., Edgar, Richard J., Plucinsky, Paul P., Miyata, E., Tsunemi, H., Aschenbach, B. 2001, ApJ, 548, 81
- [27] Weiler, K.W., Panagia, N. 1978, A&A, 70, 419
- [28] Whiteoak, J.B.Z., Green, A.J. 1996, A&AS, 118, 329
(on-line version at <http://www.physics.usyd.edu.au/astrop/wg96cat>)
- [29] Wilkin, F.P. 2000, ApJ, 532, 400, 2000

[30] Woltjer, L. 1972, *ARA&A*, 10, 129

[31] Zel'dovich, Ya. B., and Yu. P. Raizer 1966, *Physics of Shock Waves and High Temperature Phenomena*, Academic Press, New York

Chapter 2

Hydrodynamical Modelling and Particle Acceleration

2.1 Introduction

In this thesis I model supernova remnants, pulsar wind nebulae, and their interaction using a hydrodynamics code. In a few cases we combine the hydrodynamics code with an algorithm which simultaneously calculates the propagation and acceleration of energetic particles. This chapter provides a brief theoretical background for both the hydrodynamical simulations and the algorithm used to simulate the behaviour of energetic particles.

2.2 Hydrodynamics

2.2.1 Conservation laws for hydrodynamics

The equations of gas dynamics consist of three conservation laws and an equation of state. A conservation law the following general form:

$$\frac{\partial S}{\partial t} + \nabla \cdot \mathbf{F} = \mathcal{Q}. \quad (2.1)$$

Here the quantity S is the flow variable, \mathbf{F} is the associated flux and \mathcal{Q} is an external source, which can be added for some specific problems.

In gas dynamics, there is a total of three independent flow variables: the mass density ρ , momentum density $\rho\mathbf{V}$ and the total energy density $\rho e + \frac{1}{2}\rho V^2$.

Here e is the internal energy density and \mathbf{V} is the velocity of the fluid. One can express the equations of gas dynamics in a conservative form:

$$\frac{\partial \rho}{\partial t} + \nabla \cdot (\rho \mathbf{V}) = 0; \quad (2.2)$$

$$\frac{\partial(\rho \mathbf{V})}{\partial t} + \nabla \cdot (\rho \mathbf{V} \otimes \mathbf{V} + P \mathbf{I}) = 0; \quad (2.3)$$

$$\frac{\partial}{\partial t} \left(\frac{1}{2} \rho V^2 + \rho e \right) + \nabla \cdot \left(\rho \mathbf{V} \left(\frac{1}{2} V^2 + h \right) \right) = 0, \quad (2.4)$$

here h is the enthalpy,

$$h \equiv e + \frac{P}{\rho}.$$

The equation of state relates the thermal pressure to the other flow variables (density and temperature).

2.2.2 Discretization of the conservation laws

In a hydrodynamics code, the equations of gas dynamics are discretised, which enables one to integrate the equations numerically. We will illustrate the principle of this discretisation by considering a very simple form of a conservation law like (2.1), the advection equation for a scalar $q(\mathbf{x}, t)$ with flux $f(q)$:

$$\frac{\partial q}{\partial t} + \frac{\partial f(q)}{\partial x} = 0. \quad (2.5)$$

The flow variable q is defined on a grid which has a domain $x \in [a, b]$. This domain is discretised by splitting it into N cells, each with a width h , defined as $h = \Delta x = (b - a)/N$. The average value of $q(x, t)$ in a single grid cell i at time t_n is given by:

$$Q_i^n \simeq \frac{1}{h} \int_{x_i}^{x_{i+1}} q(x, t_n) dx, \quad (2.6)$$

where $i = 1 \dots N$.

We want to construct a conservative scheme, which insures that the sum over all the average values Q_i^n will only change due to the fluxes at the boundaries of the grid, i.e. the flux at $x = a$ and $x = b$. Therefore we discretise equation

(2.5) in its integral form over one single cell by integrating it over a single time step $\Delta t = \tau \equiv (t_{n+1} - t_n)$:

$$\int_{x_i}^{x_{i+1}} q(x, t_{n+1}) dx - \int_{x_i}^{x_{i+1}} q(x, t_n) dx = \int_{t_n}^{t_{n+1}} f(q(x_i, t)) dt - \int_{t_n}^{t_{n+1}} f(q(x_{i+1}, t)) dt. \quad (2.7)$$

This equation can be rewritten in a **flux-differencing form**, using equation (2.6):

$$Q_i^{n+1} = Q_i^n - \frac{\tau}{h} (F_{i+1}^n - F_i^n). \quad (2.8)$$

Here F_i^n is an average value for the flux at $x = x_i$:

$$F_i^n \simeq \frac{1}{\tau} \int_{t_n}^{t_{n+1}} f(q(x_i, t)) dt. \quad (2.9)$$

In this way we have converted a conservation law into an equation which can be solved numerically.

In a hydrodynamics code, the complete set of partial differential equations as given by equations (2.2)-(2.4) are discretised in a similar, but more advanced way as illustrated above. This yields the solution of the flow variables over a grid as a function of time. In this way, one can investigate more complex flows numerically. For a more detailed discussion of more advanced numerical techniques, the reader is referred to LeVeque (1998).

2.2.3 The Versatile Advection Code

Throughout this thesis we will use the Versatile Advection Code (VAC), which is a general tool for solving hydrodynamic and magnetohydrodynamic problems which arise in astrophysics. The philosophy behind VAC is to use the software for various problems, rather than developing a different code for each specific problem¹. In order for the software to be used in this way, it consists of different options and switches which can be used for initialising a specific problem. The software package has been developed by Gábor Tóth since 1994 as

¹Specific information: <http://www.phys.uu.nl/~toth/>

part of the project on 'Parallel Computational Magneto-Fluid Dynamics' (Tóth (1994), Tóth & Odstrčil (1996)). VAC solves a set of conservation laws with source term of the form (2.1). In the module used throughout this thesis, these conservation laws where the conservation laws or gas dynamics plus the equation of state. For the simulations we have performed in this thesis, we took the symmetry of the grid as a 1D spherically symmetric one or a 2D axially symmetric one. The algorithms used to integrate the conservation laws of gas dynamics were the *tvd-muscl* scheme and the *tvd-lf* scheme (see LeVeque for a detailed discussion). After the initialisation of the code, VAC gives as a function of time the different flow variables throughout the grid.

2.3 Particle Acceleration

2.3.1 Introduction

A magnetized astrophysical flow can be an efficient accelerator of relativistic particles if there are strong shocks present. Examples of such accelerators are supernova remnants(SNRs), pulsar wind shocks and the jets associated with the Central Engine in active galactic nuclei. In these objects shocks can accelerate particles by the mechanism known as **Diffusive Shock Acceleration** (DSA), a realization of *first order Fermi acceleration* (Fermi 1949).

Due to efficient scattering, caused by irregularities in the magnetic field, particles can cross a shock repeatedly before they are advected downstream. Each time a particle crosses a shock from downstream \rightarrow upstream \rightarrow downstream it will gain energy because of the difference in across the shock. For relativistic particles ($v \sim c$) the gain in momentum p per cycle can be written as:

$$\left\langle \frac{\Delta p}{p} \right\rangle = \frac{4}{3} \frac{U_1 - U_2}{c}. \quad (2.10)$$

Here c is the light speed and U is the velocity of the fluid in the shock rest frame, where the subscripts 1 (2) refer to the upstream (downstream) region. The chance for a particle to escape downstream and not be reflected backwards across the shock again, equals:

$$\mathcal{P}_{\text{esc}} \simeq \frac{4U_2}{c} \ll 1 \quad (2.11)$$

Due to this finite chance of escape, accelerated particles will be distributed in

a power-law in momentum. It can be shown that the slope s of this power-law equals:

$$s \equiv 1 + \frac{\text{escape rate}}{\text{acceleration rate}} \quad (2.12)$$

By using the equations (2.10) and (2.11), the slope s can be expressed as a function of the compression ratio $r = \rho_2/\rho_1 = U_1/U_2$ of the shock, which yields:

$$s = \frac{r + 2}{r - 1}. \quad (2.13)$$

This result can be derived in a more formal way, by solving the particle transport equation near a standing, plane-parallel shock.

2.3.2 The transport equation

In general one has to find a solution for the distribution function of the particles $F = F(\mathbf{x}, \mathbf{p})$ by solving the transport equation. In its simplest form, for an isotropic distribution which depends only on the magnitude of momentum p , this equation reads:

$$\frac{\partial F}{\partial t} + \nabla \cdot \mathbf{S} + \frac{\partial}{\partial p} \left(\left\langle \frac{dp}{dt} \right\rangle F \right) = 0, \quad (2.14)$$

e.g. Skilling (1975a&b). Here the flux \mathbf{S} consists of an advective term, describing how the fluid drags particles along, and a diffusive term, which describes the (slow) diffusion of particles with respect to the fluid:

$$\mathbf{S} = \mathbf{V}F - \mathbf{D}_x \cdot \nabla F. \quad (2.15)$$

Here \mathbf{D}_x denotes a diffusion tensor in configuration space. In a magnetised plasma, this tensor is anisotropic due to the influence of the magnetic field on particle orbits. It reads:

$$\mathbf{D}_x = D_{\parallel} \hat{\mathbf{b}}\hat{\mathbf{b}} + D_{\perp} (\mathbf{I} - \hat{\mathbf{b}}\hat{\mathbf{b}}). \quad (2.16)$$

Here $\hat{\mathbf{b}} = \mathbf{B}/|\mathbf{B}|$ is the unit vector along the magnetic field and \mathbf{I} the unit tensor. The field-aligned and perpendicular diffusion coefficients scale roughly as

$$D_{\parallel} \sim \frac{1}{3}c\ell = \kappa_B \left(\frac{\ell}{r_g} \right), \quad D_{\perp} \sim \frac{D_{\parallel}}{1 + (\ell/r_g)^2}. \quad (2.17)$$

Here ℓ is the scattering mean free path, $r_g \sim E/ZeB$ the gyro radius for relativistic particles ($E \approx pc$) of charge $q = Ze$, and

$$D_B \equiv \frac{1}{3} cr_g = \frac{cE}{3|Z|eB} \quad (2.18)$$

is the so-called Bohm diffusion coefficient. Throughout this thesis we will mostly use Bohm diffusion, with $\ell \approx r_g$ and $D_{\parallel} \approx D_{\perp} \approx \kappa_B$.

The mean momentum gain of particles which are collisionally coupled to the flow is due to the flow compression. It equals:

$$\left\langle \frac{dp}{dt} \right\rangle = -\frac{1}{3} (\nabla \cdot \mathbf{V}) p. \quad (2.19)$$

One can derive the power-law index (2.13) of the momentum distribution by solving the transport equation for the simple case of a plane-parallel normal shock, moving with velocity V_{sh} , and with a compression ratio r . The fluid velocity $\mathbf{V} \equiv V \hat{e}_x$ in the shock rest frame is given by:

$$V = \begin{cases} V_2 = V_s/r & \text{if } x < 0, \\ V_1 = V_s & \text{if } x > 0. \end{cases} \quad (2.20)$$

Here x is the coordinate along the shock normal, with $x = 0$ the (fixed) position of the shock. Because the flow is uniform on both sides of the shock, the transport equation is reduced to:

$$\frac{\partial}{\partial x} \left(VF - D \frac{\partial F}{\partial x} \right) = \frac{V_2 - V_1}{3} \delta(x) \frac{\partial(pF)}{\partial p}, \quad (2.21)$$

with $\delta(x)$ the Dirac delta function, and $D \equiv D_{xx}$. In the upstream ($x > 0$) and downstream ($x < 0$) region, the solution is one of a constant (but different) flux: $S_1(p) = \text{constant}$ and $S_2(p) = \text{constant}$. A relation between S_1 and S_2 can be obtained by integrating equation (2.21) across the shock, from $x = -\epsilon$ to $x = +\epsilon$ with $\epsilon \downarrow 0$. This yields an equation for $F(0, p)$, the distribution at the position of the shock:

$$\left(\frac{V_2 - V_1}{3}\right) \frac{\partial}{\partial p} [p F(0, p)] = S_2(p) - S_1(p), \quad (2.22)$$

Far upstream, there will be no particles with a momentum higher than the injection momentum p_0 . Therefore we can take $S_1(p) = 0$ for $p > p_0$. Downstream, the flux is constant, and the particle distribution must be uniform ($F(x, p)$ independent of x). This yields $S_2(p) = \text{constant} = V_2 F(0, p)$. These two conditions yield an equation for the particle distribution $F(0, p)$ at the shock:

$$\frac{\partial}{\partial p} [p F(0, p)] = -\frac{3V_2}{V_1 - V_2} F(0, p). \quad (2.23)$$

The Rankine-Hugoniot relations give the upstream and downstream velocities as $V_1 = rV_2$, with $r \geq 1$. The solution for (2.23) is a power-law in momentum, with a slope determined by the shock compression:

$$F(p) \propto p^{-(r+2)/(r-1)}. \quad (2.24)$$

This solution assumes that the scattering centers are moving with the flow velocity. For a strong, non-relativistic shock, the compression ratio equals $r = 4$. The corresponding slope of the momentum distribution equals $s = 2$.

2.3.3 Maximum energy

In the process of diffusive shock acceleration, the diffusion coefficient and flow velocity determine the acceleration time. If the diffusion coefficient equals $D_{1(2)}$, and the velocity is $V_{1(2)}$ (with subscripts 1(2) denoting upstream (downstream) values), the acceleration time equals (e.g. Drury 1983):

$$t_{\text{acc}} \equiv \left(\frac{1}{E} \frac{dE}{dt}\right)^{-1} = \frac{3}{V_1 V_2} \left(\frac{D_{n1} V_2 + D_{n2} V_1}{V_1 - V_2}\right). \quad (2.25)$$

The diffusion coefficient D_n is the projection along the shock normal:

$$D_n \equiv \hat{\mathbf{n}} \cdot \mathbf{D}_x \cdot \hat{\mathbf{n}} = D_{\parallel} \cos^2 \theta_{Bn} + D_{\perp} \sin^2 \theta_{Bn}. \quad (2.26)$$

Here $\hat{\mathbf{n}}$ is the shock normal and $\theta_{Bn} = \cos^{-1}(\hat{\mathbf{n}} \cdot \hat{\mathbf{b}})$ is the angle between the shock normal and the magnetic field. One can estimate the acceleration timescale for a shock propagating with velocity V_s , assuming Bohm diffusion (eq 2.18),

$$D_n \approx D_B. \quad (2.27)$$

One finds

$$t_{\text{acc}}(E) = \xi \left(\frac{D_B}{V_s^2} \right) = \frac{\xi}{3} \frac{cE}{|Z|eB V_s^2}. \quad (2.28)$$

Here B is the upstream value of the magnetic field. The parameter ξ takes the value $\xi = 20$ for a parallel shock, where the magnetic field is along the shock normal so that the downstream field equals $B_2 = B$. For a perpendicular shock, where the field is in the plane of the shock and $B_2 = 4B$, one has $\xi = 8$. This corresponds to an acceleration *rate* for electrons or protons ($|Z| = 1$)

$$\left(\frac{dE}{dt} \right) = \frac{3}{\xi} \frac{eB V_s^2}{c}. \quad (2.29)$$

Using the above equation for an accelerator with size R_s and a bulk velocity V_s , the maximum energy for protons and electrons equals:

$$E_{\text{max}} = \frac{3}{\xi} \frac{eB V_s R_s}{c}. \quad (2.30)$$

The maximum particle energy will fall below E_{max} in the case of significant losses. Relativistic electrons (and in extreme cases also protons) radiate part of their energy as synchrotron radiation due to the presence of the magnetic field. Electrons of energy $\Gamma m_e c^2$ radiate at a characteristic frequency, ν_s , where the single-particle emission spectrum peaks:

$$\begin{aligned} \nu_s &= 0.29 \frac{3\Gamma^2 eB}{4\pi m_e c} \\ &\simeq 4.67 B_{\mu G} E_{\text{GeV}}^2 \text{ MHz}. \end{aligned} \quad (2.31)$$

The associated timescale $\tau_{1/2}$, after which half of the energy of the electron has been lost due to synchrotron radiation, equals:

$$\begin{aligned} \tau_{1/2} &= \frac{6\pi m_e c}{\sigma_T B^2 \Gamma}, \\ &\simeq 2 \times 10^9 B_{\mu G}^{-3/2} \nu_{\text{MHz}}^{-1/2} \text{ yr}. \end{aligned} \quad (2.32)$$

Here σ_T is the Thomson cross section, $\sigma_T = 6.6 \times 10^{-25} \text{ cm}^2$. In the second equality we express the loss time in terms of the typical observed frequency of the radiation. We can again derive a maximum energy, by equating the timescale associated with the acceleration process (eq. 2.29) and the synchrotron loss-time (eq.2.32). This yields for electrons ($|Z| = 1$):

$$E_{\text{max}} = \sqrt{\frac{18\pi}{\xi}} \left(\frac{m_e^2 c^2 e}{\sigma_T B} \right)^{1/2} V_s . \quad (2.33)$$

This only depends on the velocity V_s of the accelerator and the magnetic field strength, but not on the size R_s of the accelerator.

2.3.4 Monte-Carlo Method

In this section we discuss the Monte-Carlo method used in our numerical simulations to investigate the propagation and acceleration of relativistic particles in an astrophysical flow. The acceleration and propagation of particles is described by a **Fokker-Planck equation**:

$$\frac{\partial F(\mathbf{Z}, t)}{\partial t} = \frac{\partial}{\partial \mathbf{Z}} \cdot \left(-\dot{\mathbf{Z}} F(\mathbf{Z}, t) + \frac{\partial}{\partial \mathbf{Z}} \cdot [\mathbf{D} F(\mathbf{Z}, t)] \right) . \quad (2.34)$$

This is the general form of the transport equation (2.14). $\mathbf{Z} \equiv (\mathbf{x}, \mathbf{p})$ are the coordinates in $2 - n$ dimensional phase space, and $F(\mathbf{Z}, t)$ is the particle distribution function:

$$F(\mathbf{Z}, t) = \frac{d^{2n} N}{d\mathbf{Z}^n} .$$

The other parameters in this equation are an effective advection velocity $\dot{\mathbf{Z}}$ and the diffusion tensor \mathbf{D} on phase space. These are formally defined as

$$\dot{\mathbf{Z}} = \frac{d\mathbf{Z}}{dt} + \frac{\partial}{\partial \mathbf{Z}} \cdot \mathbf{D}^\dagger , \quad \mathbf{D} \equiv \frac{\langle \Delta \mathbf{Z} \Delta \mathbf{Z} \rangle}{2\Delta t} .$$

Here $d\mathbf{Z}/dt$ is the advection velocity, and \mathbf{D}^\dagger the transpose diffusion tensor with components $(\mathbf{D}^\dagger)_{ij} = (\mathbf{D})_{ji}$. The term involving \mathbf{D}^\dagger corresponds to *dynamical friction*.

Achterberg & Krülls (1992) considered a fast simulation method for particle acceleration in an astrophysical flow. This method treats the propagation and acceleration of particles, inclusive the effects of radiation losses such as

synchro/Compton losses. It allows for a quick calculation of the spatial and momentum distribution of relativistic particles in a given flow. The method is based on the correspondence between the Fokker-Planck equation and a stochastic differential equation (SDE) of the Itô form (Gardiner 1983, Saslaw 1985):

$$d\mathbf{Z} = \dot{\mathbf{Z}}(\mathbf{Z}, t) dt + 2^{1/2} \sqrt{\mathbf{D}} \cdot d\mathbf{W}. \quad (2.35)$$

This equation consists of a statistically sharp advection term $\propto \dot{\mathbf{Z}}$, and a noise term. The latter term defines the stochastic part of the equation, and involves a so-called *N-dimensional Wiener process* $d\mathbf{W}$, where N is the number of degree of freedom in phase space. The quantity $\sqrt{\mathbf{D}}$ is a formal notation for a tensor satisfying

$$\sqrt{\mathbf{D}} \cdot \sqrt{\mathbf{D}} = \mathbf{D}.$$

This tensor can always be calculated from a principal axis-transformation. The Wiener process is chosen at each time step dt from a Gaussian distribution, in such a way that $\langle dW_i \rangle = 0$ and the variance satisfies (in component form) $\langle dW_i dW_j \rangle = \delta_{ij} dt$.

The method simulates the advection-diffusion process described by the original Fokker-Planck equation. By considering many statistically independent realizations of the Wiener process $d\mathbf{W}$, one can construct a distribution $F(\mathbf{Z}, t)$ which converges towards a solution of the original Fokker-Planck equation.

As an example we write out the SDE equations for a one-dimensional flow along the x -axis. In such a problem the distribution function depends on two phase-space coordinates, $\mathbf{Z} \equiv (x, p)$. We assume that there is only spatial diffusion along the x -axis, determined by a diffusion coefficient $D(x)$. The SDE equations in this case read:

$$\begin{aligned} dx &= \left(V(x, t) + \frac{\partial D}{\partial x} \right) dt + \sqrt{2D} dW, \\ dp &= -\frac{p}{3} \left(\frac{\partial V}{\partial x} \right) dt. \end{aligned} \quad (2.36)$$

In the above description, the momentum gain at shocks, as well as expansion losses, are incorporated in the term involving the divergence $\partial V/\partial x$ of the flow.

For electrons one has to include synchrotron losses. In that case the momentum equation becomes:

$$dp = - \left[\frac{p}{3} \left(\frac{\partial V}{\partial x} \right) + \beta_{\text{sy}} \Gamma p \right] dt \quad (2.37)$$

$$\beta_{\text{sy}} = \frac{\sigma_{\text{T}} B^2}{6\pi m_e c}.$$

2.4 Explicit schemes for shock acceleration

A simple explicit 1D numerical scheme for the momentum gain reads

$$\Delta \ln p = -\frac{1}{3} \left(\frac{\partial V}{\partial x} \right) \Delta t. \quad (2.38)$$

Hydrodynamical codes usually smear out shocks over a number of grid cells due to (numerical) viscosity. Krülls and Achterberg (1994) have found that a scheme such as (2.38) can in fact correctly calculate the effects of shock acceleration. In order to do so, the different spatial scales of the problem must satisfy the following inequality

$$\Delta x_{\text{adv}} \ll \Delta x_{\text{sh}} \ll \Delta x_{\text{diff}}. \quad (2.39)$$

Here Δx_{sh} is the width of the shock transition.

This condition follows from two different constraints. First of all, the particle must not be advected out the acceleration zone before being accelerated; it must be able to cross the shock a number of times. This condition leads to the requirement $\Delta x_{\text{adv}} \leq \Delta x_{\text{sh}}$. Secondly, the SDE method must compute true shock acceleration, and not simply the effects of *adiabatic compression*; as is the case microscopically, the ‘mesoscopic’ mean free path $\sim \sqrt{2D \Delta t}$ employed by the simulation must be larger than the width of the shock transition. This leads to the requirement $\Delta x_{\text{sh}} \leq \Delta x_{\text{diff}}$. Thus, once the width of the shock and the flow properties are known, the time step Δt can be derived from the previous condition. It is important to note that, when the diffusion coefficient D depends on momentum (as it is case for Bohm diffusion), the width of the shock has to be chosen such that (2.39) is satisfied for the *lowest* value of the diffusion coefficient.

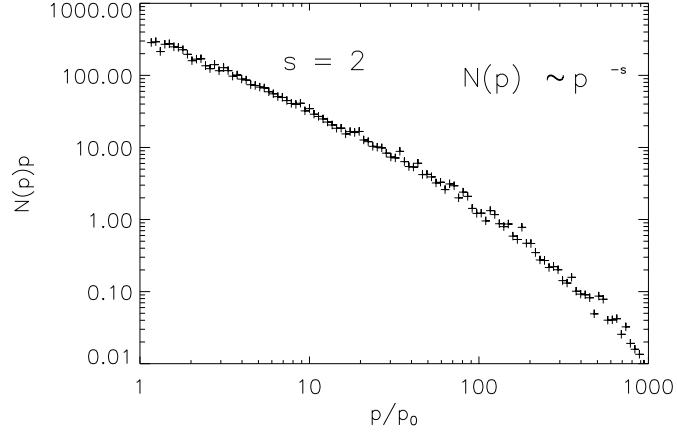


Figure 2.1: F injection at time $t = 0$. Particles are accelerated till time $t = 5$, using a velocity profile (2.20), with $V_{\text{sh}} = 1$.

As an example we again take a stationary, plane-parallel shock, with a velocity profile as in eq (2.20). The resulting momentum distribution is shown in figure 2.1. One can see that the SDE method yields a spectral index which equals $s = 2$, the value expected for a strong hydrodynamical shock. Next we show a simulation which includes synchrotron losses. The particle distribution shows a cut-off near the expected momentum value.

2.5 Implicit schemes for shock acceleration

In some numerical applications, we may not have access to the first derivatives of the fluid velocity. This occurs for example if these quantities are not defined at some points in the grid, or at the particle position. In this case, we can calculate the derivatives *implicitly*, using an interpolation of velocity values between the initial and final particle position:

$$\Delta \ln p = -\frac{1}{3} \left(\frac{V(x + \Delta x, t + \Delta t) - V(x, t)}{\Delta x} \right) \Delta t. \quad (2.40)$$

This scheme is particularly useful when computing acceleration at sharp shock transitions, which occur in analytical calculations of a flow. A direct consequence

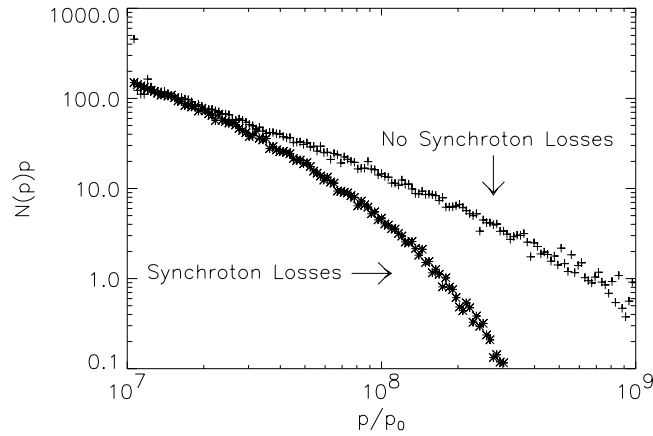


Figure 2.2: *Momentum distribution of instantaneous injection at time $t = 0$. Particles are accelerated till time $t = 5$. There are two curves shown. One is without synchrotron losses, the other one is with synchrotron losses. Using the equation of Webb et al. (1984) the maximum value for $p/p_0 \simeq 1.2 \times 10^8$ which is indeed observed in the above spectrum.*

is that, for implicit schemes, the scale ordering condition (2.39) can be relaxed to

$$(\Delta x_{\text{sh}}, \Delta x_{\text{adv}}) \ll \Delta x_{\text{diff}} , \quad (2.41)$$

as the fluid velocity derivatives can always be defined.

Radiative losses can relatively be easily included in both schemes (details can be found in Krülls & Achterberg 1994 and Marcowith & Kirk 1999).

2.5.1 test problem: acceleration by multiple shocks

As an example we consider the case of particle acceleration by multiple shocks. This situation can arise in accretion disks with spiral shocks (e.g. Spruit 1988) or in astrophysical jets. It has been considered from an analytical point-of-view by Achterberg (1990), Schneider (1993) and Melrose & Pope (1993), and numerically by Marcowith & Kirk (1999) .

In the case of multiple shocks, spread over a large number of diffusive lengths (see below) and without particle escape between shocks, the stationary spectrum hardens to $f(p) \propto p^{-3}$, compared to $f(p) \propto p^{-4}$ for an isolated strong shock. Here $f(p) = dN/4\pi p^2 dp$ is the Vlasov density of the particles. Marcowith & Kirk (1999) have considered the ideal case of a system of identical shocks with equal compression ratio. They derived the stationary particle distribution as a function of inter-shock distance and escape time. Their calculations show that the limiting case, $f(p) \propto p^{-3}$, can be obtained only in a relatively narrow range of inter-shock distances, ranging from 10 to 100 diffusive lengths. The diffusive length is defined as

$$L_{\text{diff}} = D/V_s, \quad (2.42)$$

with V_s the typical speed with which the fluid enters a shock. If the distance between shocks becomes large, radiation losses become important before a particle encounters the next shock.

Energy losses due to radiative cooling will lead to a pile-up of particles near the energy where the gain due to (shock-)acceleration is balanced by the radiative loss, provided the distribution at lower momenta is harder than $f(p) \propto p^{-4}$.

A more realistic case considers a distribution shocks, with different compression ratio, as can be found in galactic super bubbles, in clusters of galaxies, or in radio jets. We consider a 1D-system of shocks, with a randomly chosen compression ratio between 1 and 4, and random inter-shock distances in the range of 10 to 20 diffusive lengths. Figure 2.3 presents results of our simulations. We use as a reference the fiducial case of identical shocks, as considered by Marcowith & Kirk (1999) (Figure 2.3 a). Particles lose their energy through synchrotron losses, with a loss rate such that a pile-up of particles occurs at a momentum corresponding to $p/p_0 = 10^3$, with p_0 the injection momentum.

The Figures 2.3b, c and d show the particle spectrum $f(p)$ at a randomly selected shock, in a number of different cases. The stationary spectrum is harder than the spectrum due to an isolated strong with compression ratio $r = 4$ (Figure 2.3b), clearly showing the effect of particle acceleration by multiple shocks. The spectrum at a given shock in fact depends sensitively on both the shock compression ratio and the compression ratio of neighbouring shocks: it makes a large difference if neighbouring shocks, located within a loss-distance $L \leq L_{\text{loss}}$, are strong (compression ratio $r \sim 4$) or weak (compression ratio $r \sim 1$). Here $L_{\text{loss}} \sim V_s t_{\text{loss}}$ is the characteristic energy loss length at the pile-up momentum.

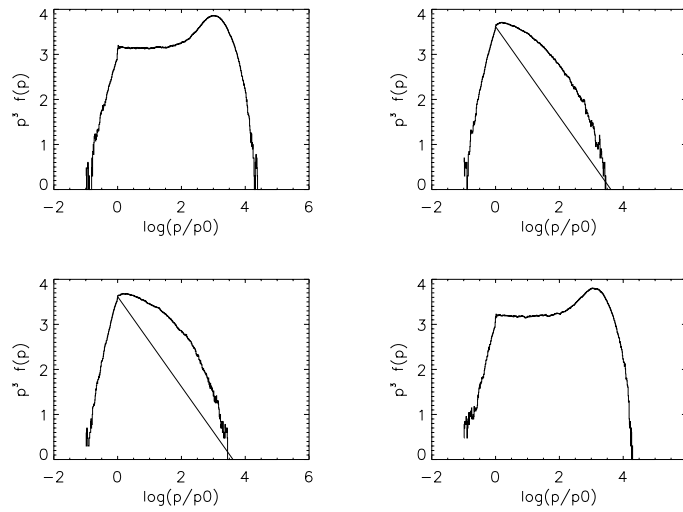


Figure 2.3: Stationary solutions, plotted as $p^3 f(p)$, in a multiple-shock system of 100 shocks. The spectrum is shown at a randomly selected shock with compression ratio of ~ 2 . The figure a (upper left panel) is our fiducial case, with the intershock distances fixed at $L = 20 L_{\text{diff}}$, and with all compression ratios set to $r = 4$. Figure b (upper right panel) plots the spectrum at the same shock but, with a system of random compression ratios between 1 and 4, and the intershock distance randomly chosen as $10 L_{\text{diff}} \leq L \leq 20 L_{\text{diff}}$. Figure c (lower left panel) plots the spectrum at the same shock, with random compression ratios between 1 and 4 but with a fixed intershock distance $L = 20 L_{\text{diff}}$. Figure d (lower right panel) plots the spectrum for a system of strong ($r = 4$) shocks, and a random inter-shock distance $10 L_{\text{diff}} \leq L \leq 20 L_{\text{diff}}$. In figures b and c we also show the power-law momentum distribution for a single (isolated) strong shock of compression ratio $r = 4$.

To separate the effects of the inter-shock distance and the compression ratio on the spectrum, we first consider the same random distribution of compression ratios, with the inter-shock distance fixed at $L = 20 L_{\text{diff}}$. The result is shown in Figure 2.3c. The spectrum is quite similar to the fully random case. In Figure 2.3d shows the effect of the inter-shock distance. The compression ratio of all shocks is fixed at $r = 4$, while the inter-shock distance is chosen randomly in the range $10 L_{\text{diff}} \leq L \leq 20 L_{\text{diff}}$. If the inter-shock distance increases well beyond L_{loss} , the effect of multiple shocks on the spectrum tends to vanish.

2.5.2 Momentum-dependent diffusion

We now consider particle acceleration at a *single* shock, allowing for momentum-dependent diffusion. As an example we take Bohm diffusion, where the particle mean free path for scattering equals the gyro radius of a relativistic particle with charge q in a magnetic field B : $\lambda \approx r_g = pc/qB$. The Bohm diffusion coefficient scales as

$$D_B \equiv \frac{1}{3} cr_g \propto p . \quad (2.43)$$

We assume that the diffusion is isotropic, with diffusion coefficient equal to the Bohm value, $D = D_B$. We neglect the gyrotropic effect of the ambient magnetic field.

Figure 2.4 shows the particle spectrum, plotted as $p^4 f(p)$, due to a shock with compression ratio $r = 4$. This figure shows the spectra for a constant diffusion coefficient, for Bohm diffusion and for the intermediate case of diffusion in magnetic Kolmogorov turbulence (see below). In all three cases, the diffusion coefficient has the same value at the injection momentum p_0 .

The strong momentum-dependence of the diffusion coefficient, $D \propto p$, leads to two main effects: [1] a slight hardening of the spectrum compared to the momentum-independent case (a flat spectrum when plotted as $p^4 f(p)$), and [2] a decrease of the cut-off momentum due to synchrotron losses, the effect of the increase of the acceleration time with momentum,

$$t_{\text{acc}} \sim \frac{D(p)}{V_s^2} \propto p , \quad (2.44)$$

see Drury (1983). The maximum momentum, p_{max} , where synchrotron losses exactly balance shock acceleration, decreases from $p_{\text{max}} \sim 10^4 p_0$ in the case of momentum-independent diffusion to $p_{\text{max}} \sim 10^2 p_0$ in the case of Bohm diffusion (see also Webb et al. (1984), and Drury et al. (1999)).

As an intermediate case, we adopt a softer momentum-dependence of the diffusion coefficient:

$$D \propto p^{1/3} . \quad (2.45)$$

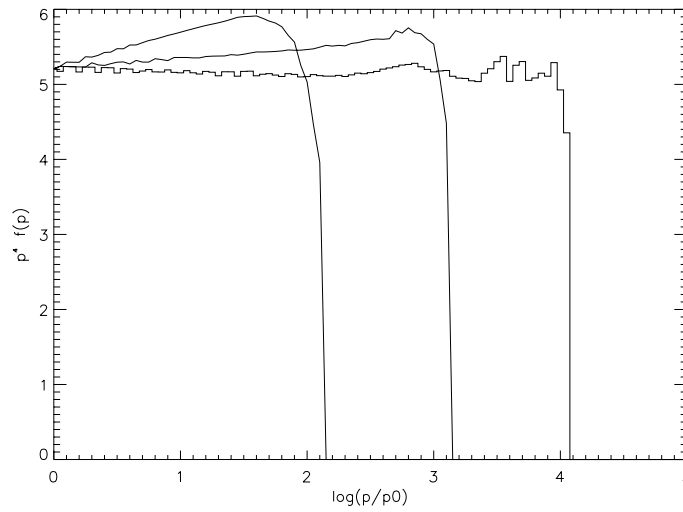


Figure 2.4: *Stationary solutions, plotted as $p^4 f(p)$, for an isolated shock of compression ratio $r = 4$, with different momentum-dependence of the diffusion coefficient (the Bohm case where $D \propto p$, the Kolmogorov case where $D \propto p^{1/3}$, and the case $D = \text{constant}$).*

This momentum dependence is appropriate for gyro-resonant scattering by turbulent MHD waves with a Kolmogorov spectrum, where the energy density per logarithmic bandwidth in the waves scales with wavenumber as $\mathcal{I}(k) d \ln k \propto k^{-2/3} d \ln k$, and where particles are scattered by waves with $k \sim 1/r_g$. In this case, the maximum momentum is $p_{\text{max}} \sim 10^3 p_0$.

2.6 Towards multi-dimensional simulations

2.6.1 Practical limitations

The SDE method can be applied to more complex flows. Here, we consider the coupling of the SDE method to a hydrodynamics code in more detail, and discuss the practical limitations that arise.

The thickness of a shock transition in a hydro-code is determined by the parameters of that code, like numerical or artificial viscosity. The size of the shock is typically a few grid cells. This simple fact results in a lower limit on the diffusion coefficient one can use when combining hydrodynamics with SDE. The condition $\Delta x_{\text{adv}} \ll \Delta x_{\text{sh}}$ of Eqn. (2.39) implies a maximum value for the timestep Δt_{SDE} that can be used in the SDE method, given a fluid velocity \mathbf{V} :

$$\Delta t_{\text{max}} = \Delta x_{\text{sh}} / |\mathbf{V}|. \quad (2.46)$$

Inserting this value for the time step into the second part of the restriction, $\Delta x_{\text{sh}} \ll \Delta x_{\text{diff}}$ yields a *minimum* value for the diffusion coefficient:

$$D_{\text{min}} = \frac{1}{2} |\mathbf{V}| \Delta x_{\text{sh}}. \quad (2.47)$$

If the diffusion coefficient depends on momentum, for instance for Bohm diffusion where $D \propto p$, this condition implies that there is a limit on the range of momenta that can be simulated.

To illustrate this point, consider the acceleration of a particle of charge $q = Ze$ at a parallel shock with shock velocity V_s , where the magnetic field B is along the shock normal. We assume Bohm diffusion with diffusion coefficient

$$D(p) = \frac{pc^2}{3|Z|eB}. \quad (2.48)$$

The momentum change in a single time step for particles in the shock transition is

$$\frac{\Delta p}{p} \approx \frac{1}{3} \left| \frac{dV}{dx} \right|_s \Delta t \approx \frac{V_s \Delta t}{4 \Delta x_{\text{sh}}}. \quad (2.49)$$

Here we assume a strong shock with velocity difference $\Delta V = \frac{3}{4} V_s$ across the shock. For Bohm diffusion, the associated change in the diffusion coefficient satisfies $\Delta D/D \approx \Delta p/p$. If we choose the maximum value allowed for the time step, $\Delta t_{\text{max}} = \Delta x_{\text{sh}}/V_s$, one has

$$\Delta D = \frac{1}{4} D. \quad (2.50)$$

Even if particles are injected with a momentum such that $D(p) \leq D_{\min}$, they will be quickly accelerated into the allowed momentum range.

Problems can occur in multiple shock systems. If particles loose too much energy between shocks, they can enter a momentum range where $D(p) \ll D_{\min}$. In that case, they will 'see' the next shock as a smooth velocity transition, and only gain energy by *adiabatic* compression rather than shock acceleration.

The fact that the hydrodynamics sets a lower limit on the range of momenta that can be simulated may be inconvenient in certain applications. One can in principle circumvent this problem by using adaptive mesh refinement (see for example LeVeque (1998)). This method increases the grid-resolution in those regions where more resolution is needed, for instance around shocks. This method is more appropriate than increasing the resolution over the whole grid.

Another possibility would be to artificially sharpen shocks or to use an implicit SDE scheme (equation 2.41). The first approach can be useful in one dimension, but fail in 2D or 3D when the geometry of shock fronts becomes very complicated, for instance due to corrugational instabilities.

2.6.2 Energy losses and the diffusion restriction

By coupling the SDE method to a flow generated using a hydrodynamics code, one can study the behaviour of energetic particles in this flow in the test-particle limit, i.e. in the case where the particles do not influence the flow. By adding the effect of radiation losses one can generate synthetic maps showing the radiation intensity across the source.

As an example, consider relativistic electrons which radiate through the synchrotron mechanism in a magnetic field B . The synchrotron emission from a single electron with Lorentz-factor Γ peaks at a frequency (Rybicki & Lightman, 1979)

$$\nu_s = 0.29 \frac{3\Gamma^2 e B}{4\pi m_e c}. \quad (2.51)$$

The Bohm diffusion coefficient scales as $D_B \propto \Gamma$, so a lower limit on the diffusion coefficient set by the hydrodynamics translates to a lower limit Γ_{\min} on the Lorentz factor and the associated synchrotron frequency $\nu_s \propto \Gamma_{\min}^2$.

This restriction can be formulated in terms of the timescales of the problem. The synchrotron loss time, in which an electron loses half of its energy, is

$$\tau_{1/2}(\Gamma) = \frac{6\pi m_e c}{\sigma_T B^2 \Gamma}. \quad (2.52)$$

If the flow we are simulating has a linear size L and typical velocity V , one can define a typical advection time

$$\tau_{\text{adv}} \sim L/V. \quad (2.53)$$

The algorithm (2.19) implies that this is also the typical acceleration time if the flow is smooth. When shocks occur, with a width Δx_{sh} , the typical time scale for the energy gain at the shock is

$$\tau_{\text{acc}} \sim \Delta x_{\text{sh}}/V. \quad (2.54)$$

A simulation of the particles in the source should fill a number of requirements:

- It should cover a sufficiently large range of momenta;
- It should clearly show the behaviour of the particle spectrum near the cut-off due to radiation losses;
- It should correctly reproduce the particle acceleration near shocks, as discussed in Section 3.

These requirements lead to a natural order of the different time-scales in the simulation:

$$\tau_{\text{acc}} \ll \tau_{\text{adv}} \leq \tau_{1/2}(\Gamma) \quad (2.55)$$

The constraint on the diffusion coefficient (Eqn. 2.47) turns out to be the most stringent in astrophysical applications. Using once again synchrotron electrons as an example, one can re-express the Bohm diffusion coefficient in terms of the field strength and observing frequency:

$$D_B \approx 10^{22} \nu_{\text{MHz}}^{1/2} B_{\mu\text{G}}^{-3/2} \text{ cm}^2 \text{ s}^{-1}. \quad (2.56)$$

Here we have normalized the physical parameters in this expression to typical values.

The minimum diffusion coefficient is of order

$$D_{\min} \approx 10^{24} \left(\frac{V}{1000 \text{ km/s}} \right) \left(\frac{\Delta x_{\text{sh}}}{0.01 \text{ pc}} \right) \text{ cm}^2 \text{ s}^{-1}, \quad (2.57)$$

with Δx_{sh} the *simulated* shock thickness. We again normalize to typical values. One sees that the simulated diffusion only represents the true state of affairs in the source if the physical diffusion proceeds at a rate much more rapid than the Bohm rate, or if the grid size is sufficiently small. In practical applications, one may choose to simulate the source with a numerical diffusion coefficient which is significantly larger than the physical one. As long as the other conditions are satisfied, at least the energy spectrum of the accelerated particles will correspond to the actual spectrum. The spatial distribution will be too diffuse, rather like looking at the source with a telescope of limited resolution.

Bibliography

- [1] Achterberg, A., & Krülls, W.M., 1992, A&A, 265, L13
- [2] Drury, L.O.C., 1983 Rep.Prog.Phys.,46,973
- [3] Drury, L.O'C., Duffy, P., Eichler, D., Mastichiadis, A. 1999, A&A, 347,370
- [4] Fermi, E. 1949, Phys. Rev., 75, 1169
- [5] Gardiner, C.W. 1983, *Handbook of Stochastic Methods*, Springer Verlag, Berlin, Ch. 4
- [6] Krülls, W.M.,Achterberg, A., 1994, A&A, 286, 314
- [7] LeVeque, R.J. 1998, in: *Computational Methods for Astrophysical Fluid Flow* , Saas Fee Adv. Course 27, R.J. LeVeque, D. Mihalas, E.A. Dorfi & E. Müller (Eds.), p.1, Springer Verlag, Heidelberg
- [8] Marcowith, A., Kirk, J. G., 1999, A&A, 347, 391
- [9] Melrose, D.B., Pope, M.H., 1993, Proc. ASA 10, 222
- [10] Rybicki, G.B., Lightman, A.P., 1979, *Radiative Processes in Astrophysics*, John Wiley & Sons, New York, Ch. 6
- [11] Saslaw, W.C. 1985, *Gravitational physics of stellar and galactic systems*, Cambridge Univ. Press, p. 18
- [12] Schneider, P., 1993, A&A 278, 315
- [13] Skilling, J. 1975, MNRAS, 172, 557
- [14] Skilling, J. 1975, MNRAS, 172, 567

- [15] Spruit, H.C., 1988, A&A 194, 319
- [16] Tóth, G. 1996, Astrophys. Lett. & Comm., 34, 245
- [17] Tóth, G. & Odstrčil 1996, J. Comp. Phys., 128, 82
- [18] Webb, G.M., Drury, L.O'C., Bierman, P. 1984, A&A, 137, 185

Chapter 3

Pulsar Wind Nebulae in Supernova Remnants

E. van der Swaluw, A. Achterberg, Y. A. Gallant and G. Tóth

abstract

A spherically symmetric model is presented for the interaction of a pulsar wind with the associated supernova remnant. This results in a pulsar wind nebula whose evolution is coupled to the evolution of the surrounding supernova remnant. This evolution can be divided in three stages. The first stage is characterised by a supersonic expansion of the pulsar wind nebula into the freely expanding ejecta of the progenitor star. In the next stage the pulsar wind nebula is not steady; the pulsar wind nebula oscillates between contraction and expansion due to interaction with the reverse shock of the supernova remnant: reverberations which propagate forward and backward in the remnant. After the reverberations of the reverse shock have almost completely vanished and the supernova remnant has relaxed to a Sedov solution, the expansion of the pulsar wind nebula proceeds subsonically. In this paper we present results from hydrodynamical simulations of a pulsar wind nebula through all these stages in its evolution. The simulations were carried out with the Versatile Advection Code.

3.1 Introduction

The explosion of a massive star at the end of its life as a supernova releases an amount of energy roughly equal to 10^{53} erg. About 99% of this energy is radiated away in the form of neutrinos as a result of the deleptonization of the $\sim 1 M_{\odot}$ stellar core as it collapses into a neutron star. The remaining (mechanical) energy of about 10^{51} erg is contained in the strong shock propagating through the stellar mantle, and ultimately drives the expansion of the supernova remnant (SNR).

In those cases where a rapidly rotating neutron star (pulsar) remains as a ‘fossil’ of the exploded star, a pulsar wind, driven by the spindown luminosity of the pulsar, can be formed. The precise magnetospheric physics leading to such a pulsar wind is not fully understood, but it is believed that a major fraction of the spin-down luminosity of the pulsar is converted into the mechanical luminosity of such a wind.

The total rotational energy released by a Crab-like pulsar over its lifetime is of order $10^{49} - 10^{50}$ erg. This is much less than the mechanical energy of $\sim 10^{51}$ erg driving the expansion of the SNR. Therefore, the *dynamical* influence of the pulsar wind on the global evolution of the supernova remnant itself will be small. From an observational point of view, however, the presence of a pulsar wind can lead to a plerionic supernova remnant, where the emission at radio wavelengths shows an extended, flat-spectrum central source associated with a Pulsar Wind Nebula (PWN). The best-known example of such a system is the Crab Nebula, and about a half-dozen other PWNs are known unambiguously around pulsars from radio surveys (e.g. Frail & Scharinghausen 1997). These surveys suggest that only young pulsars with a high spindown luminosity produce observable PWNs at radio wavelengths. At other than radio wavelengths, in particular X-rays, there are about ten detections of PWN around pulsars both in our own galaxy and in the large Magellanic cloud (LMC) (e.g. Helfand 1998; Table 1 of Chevalier 2000).

The expansion of an isolated SNR into the general interstellar medium (ISM) can be divided in four different stages (Woltjer 1972; see also Cioffi 1990 for a review): the free expansion stage, the Sedov-Taylor stage, the pressure-driven snowplow stage and the momentum-conserving stage. In the models presented here we will only focus on the evolution of a pulsar wind nebula (PWN) during the first two stages of the SNR: the free expansion stage and the Sedov-Taylor stage. We will assume that the pulsar is stationary at the center of the remnant, excluding such cases as CTB80 (e.g. Strom, 1987; Hester & Kulkarni, 1988), PSR1643-43 and PSR1706-44 (Frail et al., 1994), where the pulsar position

is significantly excentric with respect to the SNR, presumably due to a large kick velocity of the pulsar incurred at its birth, assuming of course that SNR and pulsar are associated and we are not dealing with a chance alignment of unrelated sources. The case of a pulsar moving through the remnant with a significant velocity will be treated in chapter 4 and 6 of this thesis.

In this chapter we compare (approximate) analytical expressions for the expansion of a PWN in a supernova remnant with hydrodynamical simulations carried out with the Versatile Advection Code ¹ (VAC). We confirm earlier analytical results (Reynolds & Chevalier, 1984; Chevalier & Fransson, 1992) which state that the PWN is expanding supersonically when it is moving through the freely expanding ejecta of the SNR. Due to deceleration of the expanding SNR ejecta by the interstellar medium (ISM), a reverse shock propagates back to the center of the SNR (e.g. McKee, 1974 Cioffi et al. 1988)). Due to the presence of reverberations of the reverse shock in the SNR, the expansion of the PWN goes through an unsteady phase when this reverse shock hits the edge of the PNW. After these reverberations have decayed, the expansion of the PWN through the ejecta of the SNR progenitor star continues subsonically with the PWN almost in pressure equilibrium with the interior of the SNR.

This chapter is organised as follows. In sections 3.2 and 3.3 we discuss the aforementioned two stages of the PWN/SNR system. In section 3.4 the hydrodynamical simulations will be presented and compared with the analytical expressions from section 3.2 and 3.3.

3.2 Pulsar Wind Nebula in a freely expanding Supernova Remnant

In the early stage of the evolution of a PWN, the SNR consists mostly of the stellar ejecta expanding freely into the interstellar medium. The PWN expands into these ejecta. The sound velocity in the interior of the SNR is much smaller than the expansion velocity of the PWN. The supersonic expansion of the PWN results in a shock propagating into the ejecta (see figure 3.1).

An analytical equation for the radius of this shock can be derived for a constant spindown luminosity. Using this solution, the assumption of supersonic expansion will be checked *a posteriori*.

¹See <http://www.phys.uu.nl/~toth/>

For simplicity we assume that the ejecta have a uniform density,

$$\rho_{\text{ej}}(t) = \frac{3M_{\text{ej}}}{4\pi R_{\text{ej}}^3}, \quad (3.1)$$

and a linear velocity profile as a function of radius,

$$V_{\text{ej}}(r) = \frac{r}{t} = V_0 \left(\frac{r}{R_{\text{ej}}} \right), \quad (3.2)$$

with $R_{\text{ej}} = V_0 t$ the radius of the front of the ejecta. The value of V_0 is determined by the requirement that the kinetic energy of the ejecta equal the total mechanical energy E_0 of the SNR:

$$E_0 = \frac{1}{2} \rho_{\text{ej}}(t) \int_0^{V_0 t} \left(\frac{r}{t} \right)^2 4\pi r^2 dr = \frac{3}{10} M_{\text{ej}} V_0^2. \quad (3.3)$$

This yields:

$$V_0 = \sqrt{\frac{10}{3} \frac{E_0}{M_{\text{ej}}}}. \quad (3.4)$$

We assume that the stellar ejecta swept up by the strong shock which bounds the PWN collect in a thin shell, and that this material moves with the post-shock velocity. Neglecting the contribution of the thermal energy we can write the total (kinetic) energy of this shell, E_{shell} , as:

$$E_{\text{shell}}(t) = \frac{1}{2} M_{\text{sw}}(t) \left(\frac{3}{4} \dot{R}_{\text{pwn}}(t) + \frac{1}{4} \frac{R_{\text{pwn}}}{t} \right)^2, \quad (3.5)$$

where

$$M_{\text{sw}}(t) \equiv M_{\text{ej}} \left(\frac{R_{\text{pwn}}}{V_0 t} \right)^3 \quad (3.6)$$

is the ejecta mass swept up by the pulsar wind nebula. In deriving the post-shock velocity, we assumed that the ejecta behave as an ideal non-relativistic gas with adiabatic heat ratio $\gamma_{\text{ej}} = 5/3$ and used the Rankine-Hugoniot jump conditions for a strong shock.

The interior of the PWN is dominated by thermal energy. The sound speed in a realistic PWN is close to the speed of light c , while the expansion velocity is much less than c . Perturbations in the pressure will be smoothed out rapidly, on a sound crossing time $t_s \sim R_{\text{pwn}}/c$, much less than the expansion time scale $t_{\text{exp}} \sim R_{\text{pwn}}/\dot{R}_{\text{pwn}}$. Therefore, we can assume a nearly uniform pressure P_{pwn} in the PWN. The internal energy of the PWN then equals

$$E_{\text{pwn}} = \frac{4\pi}{3(\gamma_{\text{pwn}} - 1)} R_{\text{pwn}}^3 P_{\text{pwn}}. \quad (3.7)$$

Here we take $\gamma_{\text{pwn}} = 4/3$ because the pulsar wind nebula material is relativistically hot. The pressure of the interior of the PWN must roughly equal the pressure in the shocked ejecta just downstream of the outer shock of the pulsar wind nebula at R_{pwn} :

$$P_{\text{pwn}}(t) = \frac{2}{\gamma_{\text{ej}} + 1} \rho_{\text{ej}}(t) \left(\dot{R}_{\text{pwn}}(t) - \frac{R_{\text{pwn}}}{t} \right)^2. \quad (3.8)$$

Combining these relations yields:

$$E_{\text{pwn}} = \frac{2M_{\text{sw}}}{(\gamma_{\text{pwn}} - 1)(\gamma_{\text{ej}} + 1)} \left(\dot{R}_{\text{pwn}}(t) - \frac{R_{\text{pwn}}}{t} \right)^2. \quad (3.9)$$

Energy conservation for the PWN system reads:

$$E_{\text{shell}}(t) + E_{\text{pwn}}(t) = E_{\text{init}}(t) + L_0 t. \quad (3.10)$$

Here $E_{\text{init}}(t)$ is the kinetic energy which the swept-up ejecta would have if they were freely expanding. This quantity can be obtained by integrating the kinetic energy density of ejecta in a sphere with radius $r < R_{\text{pwn}}$ if there was no PWN. This yields:

$$E_{\text{init}}(t) = E_0 \left(\frac{R_{\text{pwn}}}{R_{\text{ej}}} \right)^5. \quad (3.11)$$

After some algebra using the equations (3.1)-(3.11) one can obtain a power-law solution for the radius of the pulsar wind bubble:

$$R_{\text{pwn}}(t) = C \left(\frac{L_0 t}{E_0} \right)^{1/5} V_0 t \propto t^{6/5}, \quad (3.12)$$

where C is a numerical constant of order unity:

$$C = \left(\frac{4}{15(\gamma_{\text{ej}} + 1)(\gamma_{\text{pwn}} - 1)} + \frac{289}{240} \right)^{-1/5} \simeq 0.922 \quad (3.13)$$

with $\gamma_{\text{ej}} = \frac{5}{3}$, $\gamma_{\text{pwn}} = \frac{4}{3}$

Reynolds and Chevalier(1984) already obtained this $R(t) \propto t^{6/5}$ expansion law. It can easily be checked that the expansion velocity obtained in this manner is indeed much larger than the sound velocity in the freely expanding supernova remnant.

3.3 Pulsar Wind Nebula in a Sedov-Taylor remnant

3.3.1 The case of a constant wind luminosity

Towards the end of the free expansion stage a reverse shock is driven deep into the interior of the SNR. This reverse shock reheats the stellar ejecta, and as a result the sound velocity increases by a large factor. When the reverberations due to reflections of the reverse shock have almost completely dissipated, one can approximate the interior of the SNR by using the analytical Sedov solution (Sedov 1959).

The interaction with the reverse shock influences the evolution of the pulsar wind nebula quite dramatically. Cioffi et al. (1988) have already shown in their 1D simulation of a pure shell SNR that the reverse shock gives rise to all kinds of sound waves and weak shocks traveling back and forth through the ejecta before the interior relaxes towards a Sedov solution. We will show that during the process of relaxation the radius of the pulsar wind nebula contracts and expands due to reverberations of the reverse shock. Compression waves are

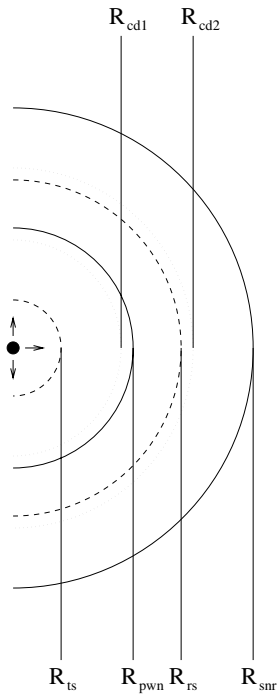


Figure 3.1: Schematic representation of PWN in a freely expanding SNR. There are a total of four shocks and two contact discontinuities. From left to right one can see: the pulsar wind termination shock R_{ts} (dashed line), the first contact discontinuity R_{cd1} (dotted line) separating shocked pulsar wind material from shocked ejecta, the PWN shock R_{pwn} (solid line) bounding the PWN. For the SNR we have a reverse shock R_{rs} (dashed line), the second contact discontinuity R_{cd2} (dotted line) separating shocked ejecta from shocked ISM, and the SNR shock R_{snr} (solid line) which is the outer boundary of the PWN/SNR system.

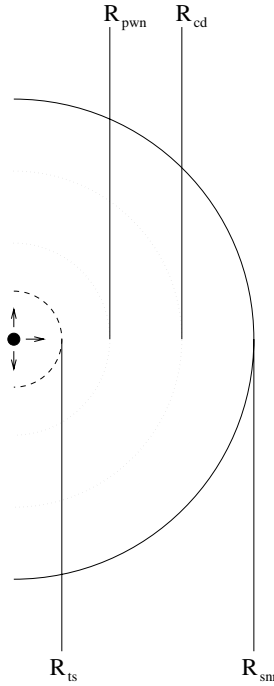


Figure 3.2: Schematic representation of a PWN in a Sedov SNR. There are a total of 2 shocks and 2 contact discontinuities. From left to right one can see: the pulsar wind termination shock R_{ts} (dashed line), the first contact discontinuity R_{pwn} (dotted line) separating shocked pulsar wind material from shocked ejecta, bounding the PWN. Furthermore there is another contact discontinuity R_{cd} (dotted line) separating shocked ejecta from shocked ISM, and the SNR shock R_{snr} (solid line) which bounds the PWN/SNR system.

partly reflected and partly transmitted at the edge of the PWN. We will come back to this point when we discuss results from hydrodynamics simulations in section 3.4, which allow a more detailed picture of this process.

In this Section we consider a fully relaxed Sedov SNR. The PWN expands subsonically into the remnant because the interior of the SNR has been reheated by the reverse shock. For the case of a constant (mechanical) luminosity driving the pulsar wind an analytical expression for the radius of the PWN can be easily obtained. In this stage of the PWN evolution, we associate its radius R_{pwn} with the contact discontinuity separating pulsar wind material from the ejecta of the progenitor star (see figure 3.2). We first present an order-of-magnitude calculation which leads to the correct power-law solution for the radius

of the PWN. The assumption of subsonic expansion implies approximate pressure equilibrium between the wind material and the stellar ejecta at the edge the PWN. In the interior of the SNR the pressure scales as

$$P_{\text{snr}} \propto E_0/R_{\text{snr}}^3 . \quad (3.14)$$

On the other hand, the pressure in the interior of the PWN scales as

$$P_{\text{pwn}} \propto L_0 t/R_{\text{pwn}}^3 , \quad (3.15)$$

with L_0 the mechanical luminosity driving the wind. Pressure equilibrium at the contact discontinuity at R_{pwn} implies the following relation for the radius of the PWN as a function of time:

$$R_{\text{pwn}}(t) = \bar{C} \left(\frac{L_0 t}{E_0} \right)^{1/3} R_{\text{snr}}(t) \propto t^{11/15} , \quad (3.16)$$

with the constant of proportionality \bar{C} to be determined below.

A more detailed derivation uses the first law of thermodynamics, assuming once again a constant energy input L_0 into the PWN by the pulsar-driven wind:

$$dE_{\text{th}} = L_0 dt - P_i d\mathcal{V}_{\text{pwn}} . \quad (3.17)$$

Here E_{th} is the thermal energy of the PWN, P_i its internal pressure, and \mathcal{V}_{pwn} its volume. This yields the following equation describing the energy balance of a slowly expanding PWN:

$$\frac{d}{dt} \left(\frac{4\pi}{3} \frac{P_i R_{\text{pwn}}^3}{(\gamma_{\text{pwn}} - 1)} \right) = L_0 - 4\pi R_{\text{pwn}}^2 P_i \left(\frac{dR_{\text{pwn}}}{dt} \right) , \quad (3.18)$$

or equivalently:

$$\frac{d}{dt} \left(\frac{4\pi}{3} \frac{\gamma_{\text{pwn}} P_i R_{\text{pwn}}^3}{(\gamma_{\text{pwn}} - 1)} \right) = L_0 + \frac{4\pi}{3} R_{\text{pwn}}^3 \left(\frac{dP_i}{dt} \right) . \quad (3.19)$$

This equation has a power-law solution for $R_{\text{pwn}}(t)$ provided the internal pressure $P_i(t)$ in the SNR behaves as a power-law in time so that the relation

$$R_{\text{pwn}}^3 \left(\frac{dP_i}{dt} \right) = \text{constant} \quad (3.20)$$

can be satisfied. For a Sedov SNR expanding into a uniform ISM one has $P_i \propto t^{-6/5}$ and one finds:

$$R_{\text{pwn}}(t) = D \left(\frac{L_0 t}{P_i(t)} \right)^{1/3} \propto t^{11/15}, \quad (3.21)$$

where

$$D = \left[\frac{4\pi}{3} \left(\frac{\gamma_{\text{pwn}}}{\gamma_{\text{pwn}} - 1} + \frac{6}{5} \right) \right]^{-1/3}. \quad (3.22)$$

If $R_{\text{pwn}} \ll R_{\text{snr}}$ we can use the central pressure from the Sedov solution with $\gamma_{\text{ism}} = 5/3$ for the interior pressure in the SNR which confines the PWN (e.g. Shu, 1992):

$$P_i(t) = P_{\text{snr}}(t) \simeq 0.074 \left(\frac{E_0}{R_{\text{snr}}^3} \right) \propto t^{-6/5}. \quad (3.23)$$

We find the same result for $R_{\text{pwn}}(t)$ as in the order-of-magnitude calculation (Eqn. 3.16), determining the constant in that expression as $\bar{C} \simeq 0.954$ for a non-relativistic fluid ($\gamma_{\text{pwn}} = 5/3$) and $\bar{C} \simeq 0.851$ for a relativistic fluid ($\gamma_{\text{pwn}} = 4/3$). By comparing the sound speed with the expansion velocity at the edge of the PWN, we confirm that the expansion remains subsonic.

An alternative derivation of the PWN expansion law uses the Kennel-Coroniti model for a highly relativistic pulsar-driven pair wind. This wind is terminated by a strong MHD shock which decelerates the fluid to a nonrelativistic expansion speed (Rees & Gunn, 1974). Kennel & Coroniti (1984, hereafter K&C) constructed a steady, spherically symmetric MHD model for the Crab nebula which includes these characteristics. We use their model in the hydrodynamical limit by considering the case

$$\sigma \equiv \frac{\text{Poynting flux}}{\text{particle energy flux}} \rightarrow 0. \quad (3.24)$$

K&C assume a constant wind luminosity,

$$L_0 = 4\pi n_1 \Gamma_1 u_1 R_{\text{ts}}^2 mc^2 \approx 4\pi n_1 \Gamma_1^2 R_{\text{ts}}^2 mc^3, \quad (3.25)$$

where n_1 is the proper density just in front of the termination shock, $u = \Gamma_1 v \approx \Gamma_1 c$ is the radial four-speed of the wind and R_{ts} is the distance from the pulsar to the termination shock. Because the wind is assumed to consist solely of a positronic plasma, m is the electron mass. The pulsar wind is highly relativistic ($\Gamma_1 \gg 1$) and the thermal and rest energy of the particles can be neglected compared with the bulk kinetic energy. The total number of particles emitted into the PWN then equals:

$$N(t) = \frac{L_0 t}{\Gamma_1 mc^2}. \quad (3.26)$$

It is believed that the bulk Lorentz factor $\Gamma_1 \approx 10^6$, but we will see that for purposes of the PWN evolution its precise value is not important, because it cancels in the final result.

After the termination of the cold wind by a strong standing shock at some radius R_{ts} , the wind flow is subsonic, with a sound speed close to the speed of light. Assuming that the shock radius R_{ts} is much smaller than the radius R_{pwn} of the PWN, and assuming a uniform density n_2 and uniform pressure P_2 inside the PWN, particle conservation implies

$$\frac{4\pi}{3} n_2 R_{\text{pwn}}^3(t) = \frac{L_0 t}{\Gamma_1 mc^2}. \quad (3.27)$$

From the K&C model we take the following relationships, valid at the strong relativistic termination shock at the inner edge of the PWN in the hydrodynamical limit:

$$n_2 = \sqrt{8} n_1 \Gamma_1, \quad P_2 = \frac{2}{3} n_1 \Gamma_1^2 mc^2 \approx \frac{L_0}{6\pi R_{\text{ts}}^2 c}. \quad (3.28)$$

The subscripts 1 and 2 label upstream and downstream parameters on either side of the termination shock. Using these jump conditions together with equations (3.25) and (3.26) we can express $R_{\text{pwn}}(t)$ as a function of $R_{\text{ts}}(t)$:

$$R_{\text{pwn}}(t) = \left(\frac{3ct}{\sqrt{8}} \right)^{1/3} R_{\text{ts}}^{2/3}(t). \quad (3.29)$$

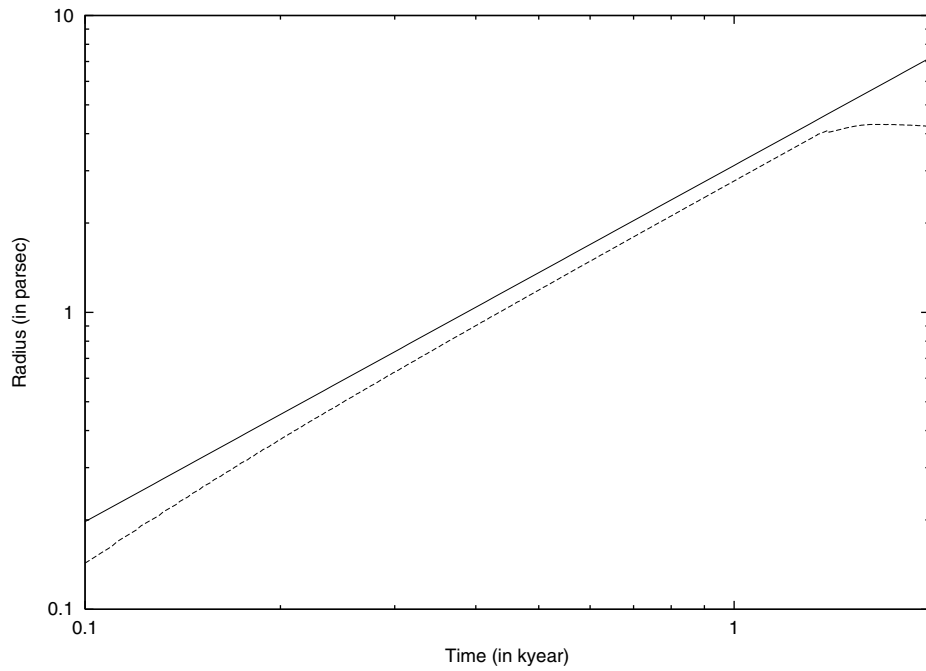


Figure 3.3: Comparison between results from numerical simulations and analytical result for the radius of the PWN, i.e. equation (3.12). The dashed line indicates the radius for the PWN obtained from numerical simulations. The solid line corresponds to equation (3.12) with $C \simeq 0.941$, as appropriate for $\gamma_{\text{pwn}} = 5/3$. The different physical parameters are as indicated in Table 1 (Simulation 1). The injected mass of the pulsar wind has been chosen in such a way that the termination velocity of the pulsar wind equals the speed of light. One can see that in the simulation the radius R_{pwn} is about 10 % smaller than predicted by the analytical result, but the power-law behaviour $R_{\text{pwn}} \propto t^{6/5}$ is correctly reproduced.

The pressure inside the PWN is nearly uniform. At the termination shock (inner edge of the PWN) it must equal the downstream pressure P_2 . At the outer edge of the PWN this pressure must approximately equal the pressure $P_{\text{snr}}(t)$ at the center of the SNR as given by Eqn. (3.23). Using (3.28) and (3.29) the inner and outer boundary conditions imply the following relation for the termination shock radius:

$$R_{\text{ts}}(t) \simeq 0.847 \left(\frac{L_0}{E_0 c} \right)^{1/2} R_{\text{snr}}^{3/2}(t). \quad (3.30)$$

It is now straightforward to obtain the radius of the PWN from (3.29) and (3.30). The resulting expression for R_{pwn} satisfies equation (3.16) with $\bar{C} \simeq 0.911$. This derivation based on (ram) pressure balance at the inner and outer edges of the pulsar wind nebula confirms our earlier result obtained from overall energy conservation.

3.3.2 The case of a varying wind luminosity

The constant wind luminosity assumption is not very realistic by the time the effects of the reverse shock and its associated reverberations have vanished. The spin-down luminosity of the pulsar is more realistically described by the luminosity evolution from a rotating magnetic dipole model:

$$L(t) = \frac{L_0}{\left(1 + \frac{t}{\tau}\right)^2}. \quad (3.31)$$

Therefore we now consider the more realistic case of a time-dependent luminosity given by (3.31). The energy balance equation for the PWN reads:

$$\frac{d}{dt} \left(\frac{4\pi}{3} \frac{P_i R_{\text{pwn}}^3}{(\gamma_{\text{pwn}} - 1)} \right) = \frac{L_0}{(1 + t/\tau)^2} - 4\pi R_{\text{pwn}}^2 P_i \left(\frac{dR_{\text{pwn}}}{dt} \right). \quad (3.32)$$

We solve this equation numerically using a fourth-order Runge-Kutta method (e.g. Press et al., 1992). As an initial condition we take the radius of the PWN equal to zero at the start of the evolution, neglecting the initial stage when the PWN is expanding supersonically. For the pressure P_i , we use the pressure at the center of the Sedov SNR (3.23). We find that the solution for R_{pwn} converges to $R_{\text{pwn}} \propto t^{0.3}$ on a time scale much larger than the typical time scale for the reverse

shock to hit the edge of the PWN. Figure 3.9 shows this semi-analytical result together with results from hydrodynamical simulations. For the semi-analytical equation we use $\gamma_{\text{pwn}} = 5/3$, because the hydrodynamics code also uses this value (see section 3.4.1 below).

3.4 Numerical simulations

3.4.1 Method

Our simulations were performed using the Versatile Advection Code (VAC, Tóth 1996) which can integrate the equations of gas dynamics in a conservative form in 1, 2 or 3 dimensions. We used the TVD-MUSCL scheme with a Roe-type approximate Riemann solver from the numerical algorithms available in VAC (Tóth and Odstrčil, 1996); a discussion of this and other schemes for numerical hydrodynamics can be found in LeVeque (1998). In this paper our calculations are limited to spherically symmetric flows.

We use a uniform grid with a grid spacing chosen sufficiently fine to resolve both the shocks inside the PWN and the larger-scale shocks associated with the SNR. Table 1 gives the physical scale associated with the grid size for the simulations presented here. An expanding SNR is created by impulsively releasing the mechanical energy of the SN explosion in the first few grid cells. The thermal energy and mass deposited there lead to freely expanding ejecta with a nearly uniform density, and a linear velocity profile as a function of radius.

A realistic shocked pulsar wind is presumably highly relativistic with an adiabatic heat ratio $\gamma_{\text{pwn}} = 4/3$. The (shocked) stellar ejecta on the other hand are non-relativistic with $\gamma_{\text{ej}} = 5/3$.

The VAC code does not currently include relativistic hydrodynamics. Therefore, the best approach available to us is to keep $\gamma_{\text{pwn}} = 5/3$, but to take a luminosity for the pulsar wind, $L(t)$, and an associated mass injection, $\dot{M}_{\text{pw}}(t)$, such that the terminal velocity obtained from these two parameters,

$$v_{\infty} = \sqrt{2L(t)/\dot{M}_{\text{ej}}(t)}, \quad (3.33)$$

roughly equals the speed of light. Since the pulsar wind material downstream of the termination shock moves with only a mildly relativistic bulk speed we expect our results to be qualitatively correct. Thermal energy and mass are deposited continuously in a small volume as a source for the wind. The hydrodynamics

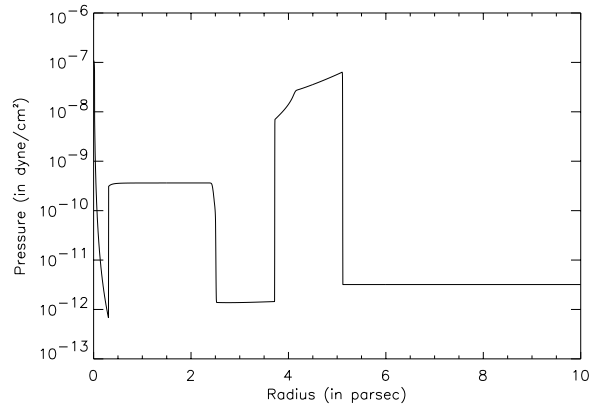


Figure 3.4: *Pressure profile of the PWN/SNR system as a function of radius, at time $t = 1000$ years after the SN explosion. Physical parameters are as indicated in Table 1 (Simulation 2). Moving outwards in radius one can see the wind termination shock, the shock bounding the PWN, the reverse shock of the SNR and the shock bounding the SNR. The interior of the PWN is nearly isobaric. There is a sudden increase in pressure of the ejecta behind the SNR reverse shock.*

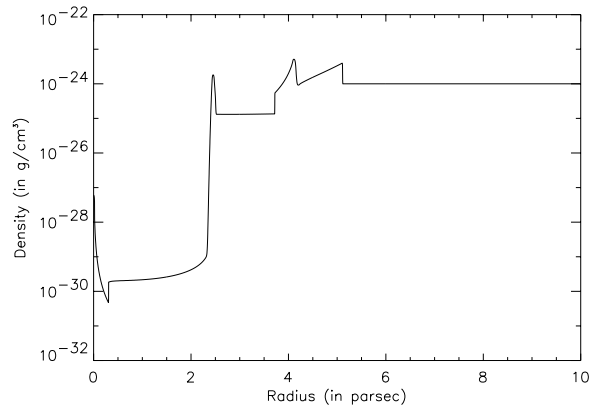


Figure 3.5: *Density profile for the same PWN/SNR system as in figure 3.4.*

Table 1: Simulation parameters

| | Simulation 1 | Simulation 2 | Simulation 3 |
|--|--------------------|--------------|--------------------|
| Explosion energy E_0 (erg) | 10^{51} | 10^{51} | 10^{51} |
| Ejecta mass $M_{\text{ej}}(M_{\odot})$ | 3 | 3 | 3 |
| Pulsar wind luminosity L_0 (erg/s) | 5×10^{38} | 10^{38} | 5×10^{38} |
| Spin-down time τ (yr) | ∞ | 600 | 600 |
| ISM mass density ρ_0 (g/cm ³) | 10^{-24} | 10^{-24} | 10^{-24} |
| Number of grid cells | 5000 | 5000 | 3000 |
| Grid size (pc) | 0.002 | 0.002 | 0.01 |

code then develops a steady wind reaching the terminal velocity v_{∞} well before the (cold) wind is terminated by the standing termination shock.

We trace the total mass injected into the PWN by the pulsar wind in order to determine the radius of the contact discontinuity which separates the pulsar wind material from the SN ejecta (R_{cd1} in figure 1 and R_{pwn} in figure 2). We also determine the position of the shock bounding the PWN during the stage of supersonic expansion. This enables us to compare the numerical results with the analytical expressions derived in sections 2 and 3 for the PWN radius.

As a test of the code we have calculated a pulsar wind driven by a constant luminosity L_0 (Simulation 1 in Table 1). We let the PWN evolve until the reverse shock propagating in the SNR hits its outer edge. Figure 3.3 shows the radius of the shock of the PWN together with the analytical equation (3.16). We take $\gamma_{\text{pwn}} = 5/3$ in the analytical expressions for comparison with the numerical results. Although the analytical result of Eqn. (3.16) is not reproduced exactly (the radius is about 10% smaller), the power-law expansion law $R_{\text{pwn}} \propto t^{6/5}$ is reproduced. As we will show in section 3.4.2, the pressure inside the bubble is larger than the one used to derive the equation, explaining the difference between the analytical and numerical results.

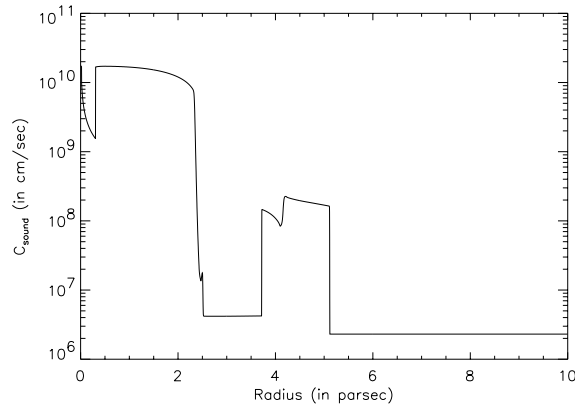


Figure 3.6: *Sound velocity profile as a function of radius, for the same case as in figures 3.4 and 3.5. Because of the Rankine-Hugoniot jump conditions at the wind termination shock, the sound velocity of the shocked wind material in the PWN bubble is close to the speed of light. Behind the contact discontinuity, where the bubble consists of swept-up ejecta, the sound speed has a smaller value.*

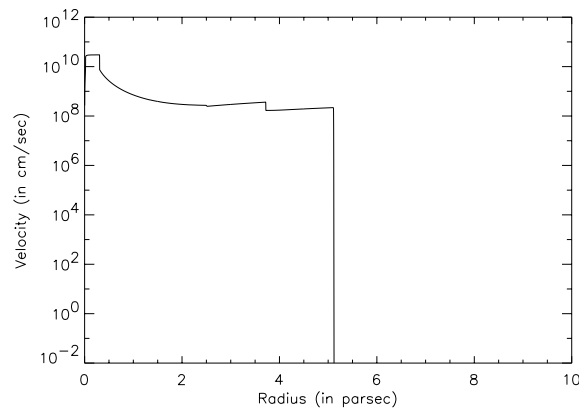


Figure 3.7: *Velocity profile for the PWN/SNR system with the same parameters. The terminal wind velocity, v_∞ , is close to the speed of light. The large jump in the velocity at a radius ~ 4 pc is the reverse shock which is still propagating forwards in the laboratory frame. The velocity jump of the PWN shock at radius ~ 2.5 pc is much smaller.*

3.4.2 Evolution of the PWN-SNR system into the Sedov phase

Our simulations of the evolution of a pulsar wind nebula inside a supernova remnant employ the parameters listed in Table 1.

In the early stage of its evolution the PWN is bounded by a strong shock propagating through the ejecta of the progenitor star. In figures 3.4–3.7 one can clearly identify the four shocks indicated schematically in figure 3.1. Moving outward in radius one first encounters the pulsar wind termination shock; this termination shock is followed by the PWN shock. In the sound velocity profile of figure 3.6 one can see a large jump between these two shocks: the contact discontinuity separating shocked pulsar wind material from shocked ejecta. Further outward one encounters the SNR reverse shock, which at this stage of the SNR evolution is still moving outwards from the point of view of a stationary outside observer. The whole PWN-SNR system is bounded by the SNR blast wave.

Figure 3.9 shows the evolution of the contact discontinuity radius R_{cd} , which can be identified with the radius of the PWN in the subsonic expansion stage. One can clearly see the moment at $t \simeq 1.75$ kyr when the reverse shock hits the edge of the PWN: the expansion becomes unsteady with the PWN contracting and expanding due to the interaction with the pressure pulses associated with the reverberations of the reverse shock. When these reverberations have almost dissipated the expansion of the PWN relaxes to a steady subsonic expansion. In this stage, we can fit the radius of the PWN obtained from the simulations with the (semi-)analytical solution obtained from a numerical integration of equation (3.18), as shown in this figure.

The interaction of the PWN with the reverse shock and the associated reverberations is quite complicated. We will therefore describe this process in more detail.

3.4.3 The influence of reverse-shock reverberations

The reverse shock initially encounters the PWN in its supersonic expansion stage. After the collision between the reverse shock and the PWN shock a reflected shock propagates back towards the outer (Sedov-Taylor) blast wave of the SNR. A transmitted shock propagates into the shocked ejecta inside the PWN. When this shock hits the contact discontinuity bounding the pulsar wind material a similar reflection/transmission event occurs: a shock moves radially outwards, and a compression wave moves into the pulsar wind material. The latter wave is

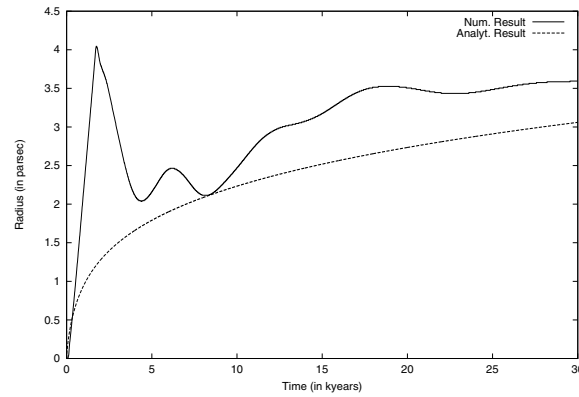


Figure 3.8: *The radius of the PWN contact discontinuity as a function of time (solid line). We compare with the semi-analytical solution from equation (3.32) (dashed line). Here one can see that the expansion of the PWN is unsteady, due to the reverberations of the reverse shock. This simulation was done with the parameters listed in Table 1 (Simulation 3).*

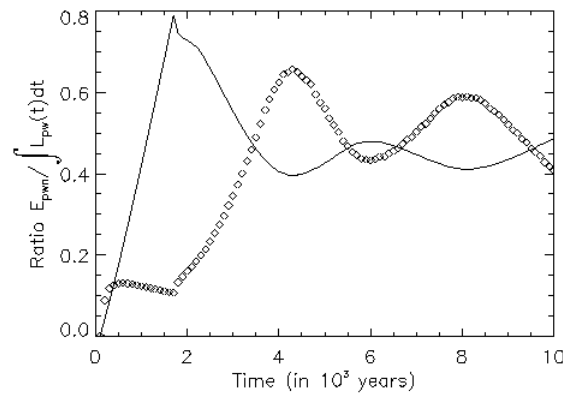


Figure 3.9: *The radius of the PWN as a function of time, together with the ratio of the total energy in the PWN bubble with respect to the total energy input by the pulsar wind. The solid line represents the radius of the contact discontinuity of the PWN (in arbitrary units), the open squares represent the aforementioned ratio of energy. This simulation was done with the parameters as listed in Table 1 (Simulation 3).*

rapidly dissipated in the pulsar wind bubble because of the high sound speed in the shocked pulsar wind. After a few sound crossing times the pulsar wind bubble contracts adiabatically in response to the pressure increase inside the SNR. After this contraction it regains pressure equilibrium with the surrounding SNR and the PWN expands subsonically henceforth. This chain of events can be clearly seen in figure 3.8 where we plot the radius of the PWN. The whole process takes a time comparable with the duration of the initial supersonic expansion stage.

3.4.4 Subsonic expansion stage

When the PWN has more or less relaxed to a steady subsonic expansion the PWN has gained energy as a result of the interaction with the reverse shock. Consequently, the radius of the PWN is roughly 20% larger than the value predicted by the semi-analytical solution obtained from Eqn. (3.18) in Section 3.2. In figure 3.9 we show the ratio between the (mostly thermal) energy of the pulsar wind bubble, i.e. the part of the PWN that consists of shocked pulsar wind material, and the total mechanical energy deposited by the pulsar. One can clearly see the increase in the energy content of the pulsar wind bubble. A large fraction of the energy deposited by the pulsar wind in the stage when the expansion is supersonic is contained in the kinetic energy of the shocked stellar ejecta in the PWN shell. When the reverse SNR shock is interacting with the PWN bubble, energy is apparently transferred from this thin shell to the interior of the bubble by the process of adiabatic compression. One can see the effect of adiabatic compression in Figure 3.9 where the radius of the PWN and the energy content of the PWN are anti-correlated.

3.5 Conclusions and discussion

We have considered a spherically symmetric PWN/SNR system in the early and middle stages of its evolution, well before cooling of the SNR shell becomes dynamically important and before a significant disruption of spherical symmetry due to a possible (large) kick velocity of the pulsar can take place. The expansion of the PWN is coupled with the dynamics of the expanding SNR, leading to two distinct evolutionary stages separated by an unsteady transition phase:

- When the PWN is surrounded by the freely expanding ejecta of the SNR, the expansion of the PWN is supersonic. In this stage the pressure in the

interior of the PWN bubble is slightly larger than one would expect from ram pressure of the surrounding ejecta alone, using the Rankine-Hugoniot relations at the PWN shock. This is due to the thin shell of shocked, swept-up ejecta which needs to be accelerated by the outward force due to the interior pressure of the PWN.

- This stage of supersonic expansion is ultimately followed by a subsonic expansion of the PWN. This happens after the reverse shock has encountered the shock of the PWN.
- The transition between these two stages is unsteady due to the interaction of the PWN with the reverse shock and its associated reverberations. From the hydrodynamical simulations we see that the time scale for adjustment to the pressure of the surrounding SNR is determined by the sound speed of the ejecta shocked by the PWN in the first stage.

Two of the prototypes of plerionic SNRs are the Crab Nebula and 3C58. In the Crab, there is a decrease in the radio flux of $0.167 \pm 0.015 \text{ \% yr}^{-1}$ (Aller & Reynolds 1985). By contrast, 3C58 shows an increase in its flux density at radio frequencies between 1967 and 1986 (Green 1987). This increase might be the result of the reverse shock which has encountered the PWN shock around 3C58; the PWN is being compressed and therefore the flux density is going up.

Our numerical simulations are different from the results presented by Jun (1998). This author concentrates on the details of the PWN in the supersonic expansion stage, and in particular on the formation of Rayleigh-Taylor fingers in his two-dimensional simulations. Our simulations include the whole supernova remnant, but can not address the development of Rayleigh-Taylor instabilities due to our assumption of spherical symmetry.

In future work we will discuss how these results change when the influence of a significant kick velocity of the pulsar is taken into account. If this is taken into account, the model presented here will lose its validity at a certain time: one can calculate when the motion of a pulsar will become supersonic in a Sedov stage. One can show that this will happen when the pulsar is about halfway from the explosion center to the edge of the SNR: a bow shock is expected to result from this and clearly the model presented here will break down. Observationally there is evidence that this is the case for the pulsar associated with the SNR W44.

Bibliography

- [1] Aller, H.D., Reynolds, S.P. 1985, ApJ, 293, L73
- [2] Chevalier, R.A. 2000, ApJ,, 539, L45
- [3] Chevalier, R.A., Fransson, C. 1992, ApJ, 395, 540
- [4] Cioffi, D.F., McKee, C.F., Bertschinger, E. 1988, ApJ, 334, 252
- [5] Cioffi, D.F. 1990, in: Physical Processes in Hot Cosmic Plasmas, Brinkmann, W., Fabian, A.C. & Giovanelli, F. (Eds), Kluwer Academic Publ., Dordrecht, Holland, p. 1.
- [6] Frail, D.A., Moffett, D.A. 1993, ApJ, 408, 637
- [7] Frail, D.A., Goss, W.M., Whiteoak, J.B.Z. 1994, ApJ, 437, 781
- [8] Frail, D.A., Giacani, E.B., Goss, W.M., Dubner, G. 1996, ApJ, 464, L165
- [9] Frail, D.A., Scharringhausen, B.R. 1997, ApJ, 480, 364
- [10] Green, D.A. 1987, MNRAS, 225, 11
- [11] Hester et al. 1996, ApJ, 456, 225
- [12] Hester, J.J., Kulkarni, S.R. 1988, ApJ, 331, L121
- [13] Jun, B-I. 1998, ApJ, 499, 282.
- [14] Kennel, C.F., Coroniti, F.V. 1988, ApJ, 283, 694
- [15] LeVeque, R.J. 1998, in: *Computational Methods for Astrophysical Fluid Flow*, Saas Fee Adv. Course 27, R.J. LeVeque, D. Mihalas, E.A. Dorfi & E. Müller (Eds.), p.1, Springer Verlag, Heidelberg

-
- [16] McKee, C.F. 1974, ApJ, 188, 335
 - [17] McKee, C.F., & Truelove, J.K. 1995, Phys. Rep., 256, 157
 - [18] Press et al. 1992, *Numerical recipes in C*, Cambridge University Press, New York
 - [19] Rees, M.J., Gunn, J.E. 1974, MNRAS, 167, 1
 - [20] Reynolds, S.P., and Chevalier, R.A. 1984, ApJ, 278, 630
 - [21] Sankrit, R., and Hester, J.J. 1997, ApJ, 491, 796
 - [22] Sedov, L.I. 1959, *Similarity and Dimensional Methods in Mechanics*, Academic, New York
 - [23] Shu, F.H. 1992, *The Physics of Astrophysics: Volume II Gas Dynamics*, University Science Books, Mill Valley
 - [24] Strom, R.G. 1987, ApJ, 319, L103
 - [25] Tóth, G. 1996, Astrophys. Lett. & Comm., 34, 245
 - [26] Tóth, G. & Odstrčil 1996, J. Comp. Phys. 128, 82
 - [27] Woltjer, L. 1972, ARA&A, 10, 129

Chapter 4

Interaction of high-velocity Pulsars with old Supernova Remnants

E. van der Swaluw, A. Achterberg and Y. A. Gallant

abstract

Hydrodynamical simulations are presented of a pulsar wind associated with a supersonically moving pulsar. The pulsar moves through the interstellar medium or, in the more interesting case, through the supernova remnant created at its birth event. In both cases there exists a bow shock around the pulsar wind nebula. Using hydrodynamical simulations we study the behaviour of the pulsar wind nebula inside a supernova remnant, and in particular the interaction with the outer shell of swept-up interstellar matter and the blast wave bounding the remnant which occurs when the pulsar breaks out of the supernova remnant.

4.1 Introduction

A supernova explosion of a massive star will result in an expanding supernova remnant (SNR). In some cases the fossil of the progenitor star is a pulsar moving at high velocity. Even though the precise physical mechanism responsible for imparting a large kick velocity to single radio pulsars at birth has not been identified, observations of the pulsar distribution with respect to the plane of the galaxy indicate that they are born with a velocity in the range $V_{\text{psr}} \sim 100 - 1000$ km/s (Harrison et al. 1992; Lyne & Lorimer 1994). A similar range of values is obtained from a sample of SNR-pulsar associations (Frail et al. 1994).

The expansion of a SNR is decelerated due to the mass-loading by the swept-up interstellar medium (ISM) or by material from a progenitor wind. As the pulsar moves with a constant velocity it will ultimately break through the SNR shell. Two observed systems are often presented as an illustration of this scenario:

CTB80: in this supernova remnant the pulsar *PSR 1951+32* is located (in projection) just inside the outer edge of the remnant. The spectral index of the synchrotron emission in the vicinity of the pulsar system indicates that there is a plerion around the pulsar, see for example Strom (1987) and Strom & Stappers (2000).

G5.4-1.2: in this case the pulsar is located well outside the supernova remnant. At radio frequencies an emission bridge connects the pulsar *B1757-24* and the associated pulsar wind nebula (PWN) with the supernova remnant (Frail & Kulkarni 1991). New upper limits on the proper motion of *B1757-24* (Gaensler & Frail 2000), which put the transverse component of the pulsar velocity at $V_{\perp\text{psr}} \leq 600$ km/s for an assumed distance of 5 kpc, leads to a discrepancy between the characteristic pulsar age obtained from its spin period derivative ($P/2\dot{P} \sim 16$ kyr) and the dynamical age obtained from the offset distance R_{psr} from the center of *G5.4-1.2* ($R_{\text{psr}}/V_{\text{psr}} \sim 39$ kyr).

Both systems are clearly brightened at radio wavelengths near the position of the pulsar, suggesting that the associated pulsar wind is rejuvenating the radio emission from the SNR shell by the injection of fresh relativistic electrons (Shull et al. 1989). In this chapter we will investigate the hydrodynamical aspects of the interaction between a pulsar wind and a SNR shell. In chapter 6 we will discuss the question of rejuvenation of the radio-emitting electrons.

Most pulsars have a lifetime ($10^6 - 10^7$ yr) which is much larger than the age $\leq 10^4$ yr of a SNR in the Sedov phase. Therefore pulsars will remain visible long after the associated SNR has dissolved into the interstellar medium and is no longer visible. In that case an isolated pulsar will move through the interstellar medium, and can form a pulsar wind nebula bow shock system. A typical example of such a system is the *Guitar Nebula* around *PSR 2224+65* which has been detected both in X-rays (Romani et al. 1997) and in $H\alpha$ (Cordes et al. 1993), but which has no associated SNR.

In this chapter we consider the case where the pulsar's kick velocity is sufficiently high so that it leaves the supernova remnant while it is still in the Sedov stage. We describe three different stages in the evolution of the pulsar-SNR system: (1) the stage where the PWN/bow shock resides inside the SNR, (2) the PWN/bow shock breaking through the shell of the SNR and (3) the stage where the PWN/bow shock moves through the ISM.

4.2 Physics of a PWN bow shock inside a SNR

4.2.1 Dynamics of the pulsar/SNR system

In rapidly rotating (young or recycled) pulsars, it is believed that a pulsar wind is driven by the spindown luminosity,

$$L = I\Omega\dot{\Omega} ,$$

of a pulsar with rotation period $P = 2\pi/\Omega$ and moment of inertia I . This relativistic wind is presumably generated in the pulsar magnetosphere, and accelerates electrons, positrons and possibly nuclei to ultra-relativistic speeds.

The pulsar wind blows a bubble (pulsar wind nebula: PWN) into the surrounding medium. The PWN is initially located well within the interior of the SNR created at the birth of the neutron star. During the free expansion stage of the SNR evolution the typical expansion speed of the stellar ejecta as determined by the mechanical energy E_{snr} released in the explosion and the ejecta mass M_{ej} ,

$$V_{\text{ej}} \sim \sqrt{\frac{10}{3} \frac{E_{\text{snr}}}{M_{\text{ej}}}} \sim 10,000 \text{ km/s} ,$$

is generally much larger than the kick velocity of the pulsar. As a result the PWN is located relatively close to the center of the SNR at this stage.

Only when the SNR expansion slows down as it enters the Sedov stage after some $\sim 500 - 1,000$ yr, a situation is possible where the pulsar position becomes strongly excentric with respect to the SNR.

The Sedov stage of SNR expansion lasts until internal (radiative) cooling becomes important. The SNR then enters the so-called pressure-driven snowplow (PDS) stage. The relevant transition time is calculated by Cioffi et al. (1988):

$$t_{\text{PDS}} = 1.33 \times 10^4 E_{51}^{3/14} \zeta_m^{-4/15} n_0^{-4/7} \text{ yr.} \quad (4.1)$$

Here E_{51} is the explosion energy E_{snr} in units of 10^{51} ergs, ζ_m denotes the metallicity and n_0 is the number density in the ISM, assuming $n_{\text{He}}/n_{\text{H}} = 0.1$.

We will describe the physics of a pulsar wind interaction with the shell of a SNR in the Sedov stage. Since the proper motion of the pulsar is supersonic with respect to the surrounding medium the outer rim of the PWN will deform its shape which results in the formation of a bow shock. Consequently the results presented below only apply for certain range of values for the pulsar velocity V_{psr} . Equating the distance travelled by the pulsar,

$$R_{\text{psr}} = V_{\text{psr}} t ,$$

with the radius for a SNR embedded in a homogeneous interstellar medium of density ρ_{ism} in the Sedov stage,

$$R_{\text{snr}} \simeq 1.15 \left(\frac{E_{\text{snr}}}{\rho_{\text{ism}}} \right)^{1/5} t^{2/5} , \quad (4.2)$$

one gets the crossing time for the pulsar:

$$t_{\text{cr}} = 1.27 \left(\frac{E_{\text{snr}}}{\rho_{\text{ism}} V_{\text{psr}}^5} \right)^{1/3} \simeq 1.4 \times 10^4 E_{51}^{1/3} V_{1000}^{-5/3} n_0^{-1/3} \text{ yr.} \quad (4.3)$$

Here V_{1000} is the velocity of the pulsar in units of 1,000 km/sec, and n_0 the number density of the ISM in units of cm^{-3} . The requirement $t_{\text{cr}} \leq t_{\text{PDS}}$ yields the minimum velocity a pulsar needs in order to break out of the SNR while it is still in the Sedov stage:

$$V_{\text{psr}} \geq 1,030 \zeta^{4/25} n_0^{1/7} E_{51}^{1/14} \text{ km/s.} \quad (4.4)$$

Although this is a rather high value, it is still in the range of values observed by Harrison et al. (1992).

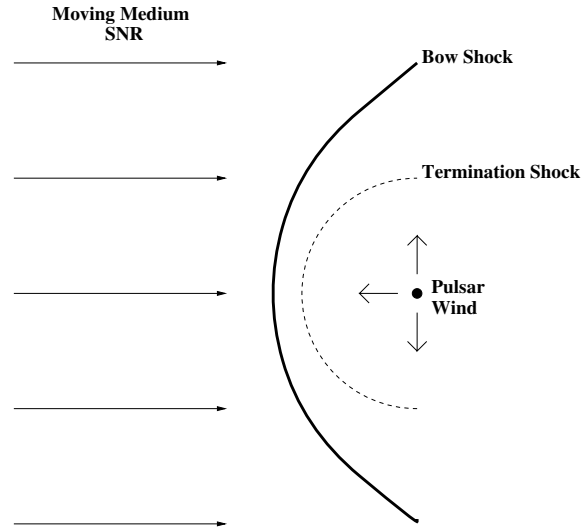


Figure 4.1: Configuration of the pulsar wind nebula moving through a uniform medium of the SNR, in the restframe of the pulsar.

One can use the Rankine-Hugoniot relations to determine the pressure just behind the Sedov-Taylor blast wave bounding the SNR (assuming a gas with specific heat ratio $\gamma = 5/3$)

$$P_{\text{sh}} = \frac{3}{4} \rho_{\text{ism}} V_{\text{snr}}^2, \quad (4.5)$$

where

$$V_{\text{snr}} \equiv \frac{dR_{\text{snr}}}{dt} = \frac{2}{5} \frac{R_{\text{snr}}}{t}$$

is the SNR expansion speed. Using this expression plus the expression (4.3) for the crossing time and the Sedov solution (4.2) one can derive the following equations valid at the moment of break-through. The speed of the pulsar is related to the SNR expansion speed by

$$V_{\text{psr}} = \frac{5}{2} V_{\text{snr}}, \quad (4.6)$$

while the material in the shell behind the SNR blast wave moves with a velocity

$$V_{\text{sh}} = \frac{3}{4} V_{\text{snr}}. \quad (4.7)$$

This corresponds to a relative speed between pulsar and post-shock material equal to

$$V_{\text{rel}} \equiv V_{\text{psr}} - V_{\text{sh}} = \frac{7}{4} V_{\text{snr}} . \quad (4.8)$$

The density in the shell is $\rho_{\text{sh}} = 4\rho_{\text{ism}}$, so the Mach number \mathcal{M}_{psr} of the pulsar motion through the shell material satisfies

$$\mathcal{M}_{\text{psr}} = \frac{V_{\text{rel}}}{\sqrt{\gamma P_{\text{sh}}/4\rho_{\text{ism}}}} = \frac{7}{\sqrt{5}} \approx 3.13 . \quad (4.9)$$

4.2.2 Pulsar Wind

A pulsar wind is believed to consist of an ultra-relativistic, cold flow with a large bulk Lorentz factor ($\Gamma_{\text{w}} \geq 10^6$) (Kennel & Coroniti 1984). In such a wind, the energy flux S and momentum flux M are approximately given by

$$M = \frac{S}{c} \approx \Gamma_{\text{w}}^2 n_{\text{w}} m c^2 , \quad (4.10)$$

where n_{w} is the proper density in the wind and m the mean mass per particle. The cold wind is terminated by a termination shock which thermalizes the flow, leading to a relativistically hot downstream state with sound speed $s \sim c/\sqrt{3}$. The typical pressure behind the ultra-relativistic termination shock, located at some radius R_{ts} , is (e.g. Blandford & McKee, 1976)

$$P_{\text{ts}} = \frac{2}{3} \Gamma_{\text{w}}^2 n_{\text{w}} m c^2 \approx \frac{L}{6\pi R_{\text{ts}}^2 c} . \quad (4.11)$$

The last equality in terms of the total luminosity L of the wind is approximate because of deviations of sphericity of the pulsar wind region, induced by the proper motion of the pulsar. The shocked pulsar wind material is separated from material that has gone through the bow shock by a contact discontinuity. Because of the high internal sound speed, both in the pulsar wind material and in the material that has passed through the bow shock, and because of the small size of the region between the termination shock and bow shock, the region between termination shock and bow shock can be considered to be isobaric to lowest approximation.

At the stagnation point at the head of the bow shock surrounding the PWN momentum flux conservation on the central streamline puts the pressure at

$$P_{\text{bs}} = \rho_{\text{sh}} V_{\text{rel}}^2 + P_{\text{sh}} = 13 \rho_{\text{ism}} V_{\text{snr}}^2 . \quad (4.12)$$

After the pulsar has broken through the shell the pulsar wind is completely confined by the ram pressure of the cold ISM and the stagnation-point pressure drops to

$$P_{\text{bs}} = \rho_{\text{ism}} V_{\text{psr}}^2 = \frac{25}{4} \rho_{\text{ism}} V_{\text{snr}}^2 , \quad (4.13)$$

a pressure reduction by roughly 50% as the pulsar leaves the SNR. The fact that the region between termination shock and bow shock is almost isobaric implies

$$P_{\text{bs}} \approx P_{\text{ts}} .$$

This determines the stand-off distance of the pulsar wind termination shock as

$$R_{\text{ts}} = \eta \left(\frac{L}{6\pi \rho_{\text{ism}} V_{\text{psr}}^2 c} \right)^{1/2} , \quad (4.14)$$

where the numerical factor η takes the value $\eta = \sqrt{25/52} \approx 0.693$ when the pulsar is still just inside the SNR, and $\eta = 1.0$ when the pulsar moves through the ISM. This is also the typical stand-off distance of the bowshock, which is always close to the termination shock at the head of the pulsar wind nebula.

These expressions allow us to calculate the relative size of the pulsar wind to the supernova remnant at the moment of break through. From the expression (4.3) for the crossing time one has

$$R_{\text{snr}}(t_{\text{cr}}) = V_{\text{psr}} t_{\text{cr}} = 13.6 E_{51}^{1/3} V_{1000}^{-2/3} n_0^{-1/3} \text{ pc} .$$

The termination shock radius is of order

$$R_{\text{ts}} \simeq 57.6 \eta L_{34}^{1/2} n_0^{-1/2} V_{1000}^{-1} \text{ AU} .$$

Here $L_{34} = L/(10^{34} \text{ erg/s})$. Note that the size of the SNR shell is much larger than the size of the PWN. For this reason we will neglect the curvature of the SNR blast wave and perform a hydrodynamical simulation where the pulsar moves with a Mach number of $\mathcal{M} = 3.13$ through the post-shock flow of a strong plane-parallel shock, ultimately crossing this shock into the unshocked medium.

Table 1: Simulation parameters

| | Simulation 1 |
|--|-----------------------|
| Pulsar wind luminosity L_0 (erg/s) | 1.3×10^{34} |
| ISM mass density ρ_0 (g/cm ³) | 1.0×10^{-24} |
| Terminal Velocity v_∞ (cm/sec) | 3.0×10^9 |
| Number of grid cells (in r-direction) | 300 |
| Number of grid cells (in z-direction) | 180 |
| Grid size (pc) (in r-direction) | 0.1 |
| Grid size (pc) (in z-direction) | 0.06 |

4.3 Hydrodynamics of the PWN bow shock

4.3.1 Simulation Method

We simulate a pulsar wind using the *Versatile Advection Code* (VAC), a non-relativistic hydrodynamics code developed by Gábor Tóth at the Astronomical Institute in Utrecht (Tóth & Odstrčil 1996). The configuration of interest is depicted in figure 1, showing both shocks which are of interest; the pulsar wind termination shock and the bow shock bounding the PWN. This system is assumed to be axially symmetric around the direction of motion of the pulsar. We use a TVD-Lax-Friedrich scheme to solve the equations of hydrodynamics in conservative form. (For an overview of different schemes see for example Le Veque 1998).

4.3.2 Starting a pulsar wind

The hydrodynamics code can only handle a non-relativistic fluid with a single equation of state. We use an ideal fluid with specific heat ratio $\gamma = 5/3$. We simulate the pulsar wind by continuously depositing thermal energy at a constant rate L (the spin-down luminosity) in a small volume, together with an associated

mass injection \dot{M}_{pw} . The hydrodynamics code itself then develops a wind with terminal velocity v_∞ before the wind is thermalized by a termination shock. The mechanical luminosity L and mass deposition rate \dot{M}_{pw} are chosen such that the terminal velocity of the wind as determined from these two parameters is close to the speed of light:

$$v_\infty = \sqrt{2L/\dot{M}_{\text{pw}}} \approx c.$$

This choice will result in the correct global behaviour of the PWN. This method is similar to the method as described in Van der Swaluw et al. (2001). We employ a non-uniform grid with largest resolution near the pulsar in order to resolve the pulsar wind. The radius of the termination shock, given by Eqn. (4.14) in the relativistic case, is replaced by its non-relativistic equivalent,

$$R_{\text{ts}} \approx \eta \left(\frac{L}{2\pi\rho_{\text{ism}}V_{\text{psr}}^2v_\infty} \right)^{1/2},$$

and will have roughly the correct value when $v_\infty \approx c$.

4.3.3 Steady PWN and bow shock in a uniform medium

Our calculations are performed in the pulsar rest frame. The pulsar wind nebula is allowed to evolve in a uniform medium, moving at a constant speed V_{psr} at large distances from the pulsar. This medium represents the interior of the supernova remnant (shocked ISM) close to the blast wave. The velocity V_{psr} is supersonic with respect to the internal sound speed of the medium so that a bow shock develops around the PWN. We let the hydrodynamics code evolve the system until the large-scale flow is steady.

In order to determine when the system is steady, we employ a recipe of Toth et al.(1998). This recipe compares all N_{var} flow variables at time t_i (denoted by $U_n(i|k)$ at grid point k) with their values at the previous time t_{i-1} . We then calculate the residue Res defined as

$$\text{Res} \equiv \sqrt{\frac{1}{N_{\text{var}}} \sum_{n=1}^{N_{\text{var}}} \frac{\sum_k [U_n(i+1|k) - U_n(i|k)]^2}{\sum_k U_n^2(i|k)}}, \quad (4.15)$$

and halt the calculation when Res has a value less than a predetermined critical value.

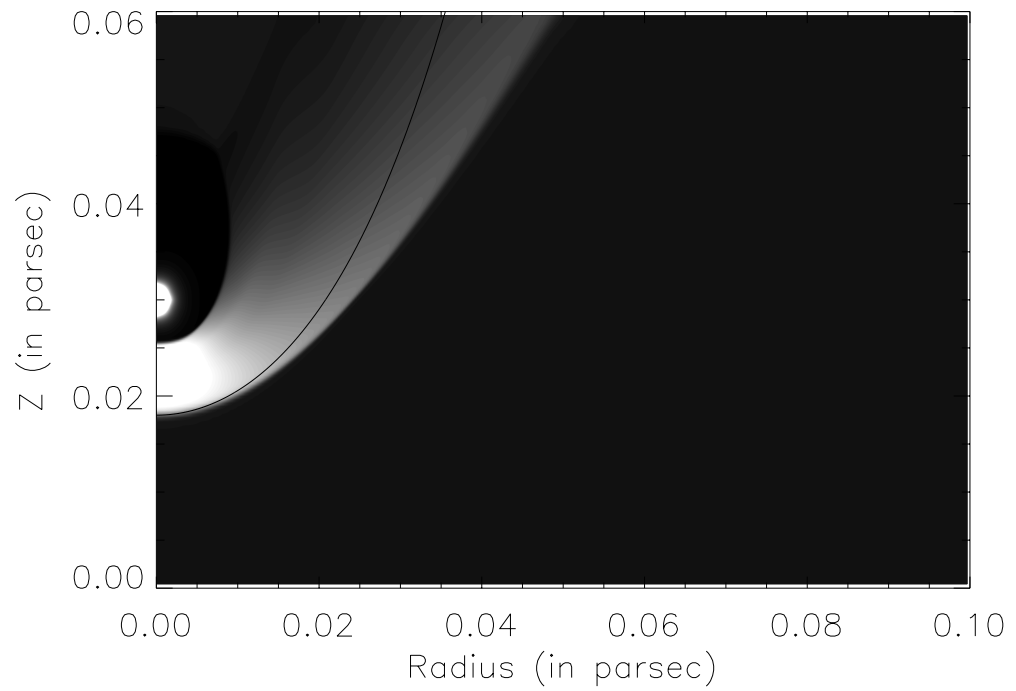


Figure 4.2: Comparison between the numerical result for the bow shock with a low Mach Number with the equation as given by Wilkin (1996). The contour plot gives the pressure profile, whereas the solid line is the profile as was given by Wilkin.

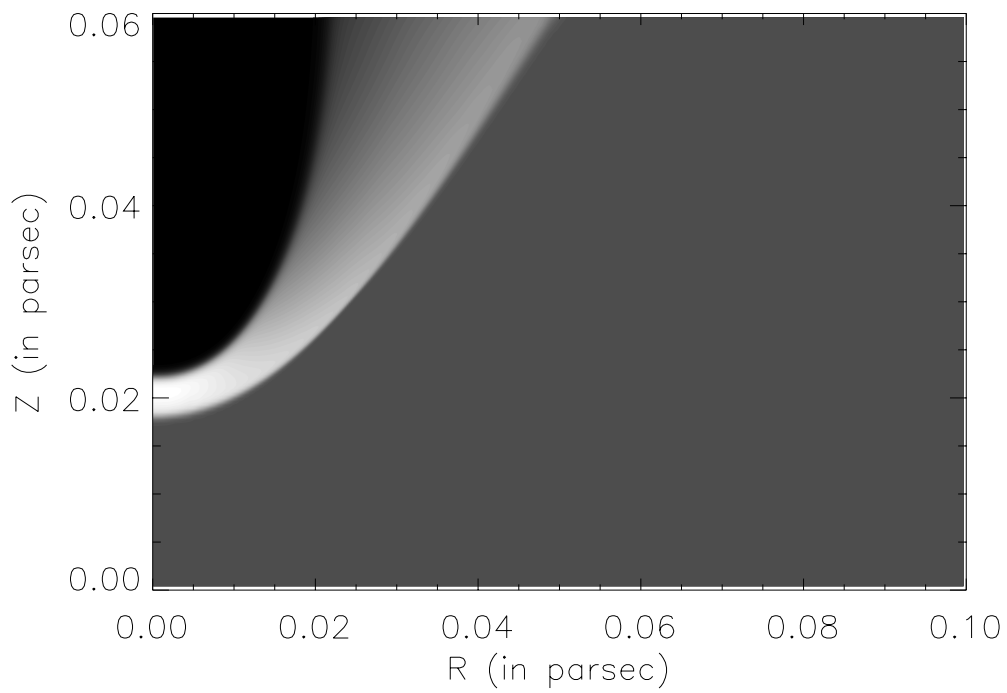


Figure 4.3: *Density profile of a PWN bow shock with the parameters as denoted in table 1. The gray-scale corresponds to the density.*

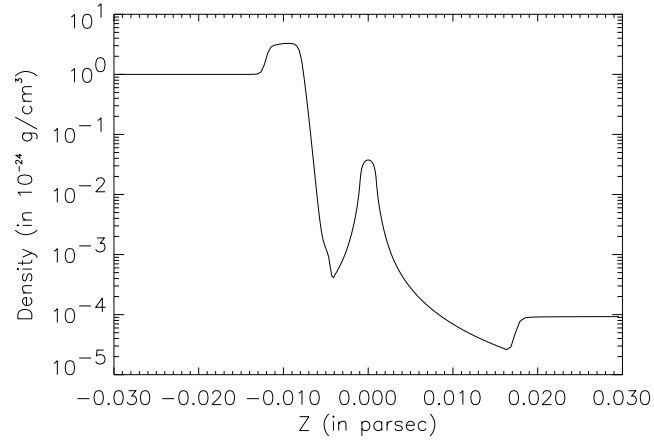


Figure 4.4: Density profile of a PWN bow shock where a cut has been made along the z -axis of Figure 4.3. In this figure, the pulsar's position corresponds to $Z=0$.

Wilkin (1996) has given an analytical equation for the geometry of a wind bow shock. His solution, in terms of the distance r to the wind source and polar angle θ with respect to the symmetry axis, reads:

$$\frac{r(\theta)}{R_0} \equiv \frac{1}{\sin \theta} \sqrt{3 \left(1 - \frac{\theta}{\tan \theta} \right)}. \quad (4.16)$$

Here $R_0 \approx R_{ts}$ is the stand-off distance of the bow shock on the symmetry axis ($\theta = 0$). We compare our morphology with Wilkin's result, where we equate R_0 to the stand-off distance of the bow shock in the simulations. This is depicted in figure 4.3. As one can see the cone of the geometry of Wilkin's solution is much narrower. This is because his solution comes from balancing the ram pressures of the wind and the ambient medium, i.e. the limit $\mathcal{M}_{psr} \gg 1$, while in our case the Mach number is moderate: $\mathcal{M}_{psr} \approx 3.13$.

The figures 4.3 and 4.4 show density profiles of the PWN bow shock of a pulsar moving through a uniform medium. One clearly sees the difference between shocked pulsar wind material and the much denser shocked ISM. The synchrotron emission coming from plerionic PWN is expected to come from the shocked pulsar wind material, whereas the material swept-up by the bow shock can show up as $H\alpha$ emission. Figure 4.5 shows the pressure distribution and

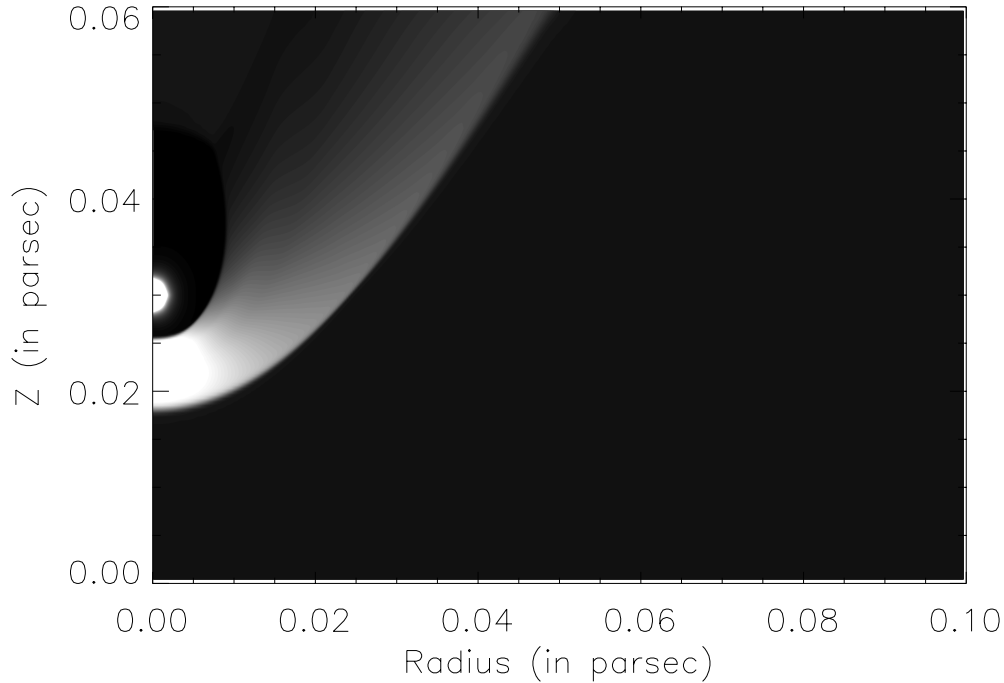


Figure 4.5: *Pressure profile of a PWN bow shock with the parameters as denoted in table 1. The gray-scale corresponds to pressure.*

figure 4.6 shows a pressure profile along the symmetry axis.

One can see the pulsar wind region around the pulsar, located at $z = 0$, the pulsar wind termination shock at $z \sim 0.025$ pc ahead of the pulsar in the direction of motion, and at $z \sim 0.042$ pc behind the pulsar. The bow shock bounding around the PWN at located at $z \sim -0.015$ pc. The region between the pulsar wind termination shock and the bowshock is almost isobaric. As shown by Van der Swaluw et al. (2001), this is also the case for a PWN around a stationary pulsar located at the center of the SNR.

4.3.4 Interaction of the PWN with a shock

In this section we present results of the break-through of the PWN bow shock through the shell of a supernova remnant. This results are again performed in

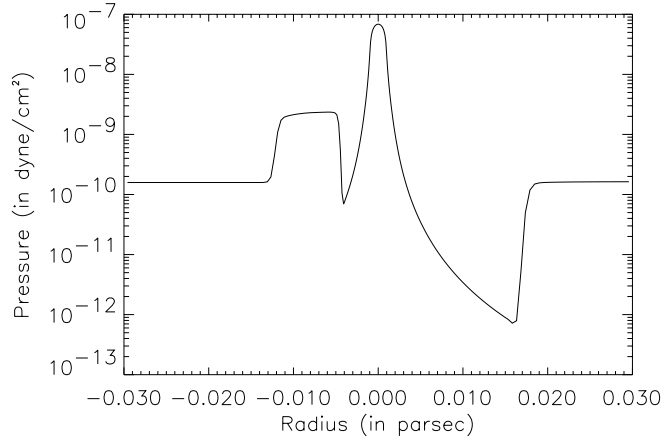


Figure 4.6: *Pressure profile of a PWN bow shock where a cut has been made along the z-axis of figure 4.3. In this figure, the pulsar's position corresponds to $Z = 0$.*

the rest frame of the pulsar. We initialise a steady-state configuration of the PWN bow shock as described above, and use the Rankine-Hugoniot relations to implement a strong shock front moving towards the pulsar such that equations (6)-(8) hold true. This simulation has been performed with parameters as denoted in table 1. At the end of the simulation, when the strong shock is almost at the upper boundary of the grid, numerical instabilities arise. Therefore we stop the simulation after the configuration as shown in the figures 4.7-4.9, when the influence of the numerical instabilities are not influencing the solution too strongly.

As stated in section 2, the PWN bow shock is much smaller than the radius of the SNR, so we can safely approximate the SNR blast wave as a plane-parallel strong shock. Figures 4.7 and 4.8 show the system after the SNR shock has passed the head of the bow shock. In figure 4.9 one can see that the pulsar wind nebula has expanded roughly by a factor 1.5 after it leaves the SNR. This reflects the reduction in the confining (ram-)pressure calculated in Section 4.2.

During the interaction between the pulsar wind and the shell of the SNR the PWN bow shock and the SNR blastwave intersect. This interaction produces an additional pressure gradient which results in an accumulation of mass. The pressure and density enhancements can be seen at the region of intersection in the figures 4.7 and 4.8 as bright spots. When the bow shock moves through the

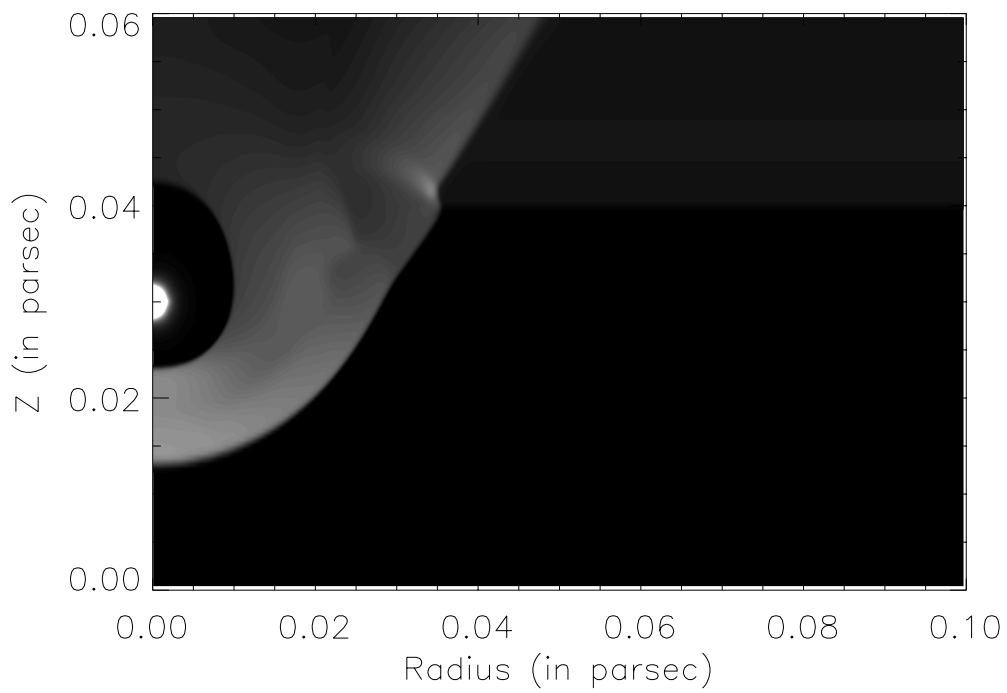


Figure 4.7: *Pressure profile of a PWN bow shock with the same parameters as denoted in table 1, except on a lower resolution. Here the PWN is interacting with the shell of the SNR. The gray-scale corresponds to pressure*

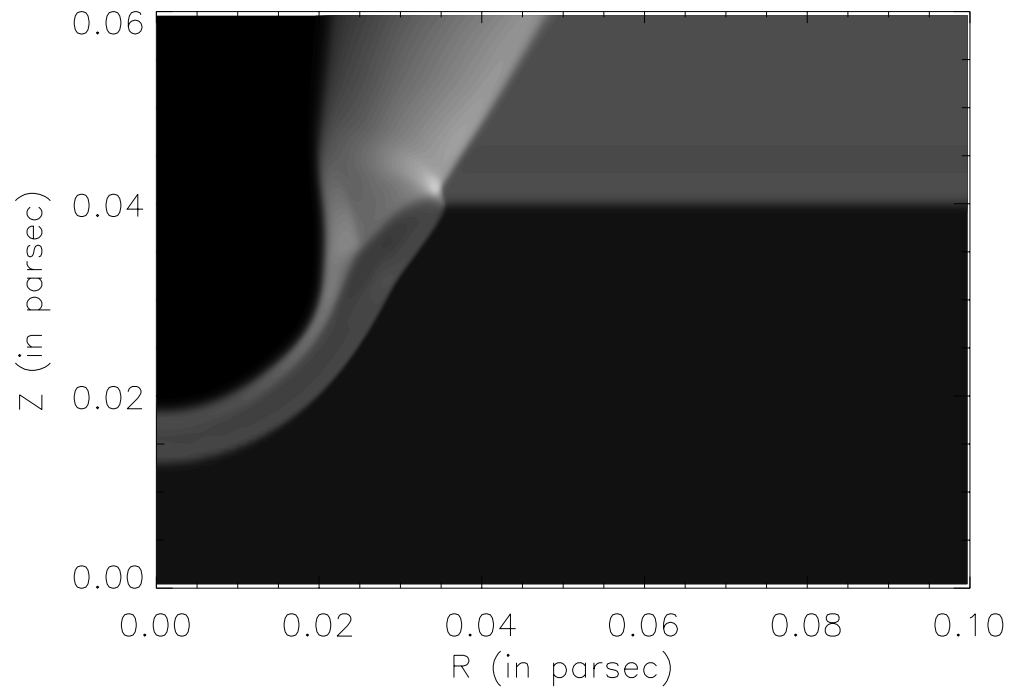


Figure 4.8: *Density profile of a PWN bow shock with the same parameters as denoted in table 1 at a low resolution. Here the PWN is interacting with the shell of the SNR. The gray-scale corresponds to the density.*

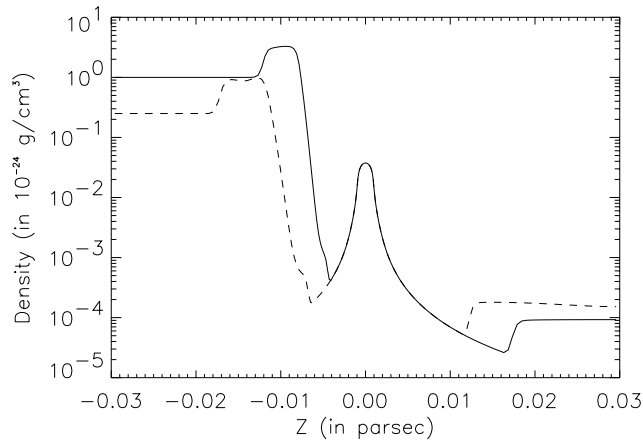


Figure 4.9: *Density profile of a PWN bow shock where a cut has been made along the z-axis. In this figure the pulsar's position corresponds to $Z = 0$. The solid line denotes the density profile before interacting with the SNR shock. The dashed line denotes the density profile after the SNR shock has passed the head of the bow shock. The PWN has expanded roughly by a factor 1.5.*

shell of the remnant it encounters the unshocked ISM. The ambient density is reduced by a factor 4.0, which results in a similar density reduction behind the bow shock.

4.4 Conclusions

We have considered the case of a pulsar wind breaking through of the shell of a SNR in the Sedov-Taylor stage. We have shown that only high-velocity pulsars reach the edge of the SNR while the SNR is still in the Sedov stage of its evolution. At moment of break-through, the ratio of the pulsar velocity and SNR expansion speed is fixed at $V_{\text{psr}}/V_{\text{snr}} = 5/2$, and the Mach number associated with the pulsar motion equals $\mathcal{M}_{\text{psr}} = 7/\sqrt{5}$. These conclusions are *independent* of the explosion energy E_{snr} or the pulsar speed V_{psr} .

Our simulations show that the break-through of the PWN does not lead to a significant disruption. The reduction of stagnation pressure by about 50% leads to a moderate expansion of the PWN where its radius increases by a factor ~ 1.5 . The latter result can also be obtained analytically.

There is good agreement between our numerical results and analytical estimates, based on pressure balance arguments, for the size of the bowshock surrounding the PWN. The only clear indication of the interaction between the PWN bow shock and the SNR (Sedov-Taylor) blast wave is a density- and pressure enhancement at the intersection of these two shocks.

In chapter 6 we will consider the effects of the energetic particles which are injected by the pulsar wind into the surroundings. There we will show that the rejuvenation mechanism as proposed by Shull et al. (1989) can not be maintained because of diffusion arguments.

Bibliography

- [1] Blandford, R.D., McKee, C.F. 1976, *Phys. Fluids* 19, 1130
- [2] Cioffi, D.F., McKee, C.F., Bertschinger, E. 1988, *ApJ*, 334, 252
- [3] Cordes, J.M., Romani, R.W., and Lundgren, S.C. 1993 *Nature*, 362, 133
- [4] Frail, D.A., and Kulkarni, S.R. 1991 *Nature*, 352, 785
- [5] Frail, D.A., Goss, W.M., Whiteoak, J.B.Z. 1994, *ApJ*, 437, 781
- [6] Gaensler, B.M , Frail, D.A. 2000, *Nature*, 406, 158
- [7] Gaensler et al, 2000 *MNRAS* 000, 000
- [8] Harrison, P.A., Lyne, A.G., Anderson, B. 1993, *MNRAS*, 261, 113
- [9] Kennel, C.F., Coroniti, F.V. 1984, *ApJ*, 283, 694
- [10] Lyne, A.G., Lorimer, D.R. 1994, *Nature*, 369, 127
- [11] Romani, R.W., Cordes, J.M., and Yadigaroglu, I.A. 1997 *ApJ*, 484, L137
- [12] Shull, J.M., Fesen, R.A. & Saken, J.M. 1989, *ApJ*, 346, 860
- [13] Strom, R.G., 1987 *ApJ*, 319, L103
- [14] Strom, R.G. and Stappers, B.W. 2000, *Bonn proceedings*, 509
- [15] Tóth, G., Odstrčil, D., 1996, *J. Comp. Phys.* 128, 82
- [16] van der Swaluw, E., Achterberg, A., and Gallant, Y.A. 2001, submitted to *A&A*, *astro-ph/0012440*

Chapter 5

Non-thermal X-Ray Emission from young Supernova Remnants

E. van der Swaluw, A. Achterberg and Y. A. Gallant

abstract

The Galactic (nucleonic) cosmic-ray spectrum up to the knee ($E \sim 10^{15}$ eV) is attributed to acceleration processes which take place near the external shocks around supernova remnants (SNRs). Theoretical predictions give a similar estimate for the maximum particle energy which can be reached at these shocks. Electrons with energies $E \sim 10^{14}$ eV radiate X-ray photons in the $\sim 10 - 100$ μG magnetic fields present in many young SNRs. These electrons near the knee give rise to a non-thermal X-ray component in the spectrum of young supernova remnants. Recent observations of SN1006 and G347.3-0.5 confirm this prediction.

We have combined hydrodynamical calculations of the evolution of a young remnant with an algorithm which simultaneously calculates the associated particle acceleration in the test-particle approximation. This allows for

We present synchrotron maps at different frequencies in the X-ray domain, and present spectra of the energy distribution of the electrons at different positions in the supernova remnant. We compare our results with earlier work on this subject by Reynolds (1998).

5.1 Introduction

In this Chapter we consider the acceleration of electrons at the blast wave surrounding a young supernova remnant. The theory of diffusive shock acceleration (DSA) predicts that nuclei and electrons are accelerated efficiently at this blast-wave (see Drury (1983) and Blandford & Eichler (1987) for a review of DSA).

Galactic cosmic rays are thought to be produced at SNRs by this acceleration process. Cosmic ray nuclei can be accelerated up to the energy of the knee ($E \sim 10^{15}$ eV) of the Galactic cosmic ray spectrum. At the knee, the slope s of the spectrum steepens from its low-energy value, $s \equiv -d \ln N(E)/d \ln E \approx 2.7$, to $s \approx 3.0$, possibly signalling a change in the production process responsible for particles above 10^{15} eV, or reacceleration distributed throughout the Galaxy.

General considerations (e.g. Achterberg, 2000) allow us to estimate the maximum attainable energy for shock-accelerated particles in a SNR as

$$E_{\max} \approx ZeB \left(\frac{V_s}{c} \right) R_{\text{snr}}, \quad (5.1)$$

with Ze the absolute value of the particle charge, B the magnetic field strength in the ISM, V_s the shock speed and R_{snr} the shock radius. This estimate applies to energetic nuclei, where radiation or ionization losses can be neglected. For typical parameters ($R_{\text{snr}} \sim 10$ pc, $B \sim 30$ μ G and $V_s \sim 1000$ km/s) one finds $E_{\max} \sim 1000$ TeV, intriguingly close to the energy of the knee.

Recent discoveries of nonthermal X-ray emission from SNRs seem to suggest that relativistic electrons are accelerated by SNR shocks to similar energies, $E \approx 10 - 100$ TeV. The X-ray spectrum of three SNRs is dominated by nonthermal emission: SN1006 (Koyama et al. 1995), G347.3-0.5 (Koyama et al. 1997, Slane et al. 1999) and G266.2-1.2 (Slane et al. 2001). Furthermore Cas A, Kepler, Tycho and RCW 86 (Allen, Gotthelf, & Petre 1999) also show a nonthermal X-ray component, but in these three systems there is a significant thermal component below 10 keV.

Diffusive shock acceleration naturally produces particles with a power-law distribution in momentum. The power-law index s is determined by the compression ratio r of the shock. In the test-particle limit this slope equals $s = (r + 2)/(r - 1)$, and spectral index of the associated synchrotron emission is $\alpha \equiv -d \ln S_\nu/d \ln \nu = (s - 1)/2$. At radio frequencies observations of SNR shells give $\alpha \sim 0.5 - 0.6$, corresponding with $s = 2\alpha + 1 \sim 2.0 - 2.2$. This is encouragingly close to the predicted value for s if the accelerator is a strong hydrodynamical shock with compression ratio $r = 4$. The fact that the observed

spectrum is somewhat steeper than predicted probably indicates that the shock is weakened by the back-reaction of the accelerated particles, which reduces the shock compression (see e.g. Drury et al. 1989, Kang & Jones 1991).

A problem with this simple scenario, which we will not address here, is the fact that no detectable gamma-ray emission is observed from most young remnants. Such emission is expected if nuclei are accelerated to TeV energies. They result from inelastic collisions between cosmic ray nuclei and nuclei in the ISM. These collisions produce (among other debris) neutral pions which decay into gamma rays.

The momentum distribution will deviate from a simple power law close to the maximum energy. Due to the combined effect of radiation losses and the finite age of the remnant the spectrum must steepen. Allen et al. (1999) show that the spectral index associated with five remnants (Cas A, Tycho, RCW 86, Kepler and SN 1006) must continue at the radio value ($\alpha \sim 0.6$, $s \sim 2.2$) up to X-ray frequencies (photon energy 10 keV), corresponding to electron energies of $E \sim 10$ TeV for an assumed field strength of $10 - 100 \mu\text{G}$. Above a photon energy of 10 keV the photon spectral index is much steeper, $\alpha \sim 3.2$.

These observations suggest that young SNRs indeed produce relativistic electrons with a simple power law distribution with slope $s \sim 2.2$, up to an energy of ~ 10 TeV, close to the energy (~ 1000 TeV) associated with the knee in the nucleonic component of the Galactic cosmic rays. This seems to confirm one of the basic predictions of the theory of DSA. Detailed models of the morphology and the spectrum of young SNRs seem to be the next step in order to get better tools to explain the observations.

Reynolds (1998) (R98) has presented a detailed calculation of the morphology and the spectrum of synchrotron X-rays from SNRs. In this chapter we present a method which expands on his work. We use a hydrodynamics code to calculate the evolution of a SNR in the general ISM. Simultaneously we calculate the particle acceleration at the shock, and particle transport within the remnant. Our algorithm employs the test particle approximation where the fluid dynamics of the SNR is not influenced by the accelerated particles.

This Chapter is organised as follows. In section 5.2 we briefly describe the theory of particle acceleration at SNRs, and calculate typical electron- and photon energies. In section 5.3 we describe the method used to simulate particle acceleration. In section 5.4 we present the simulation results, followed by a discussion and conclusions in section 5.5.

5.2 Particle acceleration at SNR blastwaves

5.2.1 SNR evolution

The evolution of a single supernova remnant (SNR) can be divided in four main stages (Woltjer 1972): the free expansion stage, the Sedov-Taylor stage, the pressure-driven snow plow stage and the momentum-conserving stage. These stages correspond to a progressive deceleration of SNR expansion. If the SNR expands into a uniform ISM with density n_0 , the shock radius R_{snr} varies with time in these four stages as $R_{\text{snr}} \propto t$, $R_{\text{snr}} \propto t^{2/5}$, $R_{\text{snr}} \propto t^{2/7}$ and $R_{\text{snr}} \propto t^{1/4}$ respectively. In this chapter we will only focus on the free expansion and Sedov-Taylor stages of SNR evolution. In later stages, synchrotron losses together with the reduced efficiency of the acceleration process prevent electrons to be accelerated to X-ray emitting energies.

To describe the transition between the free expansion stage and the Sedov-Taylor stage we use the results of McKee & Truelove (1995). The transition occurs roughly when the SNR blastwave has swept up a roughly 1.61 times the ejecta mass. For an interstellar mass density ρ_{ism} this occurs at a radius

$$R_{\text{ST}} = 1.17 \left(\frac{3M_{\text{ej}}}{4\pi\rho_{\text{ism}}} \right)^{1/3} \quad (5.2)$$

which is

$$R_{\text{ST}} = 2.23 \left(\frac{M_{\text{ej}}}{M_{\odot}} \right)^{1/3} n_0^{-1/3} \text{ pc}. \quad (5.3)$$

Here $n_0 = \rho_{\text{ism}}/\mu m$ is the number density (in cm^{-3}) of the ISM, assuming a mean atomic mass $\mu_{\text{m}} = 2.34 \times 10^{-24}$ g, and M_{ej} is the mass of the ejected stellar mantle. Given an mechanical explosion energy $E_0 = 10^{51} E_{51}$ erg, this transition occurs at an age

$$t \approx t_{\text{ST}} = 209 E_{51}^{-1/2} \left(\frac{M_{\text{ej}}}{M_{\odot}} \right)^{5/6} n_0^{-1/3} \text{ yr}. \quad (5.4)$$

Defining a typical velocity

$$V_{\text{ST}} = \frac{R_{\text{ST}}}{t_{\text{ST}}} = 10,400 E_{51}^{1/2} \left(\frac{M_{\text{ej}}}{M_{\odot}} \right)^{-1/2} \text{ km/s}, \quad (5.5)$$

the typical shock speed at transition is

$$V_s(t_{\text{ST}}) \approx 0.63 V_{\text{ST}} = 6,552 E_{51}^{1/2} \left(\frac{M_{\text{ej}}}{M_{\odot}} \right)^{-1/2} \text{ km/s}. \quad (5.6)$$

5.2.2 Shock acceleration

The acceleration process around shocks relies on efficient scattering of the relativistic particles. This scattering is caused by irregularities (Alfvén waves) in the magnetic fields near the shock. The scattering confines particles near the shock, allowing for repeated shock crossings and efficient acceleration.

The resulting spatial diffusion proceeds at a different rate along and across the magnetic field, and must be described by a diffusion tensor of the form

$$\mathbf{D}_x = D_{\parallel} \hat{\mathbf{b}}\hat{\mathbf{b}} + D_{\perp} (\mathbf{I} - \hat{\mathbf{b}}\hat{\mathbf{b}}), \quad (5.7)$$

where $\hat{\mathbf{b}} = \mathbf{B}/|\mathbf{B}|$ is the unit vector along the magnetic field and \mathbf{I} the unit tensor. The field-aligned and perpendicular diffusion coefficients scale roughly as

$$D_{\parallel} \sim \frac{1}{3} c \ell = \kappa_B \left(\frac{\ell}{r_g} \right), \quad D_{\perp} \sim \frac{D_{\parallel}}{1 + (\ell/r_g)^2}. \quad (5.8)$$

Here ℓ is the scattering mean free path, $r_g \sim E/ZeB$ the particle gyro radius for relativistic particles ($E \approx pc$) and

$$\kappa_B \equiv \frac{1}{3} c r_g = \frac{cE}{3ZeB} \quad (5.9)$$

is the Bohm diffusion coefficient. In this chapter we will assume Bohm diffusion, with $\ell \approx r_g$ and $D_{\parallel} \approx D_{\perp} \approx \kappa_B$. In this way we avoid having to deal with anisotropic diffusion, which is computationally expensive. Bohm diffusion is thought to be a reasonable approximation if the level of magnetic turbulence has an amplitude comparable to the mean field: $\delta B \sim B$.

In diffusive shock acceleration, the diffusion rate determines the acceleration time scale. The acceleration time near a planar shock equals (e.g. Drury 1983)

$$t_{\text{acc}} \equiv \left(\frac{1}{E} \frac{dE}{dt} \right)^{-1} = \frac{3}{V_1 V_2} \left(\frac{D_{n1} V_2 + D_{n2} V_1}{V_1 - V_2} \right). \quad (5.10)$$

Here V is the velocity of the fluid in the shock rest frame, and D_n denotes the diffusion coefficient in the direction perpendicular to the plane of the shock:

$$D_n \equiv \hat{\mathbf{n}} \cdot \mathbf{D}_x \cdot \hat{\mathbf{n}} = D_{\parallel} \cos^2 \theta_{Bn} + D_{\perp} \sin^2 \theta_{Bn} . \quad (5.11)$$

Here $\hat{\mathbf{n}}$ is the shock normal and θ_{Bn} the angle between the shock normal and the magnetic field. The subscripts 1 (2) refer to the values of various quantities upstream (downstream) of the shock. We estimate the acceleration time scale, assuming Bohm diffusion on both sides of a strong hydrodynamical shock with compression ratio $r = 4$, propagating into a stationary ISM so that $V_1 = V_s$ and $V_2 = V_s/4$. Writing B for the *upstream* magnetic field and κ_B for the associated Bohm diffusion coefficient, one finds

$$t_{\text{acc}}(E) = \xi \frac{\kappa_B}{V_s^2} = \frac{\xi}{3} \frac{cE}{ZeB V_s^2} . \quad (5.12)$$

The parameter ξ takes the value $\xi = 20$ for a parallel shock where the magnetic field is along the shock normal so that $B_2 = B$, and $\xi = 8$ for a perpendicular shock where the field is in the plane of the shock and $B_2 = 4B$. This corresponds to an acceleration *rate* for electrons or protons ($Z = 1$)

$$\left(\frac{dE}{dt} \right)_{\text{dsa}} = \frac{3}{\xi} \frac{eB V_s^2}{c} . \quad (5.13)$$

The synchrotron loss rate for electrons is (e.g. Rybicki & Lightman 1979)

$$\left(\frac{dE}{dt} \right)_{\text{sy}} = - \frac{\sigma_T B^2 E^2}{6\pi m_e^2 c^3} , \quad (5.14)$$

where $\sigma_T = 6.65 \times 10^{-25} \text{ cm}^2$ is the Thomson cross section. Since we are only interested in an order of magnitude calculation, we neglect the difference between the synchrotron losses incurred upstream and downstream from the shock. This gives an approximate equation for the net electron acceleration rate at the shock, assuming Bohm diffusion:

$$\frac{dE}{dt} = \frac{3}{\xi} \frac{eB V_s^2}{c} - \frac{\sigma_T B^2 E^2}{6\pi m_e^2 c^3} . \quad (5.15)$$

Protons (and other nuclei) satisfy a similar equation without the synchrotron loss term. Equation (5.15) describes the energy gain of particles that remain close to the shock, subject to shock acceleration. One can use it to calculate the typical cut-off energy in the distribution of shock-accelerated particles.

5.2.3 Typical electron and photon energies

If losses can be neglected, as is the case for nuclei, Eqn. (5.15) defines a typical energy

$$E_{\max} \sim \frac{3eB}{\xi} \left(\frac{V_{\text{ST}}}{c} \right) R_{\text{ST}}, \quad (5.16)$$

which is

$$E_{\max} \approx 200 E_{51} \left(\frac{\xi}{10} \right)^{-1} \left(\frac{M_{\text{ej}}}{1 M_{\odot}} \right)^{-1/6} \left(\frac{B}{10 \mu\text{G}} \right) n_0^{-1/3} \text{ TeV}. \quad (5.17)$$

Particles injected into the acceleration process at a time $t \ll t_{\text{ST}}$ will, in absence of losses, reach an energy $E \approx E_{\max}$ at $t \sim t_{\text{ST}}$. In the Sedov-Taylor phase the acceleration rate decays as $(dE/dt)_{\text{dsa}} \propto V_s^2 \propto R_{\text{snr}}^{-3}$. Assuming $B = \text{constant}$, loss-free acceleration for $t > t_{\text{ST}}$ typically trebles the particle energy to $E \approx 3E_{\max}$.

For electrons, the energy gain at the shock balances synchrotron losses when

$$E = E_{\text{sy}} \equiv \sqrt{\frac{27}{4\xi}} \frac{m_e c^2}{\sqrt{\alpha}} \left(\frac{B}{B_{\text{cr}}} \right)^{-1/2} \left(\frac{V_s}{c} \right). \quad (5.18)$$

In this expression $\alpha \equiv e^2/\hbar c = 1/137.04$ is the fine-structure constant, and $B_{\text{cr}} \equiv m_e^2 c^3/e\hbar = 4.4 \times 10^{13} \text{ G}$ is the critical magnetic field. For typical parameters one finds

$$E_{\text{sy}} \approx 350 E_{51}^{1/2} \left(\frac{\xi}{10} \right)^{-1/2} \left(\frac{V_s}{V_{\text{ST}}} \right) \left(\frac{M_{\text{ej}}}{M_{\odot}} \right)^{-1/2} \left(\frac{B}{10 \mu\text{G}} \right)^{-1/2} \text{ TeV}. \quad (5.19)$$

In the free expansion stage one has $V_s \approx 1.37 V_{\text{ST}}$, while well into the Sedov-Taylor phase ($t \gg t_{\text{ST}}$) one has

$$\frac{V_s}{V_{\text{ST}}} \approx 0.63 \left(\frac{R_{\text{snr}}}{R_{\text{ST}}} \right)^{-3/2}. \quad (5.20)$$

Asymptotically, electrons will approach an energy E_{sy} when the age of the remnant becomes larger than the synchrotron loss time,

$$t_{\text{sy}} \approx 800 \left(\frac{B}{10 \mu\text{G}} \right)^{-2} \left(\frac{E}{100 \text{ TeV}} \right)^{-1} \text{ yr}. \quad (5.21)$$

The scaling $E_{\text{sy}} \propto B^{-1/2}$ implies that the maximum energy of synchrotron photons no longer depends on the magnetic field strength in the source once electron acceleration is limited by synchrotron losses. Using the standard expression for the typical synchrotron frequency ν_s ,

$$\nu_s \sim \frac{3eB}{4\pi m_e c} \left(\frac{E}{m_e c^2} \right)^2 \quad (5.22)$$

with $E = E_{\text{sy}}$, one finds:

$$h\nu_{\text{max}} \sim \left(\frac{81}{4\pi\xi\alpha} \right) m_e V_s^2 \quad (5.23)$$

which is

$$h\nu_{\text{max}} \approx 54 E_{51} \left(\frac{\xi}{10} \right)^{-1} \left(\frac{M_{\text{ej}}}{M_\odot} \right)^{-1} \left(\frac{V_s}{V_{\text{ST}}} \right)^2 \text{ keV} . \quad (5.24)$$

Up to factors of order unity, one has (McKee & Truelove 1995)

$$V_{\text{ST}}^2 = 2E_0/M_{\text{ej}} , \quad (5.25)$$

so that the typical cut-off energy in the spectrum of synchrotron photons is

$$h\nu_{\text{max}} \approx 10^2 \left(\frac{m_e}{M_{\text{ej}}} \right) \left(\frac{V_s}{V_{\text{ST}}} \right)^2 E_0 . \quad (5.26)$$

These estimates show that one has to observe SNRs in the free expansion phase (where $V_s \approx V_{\text{ST}} \approx 10,000$ km/s), or closely thereafter, if the shock is to accelerate electrons to a sufficiently high energy to produce synchrotron X-rays in the keV range.

Figure 5.1 shows the typical energy of electrons and protons, injected at an early stage of the SNR evolution, as a function of time. The particle energy is calculated by numerically integrating Eqn. (5.15) with $\xi = 20$ (parallel shock), using the semi-analytical results of McKee & Truelove (1995) for the velocity of the external blast wave as a function of time:

$$\frac{V_s(t)}{V_{ST}} = \begin{cases} 1.37 \left[1 + 0.6 \left(\frac{t}{t_{ST}} \right)^{3/2} \right]^{-5/3} & \text{if } t < t_{ST}, \\ 0.63 \left[1.56 \left(\frac{t}{t_{ST}} \right) - 0.56 \right]^{-3/5} & \text{if } t \geq t_{ST}, \end{cases} \quad (5.27)$$

The parameters for the SNR are the same as used in the simulations presented below: an explosion energy $E_0 = 10^{51}$ erg, ejecta mass $M_{ej} = 3M_\odot$ and an ISM mass density $\rho_0 = 10^{-24}$ g/cm³. This corresponds to $t_{ST} \approx 700$ yr, $V_{ST} \approx 6000$ km/s and $R_{ST} \approx 4.5$ pc. We consider three values for the strength of the ISM magnetic field: $B_0 = 3, 10$ and $30 \mu\text{G}$.

In the free expansion stage ($t \ll t_{ST}$ and $R_{snr} \ll R_{ST}$) the energy of the accelerated particles is limited by the finite age of the source. The maximum particle energy grows as $E \propto BR_{snr}$. Proton acceleration continues to be limited only by the size and age of the remnant, and protons are accelerated to an energy $E \approx 20 B_{\mu\text{G}}$ TeV by the time the SNR has expanded to a radius of 30 pc.

Electrons feel the effect of synchrotron losses. The influence of these losses sets in at earlier times (and smaller SNR radii) with increasing field strength. This limits the electron energy to $E \leq 40$ TeV for $B_0 = 3 \mu\text{G}$, $E \leq 90$ TeV for $B_0 = 10 \mu\text{G}$ and $E \leq 100$ TeV for $B_0 = 30 \mu\text{G}$. At late times (large radii) the energy of old electrons near the shock decays to $E = E_{sy}$. This means that the maximum energy in the distribution of shock-accelerated electrons will correspond to the energy where shock acceleration is balanced by synchrotron losses.

Figure 5.1 also shows the typical photon energy $h\nu_s$ of the synchrotron photons emitted by these maximum-energy electrons. It gives the typical cut-off energy in the photon spectrum. If the magnetic field is small, electrons hit the synchrotron-limited energy relatively late in the evolution of the remnant ($t \gg t_{ST}$), when the associated maximum photon energy is already decaying: $h\nu_{\text{max}} \propto V_s^2 \propto R_{snr}^{-3}$. Such remnants are not expected to be strong sources of non-thermal X-ray emission.

If the magnetic field is large, shock acceleration is rapid, and the electrons hit the synchrotron-limited energy early in the evolution of the remnant. In that case, the remnant is still in the free expansion stage with $V_s \approx V_{ST}$.

Taking $\xi \approx 15$ as an average value, such remnants should show non-thermal X-ray emission around $t \approx t_{\text{ST}}$, up to typical photon energies of the order of 10-100 keV.

One can estimate a minimum value of the magnetic field above which one expects young SNRs to be non-thermal X-ray emitters. It corresponds to the case where the electrons begin to be limited by synchrotron losses at the end of the free-expansion stage, so that $E_{\text{max}} \approx E_{\text{sy}}$ for $R_{\text{snr}} \approx R_{\text{ST}}$. It turns out that this minimum field only depends on the SNR parameters through the Sedov-Taylor radius R_{ST} . It can be expressed as:

$$\frac{B_{\text{min}}}{B_{\text{cr}}} = \left(\frac{3\xi}{4\alpha} \right)^{1/3} \left(\frac{\lambda_e}{R_{\text{ST}}} \right)^{2/3}, \quad (5.28)$$

where $\lambda_e = \hbar/m_e c = 3.86 \times 10^{-11}$ cm is the Compton wavelength of the electron. For typical SNR parameters one finds

$$B_{\text{min}} \approx 14 \left(\frac{\xi}{10} \right)^{1/3} \left(\frac{M_{\text{ej}}}{M_{\odot}} \right)^{-2/9} n_0^{2/9} \mu\text{G}. \quad (5.29)$$

The value of B_{min} depends relatively weakly on SNR parameters.

5.3 Simulation method

5.3.1 SNR Hydrodynamics

We have performed hydrodynamical simulations, using the Versatile Advection Code ¹ (VAC, Tóth 1996). We employ the TVD-MUSCL scheme with a Roe-type approximate Riemann solver, one of the numerical algorithms available in VAC (Tóth and Odstrčil 1996). A discussion of this (and other) schemes for numerical hydrodynamics can be found in LeVeque (1998).

The calculations are performed in one dimension, on a spherically symmetric grid with uniform radial grid spacing. As an initial condition we deposit an amount E_0 in thermal energy and a mass M_{ej} in the first few grid cells. This leads to the formation of both the reverse shock propagating into the stellar ejecta, and the forward shock in the ISM, as discussed above. The resolution of our calculations are such that both the forward shock and the reverse shock are

¹See <http://www.phys.uu.nl/~toth/>

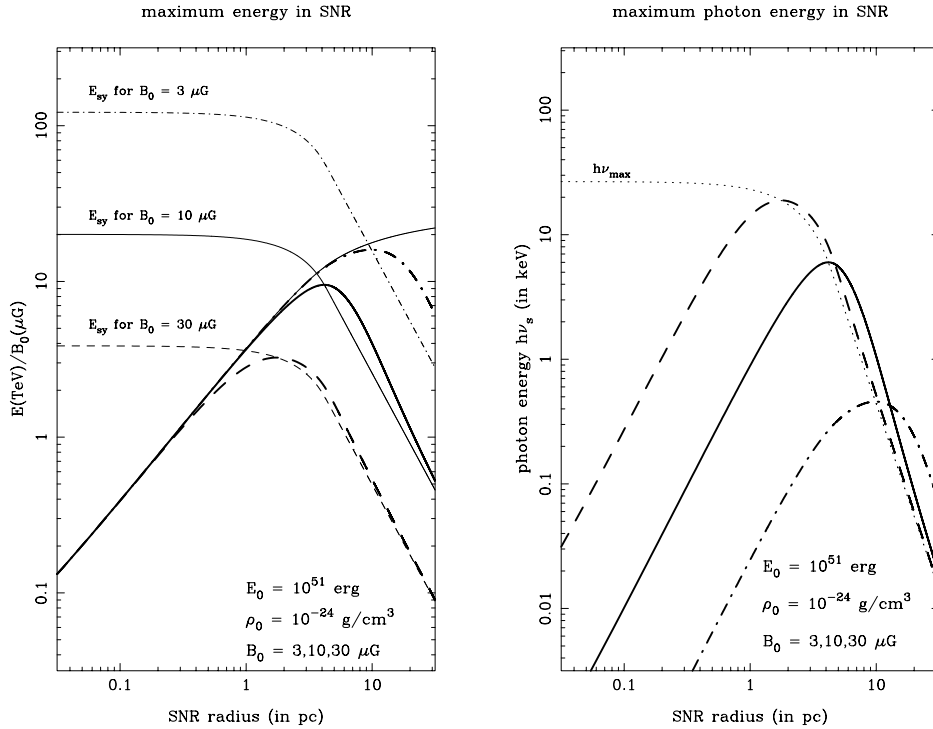


Figure 5.1: The left panel shows the typical maximum energy of shock-accelerated electrons and protons, plotted as E/B , as a function of the radius R_{SNR} of the supernova remnant. Shown are three cases, corresponding to a magnetic field strength of $B = 3 \mu\text{G}$ (dash-dot curves), $B = 10 \mu\text{G}$ (solid curves) and $B = 30 \mu\text{G}$ (dashed curves). Also shown is the energy E_{sy} where electron synchrotron losses balance the energy gain per unit time at the shock. At early times, the maximum particle energy rises as $E/B \propto V_{\text{SNR}} R_{\text{SNR}}$. Electrons start to lose energy when $E > E_{\text{sy}}$, asymptotically approaching the relation $E \approx E_{\text{sy}} \propto R_{\text{SNR}}^{-3/2}$ at late times. Protons, who are not subject to losses, continue to follow the loss-free energy curve (thin solid curve). The right panel shows the typical maximum energy of synchrotron photons emitted by shock-accelerated electrons in these three cases. Also shown is the energy $h\nu_{\text{max}}$ corresponding to an electron energy $E = E_{\text{sy}}$ (dotted curve). This quantity is independent of the magnetic field strength. In older remnants, the cut-off in the synchrotron spectrum should be close to a photon energy $h\nu_{\text{max}}$.

resolved, and these shocks have the correct compression factor ($r = 4$) expected for a strong, non-relativistic hydrodynamical shock.

5.3.2 Magnetic fields

Our hydrodynamical simulations do not include the dynamical influence of magnetic fields. The magnetic pressure ($B^2/8\pi$) is generally much lower than the thermal pressure inside a young SNR. Therefore, the presence of magnetic fields does not significantly influence SNR expansion. However, in order to describe particle acceleration and the associated synchrotron emission, we need to know the value for the magnetic field throughout the SNR. The magnetic field determines the value of the particle diffusion coefficient, and of the synchrotron emissivity.

We choose to describe the magnetic field in the approximation where it is passively carried by the flow, but neglect the magnetic forces acting on the flow. The magnetic field configuration inside the SNR can then be found using the frozen-in condition (flux conservation). This condition allows us to calculate the magnetic field $\mathbf{B}(\mathbf{r}, t)$, given the field $\mathbf{B}_0(\mathbf{r}_0, t_0)$ and local density ρ_0 at some initial time t_0 when the fluid attached to the field line was at position $\mathbf{r}(t_0) \equiv \mathbf{r}_0 = (x_0^1, x_0^2, x_0^3)$ (e.g. Zeldovich, Ruzmaikin & Sokoloff 1983). The field components B_i follow quite generally from

$$\frac{B_i}{\rho h_i} = \sum_{j=1}^3 \frac{\partial x^i}{\partial x_0^j} \left(\frac{B_{0j}}{\rho_0 h_{0j}} \right). \quad (5.30)$$

Here $\rho \equiv \rho(r, t)$ is the density and $\rho_0 \equiv \rho(r_0, t_0)$ etc. The coefficients h_i are the scale factors appearing in the distance recipe for orthogonal curvilinear coordinates x^i ($i = 1, 2, 3$), $ds^2 = \sum_{i=1}^3 (h_i dx^i)^2$. In spherical coordinates, with distance recipe

$$ds^2 = dr^2 + r^2 d\theta^2 + r^2 \sin^2 \theta d\phi^2, \quad (5.31)$$

one has $h_{rr} = 1$, $h_{\theta\theta} = r^2$ and $h_{\phi\phi} = r^2 \sin^2 \theta$. The assumption of radial expansion, together with mass conservation

$$4\pi r^2 \rho dr = 4\pi r_0^2 \rho_0 dr_0, \quad (5.32)$$

implies:

$$\frac{\partial \theta}{\partial r_0} = \frac{\partial r}{\partial \theta_0} = 0 \quad , \quad \frac{\partial \theta}{\partial \theta_0} = 1 \quad , \quad \frac{\partial r}{\partial r_0} = \frac{\rho_0 r_0^2}{\rho r^2} . \quad (5.33)$$

Assuming $B_\phi = 0$, one finds the radial and tangential field components B_r and B_θ :

$$B_r = \left(\frac{r_0}{r} \right)^2 B_{0r} , \quad (5.34)$$

$$B_\theta = \left(\frac{\rho}{\rho_0} \right) \left(\frac{r}{r_0} \right) B_{0\theta} .$$

Here r is the current radial position of the fluid element, and r_0 its position when it crosses the SNR blastwave. Similarly, ρ is the density at the current position of the fluid element and ρ_0 is the density of the ISM. We assume that the only magnetic field present in the SNR is the compressed interstellar field. The interstellar field is taken to be uniform with field strength B_0 and aligned with the z -axis:

$$B_{0r} = B_0 \sin \theta_0 \quad , \quad B_{0\theta} = -B_0 \cos \theta_0 . \quad (5.35)$$

The density profile $\rho(r)$ and the value of r/r_0 throughout the remnant follow from the simulations. In this manner we obtain a remnant with a spherically symmetric flow, and an axially symmetric magnetic field configuration, which both dependent on time. This approach is similar to the one used Duin & Strom (1975) and by Reynolds & Chevalier (1981).

The difference between our approach and the approach taken in R98 is in the treatment of the dynamical evolution of the SNR. Whereas R98 assumes a Sedov solution, our numerical results cover the free expansion stage, the Sedov-Taylor stage, and the transition between the two. As argued above, the most energetic particles are produced near this transition.

5.3.3 Energetic particles

The acceleration and propagation of relativistic particles in a magnetized astrophysical plasmas is usually investigated by solving a Fokker-Planck equation of the type:

$$\frac{\partial F(\mathbf{Z}, t)}{\partial t} = \frac{\partial}{\partial \mathbf{Z}} \cdot \left(-\dot{\mathbf{Z}} F(\mathbf{Z}, t) + \frac{\partial}{\partial \mathbf{Z}} \cdot [\mathbf{D} F(\mathbf{Z}, t)] \right), \quad (5.36)$$

e.g. Skilling, (1975) and Jones(1990). Here $F(\mathbf{Z}, t)$ is the particle distribution function in phase space, $\mathbf{Z} = (\mathbf{x}, \mathbf{p})$ is the phase-space position vector, $\dot{\mathbf{Z}}$ is the phase-space advection velocity and \mathbf{D} is a diffusion tensor, formally defined in dyadic notation as

$$\mathbf{D} \equiv \frac{\langle \Delta \mathbf{Z} \Delta \mathbf{Z} \rangle}{2\Delta t}. \quad (5.37)$$

It has been shown (e.g. Gardiner, 1983; Saslaw, 1985) that the Fokker-Planck equation is equivalent to the following stochastic differential equation (SDE) of the Itô form, consisting of a regular advective term $\propto dt$ and a stochastic term:

$$d\mathbf{Z} = \dot{\mathbf{Z}} dt + \sqrt{2\mathbf{D}} \cdot d\mathbf{W}. \quad (5.38)$$

Here $\sqrt{\mathbf{D}}$ is short-hand notation for a tensor with components such that

$$\sqrt{\mathbf{D}} \cdot \sqrt{\mathbf{D}} = \mathbf{D}.$$

The velocity $\dot{\mathbf{Z}}$ entering the advective term consists of both the mean velocity in phase space, and an additional dynamical friction term:

$$\dot{\mathbf{Z}} \equiv \frac{d\mathbf{Z}}{dt} + \frac{\partial}{\partial \mathbf{Z}} \cdot (\mathbf{D}^\dagger), \quad (5.39)$$

where \mathbf{D}^\dagger is the transpose of \mathbf{D} .

The noise term $d\mathbf{W}$ in the stochastic term of equation (5.38) is a N -dimensional Wiener process, where N is the number of degrees of freedom in phase space (e.g MacKinnon & Craig 1991; Achterberg & Krülls 1992 and Krülls & Achterberg 1994). Its components dW_i satisfy a set of simple rules,

$$\langle dW_i \rangle = 0, \quad \langle dW_i dW_j \rangle = \begin{cases} dt & \text{if } i = j \\ 0 & \text{if } i \neq j \end{cases}, \quad (5.40)$$

where the angular brackets indicate an average over many statistically independent realizations of this Wiener process.

By running many independent realizations of prescription (5.38) one can construct the phase-space distribution $F(\mathbf{Z}, t)$.

This correspondence between the Fokker Planck equation and SDEs is the basis for a fast simulation method for particle acceleration and propagation in a time-dependent flow. With this method one can include effects like synchrotron losses, Compton losses and expansion losses in a straightforward fashion.

The application to shock acceleration has been considered by different authors (e.g Krülls and Achterberg 1994; Marcowith and Kirk 1999) and has been compared successfully with available analytical solutions. We employ this method here in conjunction with the hydrodynamical simulations to calculate the behaviour of relativistic electrons a young supernova remnant.

For practical reasons, we assume isotropic spatial diffusion with a diffusion coefficient equal to the Bohm diffusion coefficient, $\mathbf{D} = \kappa_B \mathbf{I}$. Spatial transport is then described in cylindrical coordinates $Z = r \cos \theta$ and $R = r \sin \theta$ by the following two equations:

$$\begin{aligned} dZ &= \left(V \cos \theta + \frac{\partial \kappa_B}{\partial Z} \right) dt + \sqrt{2 \kappa_B} dW_Z ; \\ dR &= \left(V \sin \theta + \frac{\partial \kappa_B}{\partial R} \right) dt + \sqrt{2 \kappa_B} dW_R . \end{aligned} \quad (5.41)$$

Here V is the radial fluid velocity at the position of the particle. We neglect the possible influence of Fermi-II acceleration by waves, so the particle momentum p does not diffuse. In that case the energy change for relativistic electrons with $E \approx pc$ is described by (e.g. Krülls and Achterberg 1994):

$$dE = -\frac{E}{3} \left[\frac{1}{r^2} \frac{\partial}{\partial r} (r^2 V) \right] dt + \left(\frac{dE}{dt} \right)_{\text{sy}} dt . \quad (5.42)$$

The first term, involving the divergence of the radial fluid velocity, describes expansion losses within the remnant, as well as shock acceleration at the forward and reverse shocks, provided the time step dt is chosen such that

$$V dt \ll \Delta r_s \ll \sqrt{2 \kappa_B dt} . \quad (5.43)$$

The quantity Δr_s is the thickness of the shock transition, typically a few grid cells. In the simulations, the shocks are thin regions of strong (negative) divergence. The second term in (5.42) is the synchrotron loss term (5.14), evaluated using the local value of the magnetic field. Even though Eqn. (5.42) has no *explicit* stochastic term, the energy gain exhibits stochastic behaviour because different realizations of an electron trajectory through the remnant, as obtained from (5.41), lead to a different sampling of the fluid velocity $V(r, t)$ and its derivatives.

By simultaneously advancing the particle position (R, Z) in the remnant and the particle energy E using (5.41) and (5.42), using the velocity $V(r, t)$ obtained from the numerical simulations, one can model the behaviour of energetic electrons in the SNR.

5.4 Simulation results

We have simulated the evolution of a spherical supernova remnant with the parameters listed in Table 1 using the VAC code. Figure 5.2 shows the radius R_{SNR} of the remnant. One can see the transition from the free expansion phase to the Sedov-Taylor stage at $t \approx 2$ kyr, where the exponent of the expansion law $R_{\text{SNR}} \propto t^\beta$ changes from $\beta = 1$ to $\beta = 2/5$.

Figure 5.3 shows the radial velocity profile $V(r)$ of the remnant at a moment close to the transition to the Sedov-Taylor phase. One can clearly identify the reverse shock propagating into the ejecta ($r \simeq 3.6$ parsec), and the forward shock ($r \simeq 4.5$ parsec) propagating into the interstellar medium.

The results from the hydrodynamical simulations are used to calculate the acceleration and propagation of relativistic electrons near the forward shock in the test-particle approximation, using the Itô method described above. We assume isotropic diffusion at the Bohm rate set by the magnetic field constructed using the flux-freezing condition.

We continuously inject particles at the forward shock, starting at the age of $t = 200$ years, up to the end of the simulation at an age of $t = 1000$ years. At the end of the simulation the radius of the SNR equals $R_{\text{SNR}} \simeq 4.5$ parsec. The total grid over which the test-particles are allowed to propagate has a size $0.0 \leq R \leq 6.0$ parsec in cylindrical radius, and $-6.0 \leq Z \leq +6.0$ parsec along the symmetry axis (Z-axis). A total of $\sim 4.2 \times 10^6$ test particles are injected during the simulation. The injection is at constant injection momentum p_0 , with an injection rate proportional to the amount of swept-up interstellar material. The number of particles introduced at the shock in a time interval dt scales as

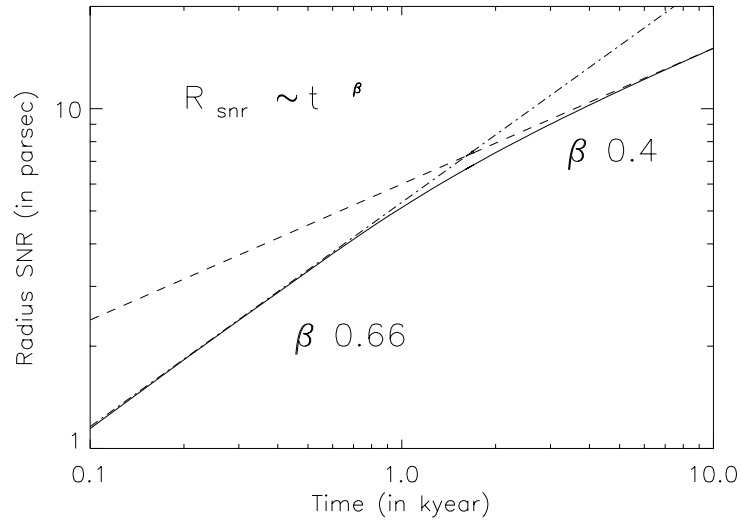


Figure 5.2: Expansion of a SNR, $R_{\text{snr}} \propto t^\beta$. There is a transition from the free expansion stage ($\beta = 1.0$, dashed line) to the Sedov-Taylor stage ($\beta = 0.2/5$, dotted line) at $t \sim 2$ kyr. The parameters of the SNR are tabulated in table 1.

Table 5.1: Parameters of simulated supernova remnant

| | |
|--|----------------------|
| Mechanical energy E_0 (in ergs) | 10^{51} |
| Ejecta mass M_{ej} (in M_\odot) | 6 |
| ISM mass density ρ_0 (in g/cm^3) | 10^{-24} |
| ISM magnetic field B_0 (in μG) | 10 |
| Number of radial grid cells | 5000 |
| Grid size Δr (in pc) | 1.0×10^{-3} |

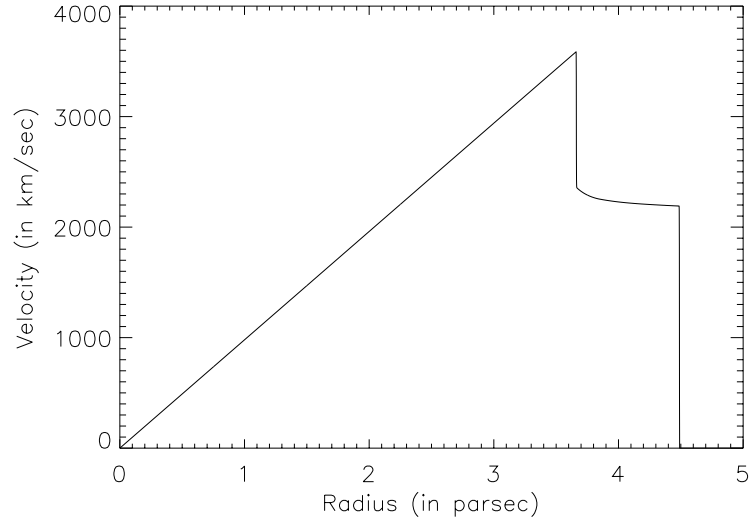


Figure 5.3: *Velocity profile of a SNR with the parameters as in table 1.*

$$d\mathcal{N}(p) \propto R_{\text{snr}}^2 V_s dt \times \delta(p - p_0) . \quad (5.44)$$

This implies that most particles were injected at later times, with $d\mathcal{N} \propto t^2 dt$ in the free expansion phase, and $d\mathcal{N} \propto t^{1/5} dt$ in the Sedov-Taylor stage.

At the end of the simulation we have the position and the momentum of each simulated particle. Because we also know the magnetic field strength throughout the remnant we can produce synchrotron surface brightness maps at different frequencies. The emissivity of each particle is modelled using a tabulated form of the well-known synchrotron emission profile $F(\nu/\nu_s)$ (e.g. Rybicky & Lightman 1979)

$$P(\nu) = \frac{\sqrt{3}e^3 B \sin \alpha}{m_e c^2} F\left(\frac{\nu}{\nu_s}\right), \quad (5.45)$$

where the typical frequency ν_s has been defined in Eqn. (5.22). To produce a surface brightness map we exploit the cylindrical symmetry of the system. A test-particle is copied N times on a circle around the axis of symmetry. In this way, each simulated electron contributes N times to the synchrotron map, each time at a different position separated by an angle $2\pi/N$ from the previous copy. Each

copy has a different angle α between the line of sight and the magnetic field orientation, which determines the typical emissivity and frequency distribution of the synchrotron radiation (see equations (5.22) and (5.45)). By adding the contribution of all copy particles one produces a surface brightness map.

An examples of a synchrotron map is shown in figures 5.4. It shows a similar surface brightness profile as the synchrotron maps presented by R98.

Figure 5.5 shows the energy distribution of the total amount of test-particles in the SNR. One can see that the cut-off occurs at the expected energy of $E \simeq 100$ Tev.

One can also calculate a photon spectrum of the synchrotron radiation from all the simulated electrons in the remnant. The same trick of using copy-particles is employed to calculate total spectrum. Figure 5.6 shows the resulting synchrotron spectrum.

At low photon energies, the spectral index α equals $\alpha \simeq -1.0$, whereas at the roll-off part of the spectrum, where the synchrotron losses start to match the energy gain due to the acceleration process we get a spectral index of $S_\nu \propto \nu^{-3.0}$ corresponding with a spectral index for the momentum distribution of $s = 7.0$. This is encouraging close to the value as *observed* for the five remnants by Allen et al. (1999).

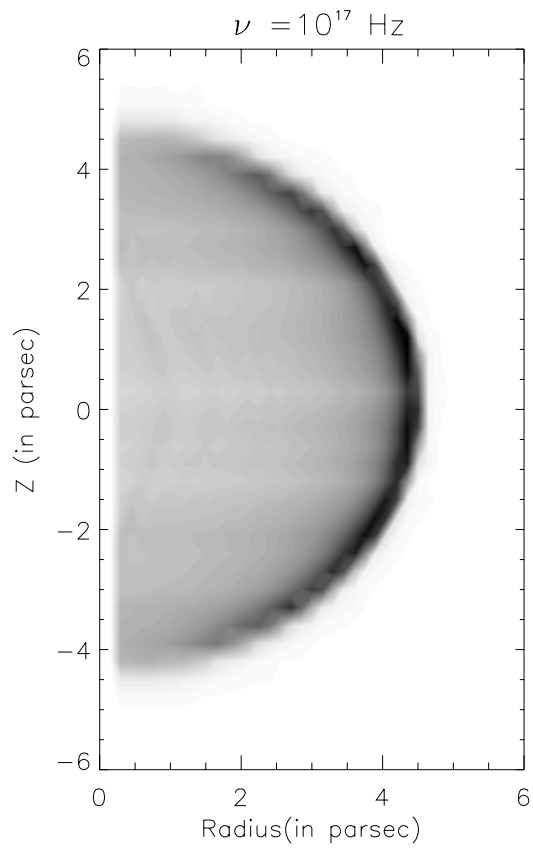


Figure 5.4: *synchrotron map at a frequency of $\nu = 10^{17}$ Hz.*

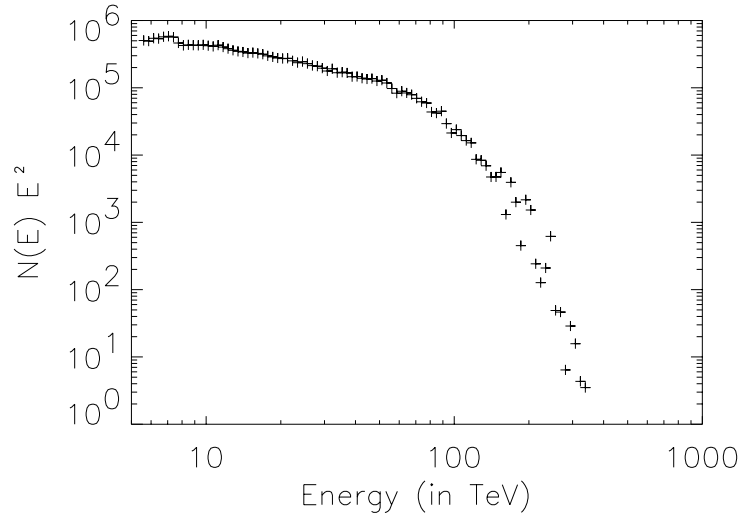


Figure 5.5: *Energy distribution of the total amount of test-particles in the SNR.*

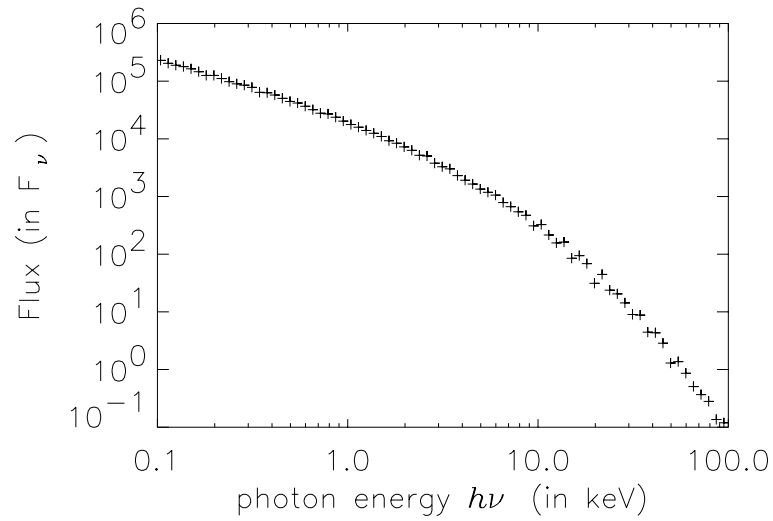


Figure 5.6: *Total integrated spectrum of the SNR.*

5.5 Discussion and conclusions

We have considered the acceleration of electrons in a young SNR by combining a simple hydrodynamics calculation with an algorithm to describe electron acceleration in the test-particle limit. These calculations, as well as theoretical estimates based on a simple model of shock acceleration, confirm that young remnants can accelerate electrons up to energies of 10-100 TeV, provided the magnetic field is sufficiently strong, typically $B \geq 10 \mu\text{G}$. We predict that these remnants are sources of synchrotron X-rays around the transition time between the free expansion phase and the Sedov-Taylor phase.

We have produced synchrotron surface brightness maps at different photon energies, which are qualitatively comparable with the synchrotron maps which were produced by R98 assuming a Sedov-Taylor remnant.

Our method can be applied to more complicated problems, such as SNRs expanding into a non-uniform ISM, which will lead to a more complicated morphology. Also, some of the simplifying assumptions made in these calculations should be replaced by more realistic ones. First of all, particle diffusion in the remnant should be treated more generally, allowing for the anisotropy induced by the magnetic field by relaxing the assumption that the mean free path equals the gyration radius ($\ell \sim r_g$). Although anisotropic diffusion is easily incorporated into our formalism, it is computationally expensive. We expect that, at least in the limit $\ell \gg r_g$, this will introduce a larger difference between the particle acceleration at the quasi-parallel region of the blastwave (where $\theta_{Bn} < 45^\circ$) and the quasi-perpendicular region (where $\theta_{Bn} > 45^\circ$).

Secondly, one could allow for distributed acceleration by waves (Fermi-II acceleration) in the remnant by assuming some wave spectrum, and including the associated momentum diffusion into the equation governing the energy change of our test particles.

Finally, one would like to relax the assumptions of spherical symmetry and a uniform interstellar medium, using a full MHD treatment to calculate both the magnetic field in the SNR, and the small-scale structure caused by instabilities (such as the Rayleigh-Taylor instability) expected in an expanding SNR.

Bibliography

- [1] Achterberg, A. 2000, in: Highly Energetic Physical Processes and Mechanisms for Emission from Astrophysical Plasmas (IAU Symp. no. 195), P.C.H. Martens, S. Tsuruta & M.A. Weber (Eds.), Astronomical Society of the Pacific, p. 291.
- [2] Achterberg, A., & Krüßs, W.M. 1992, A&A, 265, L13
- [3] Allen, G.E., Gotthelf, E.V., Petre, R. 1999, "Evidence of 10-100 Tev Electrons in Supernova Remnants," in Proceedings of the 26th International Cosmic Ray Conference, Salt Lake City, 17-25 August 1999, Edited by D.Kieda, M.Salamon, and B.Dingus, Vol.3, 480-483
- [4] Blandford, R.D., & Eichler, D. 1987 Phys.Rep., 154, 1
- [5] Drury, L.O.C. 1983 Rep.Prog.Phys., 46, 973
- [6] Drury, L.O.C., Markiewicz, W.J., Völk, H.J. 1989, A&A, 225, 179
- [7] Duin, R.M., & Strom, R.G. 1975, A&A, 39, 33
- [8] Gardiner, C.W. 1983, *Handbook of Stochastic Methods*, Springer Verlag, Berlin, Ch. 4
- [9] Jones, F.C. 1990, ApJ 361, 162.
- [10] Kang, H., & Jones, T.W. 1991, MNRAS, 249, 439
- [11] Koyama, K., Petre, R., Gotthelf, E.V., Hwang, U., Matsuura, M., Ozaki, M., & Holt, S.S. 1995, Nature, 378, 255
- [12] Koyama, K. et al. 1997, PASJ, 49, L7

-
- [13] Krülls, W.M., Achterberg, A. 1994, *A&A*, 286, 314
- [14] LeVeque, R.J. 1998, in: *Computational Methods for Astrophysical Fluid Flow*, Saas Fee Adv. Course 27, R.J. LeVeque, D. Mihalas, E.A. Dorfi & E. Müller (Eds.), p.1, Springer Verlag, Heidelberg
- [15] MacKinnon, A. L., Craig, I. J. D. 1991, *A&A*, 251,693
- [16] Marcowith, A., Kirk, J. G. 1999, *A&A*, 347, 391
- [17] McKee, C.F., & Truelove, J.K. 1995, *Phys.Rep.*, 256, 157
- [18] Reynolds, S.P. 1998, *ApJ*, 493, 375
- [19] Reynolds, S.P., & Chevalier, R.A. 1981, *ApJ*, 245, 912
- [20] Rybicki, G.B., Lightman, A.P. 1979, *Radiative Processes in Astrophysics*, John Wiley & Sons, New York, Ch. 6
- [21] Saslaw, W.C., 1985, *Gravitational physics of stellar and galactic systems*, Cambridge Univ. Press, p.18.
- [22] Skilling, J. 1975, *MNRAS*, 172, 557.
- [23] Slane, P., Gaensler, B.M., Dame, T.M., Hughes, J.P., Plucinsky, P.P., & Green, A. 1999 *ApJ*, 525, 357
- [24] Slane, P., Hughes, John P., Edgar, Richard J., Plucinsky, Paul P., Miyata, E., Tsunemi, H., Aschenbach, B. 2001, *ApJ*, 548,81
- [25] Tóth, G., 1996, *Astrophys. Lett. & Comm.*, 34, 245
- [26] Tóth, G. & Odstrčil 1996 *J. Comp. Phys.*, 128, 82
- [27] Woltjer, L. 1972, *ARA&A*, 10, 129
- [28] Zeldovich, Ya.B., Ruzmaikin, A.A., Sokoloff, D.D. 1983, *Magnetic Fields in Astrophysics*, Gordon and Breach Science Publishers, p. 75

Chapter 6

Rejuvenating Shells of Supernova Remnants by Pulsar Winds

E. van der Swaluw, A. Achterberg and Y. A. Gallant

abstract

We reconsider the rejuvenation mechanism as proposed by Shull et al. (1989). These authors suggest that an active pulsar can rejuvenate the shell of its associated supernova remnant (SNR), at the moment when the pulsar breaks through the shell of the SNR. The morphology of the remnants G5.4-1.2 and CTB80 seem to confirm this rejuvenation mechanism. The spindown energy deposited by the pulsar, as a relativistic pulsar wind, has a magnitude, which is large enough to explain the observed radio emission structures observed in remnants where the rejuvenation mechanism seems at work.

Shull et al. (1989) did not explain the observed lengthscales of the rejuvenated parts of the SNR shell. Therefore one needs to consider the (diffusive) transport of the injected electrons by the pulsar wind. In this chapter, we investigate the physical diffusive conditions, needed to explain the observed lengthscales. We make a distinction between diffusion along the magnetic field line and perpendicular to the magnetic field line, which is parameterised by the gyrofactor η . We show that one has to assume a high value for the gyrofactor $\eta \simeq 10^{3-4}$, i.e. diffusion of the electrons along the magnetic field line is much faster than perpendicular to the magnetic field line, in order for the rejuvenation mechanism to work on the observed lengthscales. We discuss the consequences of this assumption on the overall distribution of the electrons at the shell of the SNR.

6.1 Introduction

A supernova remnant (SNR) results from the supernova explosion of a massive star. In some of these explosions the stellar core collapses to a pulsar, which gains a kick velocity at birth. Several mechanisms have been considered for giving the pulsar this kick velocity, such as an anisotropic explosion of the progenitor star, although none of them can be favoured from an observational point of view.

The expansion of the supernova remnant itself is decelerated by the surrounding interstellar medium (ISM), whereas the pulsar moves ballistically at a constant speed. This ultimately results in a break-through of the pulsar through the shell, which has been considered in Chapter 4 of this thesis. In that chapter we concluded that only high-velocity pulsars can break through the supernova remnant shell while the SNR is in the Sedov stage of its expansion. Furthermore we concluded that the interaction between the pulsar wind nebula bow shock around the pulsar and the shell of the remnant leads to a growth of the pulsar wind region, plus a slight enhancement of the density and pressure in the region between the pulsar wind bow shock and the shell of the SNR.

Shull et al. (1989) have argued that, during the interaction between the pulsar wind and the SNR shell, the radio emission from the SNR shell can be rejuvenated. They explain the radio brightening as due to the pulsar's relativistic electrons that have encountered the magnetic field lines in the shell. These electrons can propagate along the magnetic field lines and radiate at radio frequencies. Besides an apparently rejuvenated SNR shell, a diffuse plerionic component around the pulsar is observed in systems like CTB80 (Angerhofer et al. 1981) and G5.4-1.2 (Frail & Kulkarni 1991). For both cases one can see a trail of radio emission which, in the model of a pulsar catching up with the shell of the remnant, is a wake of radio electrons originating from the pulsar wind. In this respect the model seems quite consistent with observations. In this chapter we describe the propagation of the particles injected by the pulsar wind and describe the associated diffusion process. We estimate the diffusive length scales of the injected electrons in the lifetime of a SNR or their radiative lifetime. This will enable us to compare these results with actual lengthscales observed in these kind of systems. In this way, we can constrain the physical conditions needed for the rejuvenation mechanism to work. This chapter is organised as follows. Section 6.2 considers the physical configuration of the pulsar wind-SNR system. Section 6.3 discusses the lengthscales one gets for electron diffusion in the source.

Section 6.4 will apply this to three candidates where the rejuvenation process might be at work: CTB80, G5.4-1.2 and G341.2+0.9 (Frail et al. 1994). Section 6.5 will consider the results of section 6.4 in more detail by using a numerical simulation. Section 6.6 contains the conclusions.

6.2 Rejuvenation

We consider the case where a pulsar has just caught up with the front of a SNR. In this situation there are two main components. First there is the decelerating shell of the SNR. Secondly there is the pulsar wind nebula (PWN) associated with the pulsar moving at constant speed. For typical parameters, the SNR shell at this stage of its evolution is a slowly fading radio source. The reason for the increasingly weak emission is twofold: (1) due to the deceleration of the SNR shock, it is less efficient in accelerating particles to radio-emitting energies, (2) the accelerated particles from the first (more energetic) stage of the SNR have lost a significant amount of their energy due to synchrotron losses, and adiabatic losses in the remnant's interior. The pulsar wind associated with the pulsar, on the other hand, consists of an ultra-relativistic, cold flow with a high Lorentz factor ($\Gamma_w \geq 10^6$). This flow is thermalised by a termination shock, leading to a relativistically hot bubble. Because of the low sound speed in the SNR interior with respect to the pulsar velocity, the hot bubble is deformed to a bow shock. The size of the pulsar wind nebula is very small (~ 0.01 parsec) compared with the size of the SNR (~ 30 parsec).

In principle there are two ways to achieve a rejuvenation of the SNR shell: (1) the bow shock bounding the pulsar wind nebula (PWN) reaccelerates electrons already present in the SNR shell to higher energies; (2) the pulsar wind itself rejuvenates the shell of the SNR by injecting fresh already highly relativistic electrons. In this chapter we will take the pulsar wind as the source for radio electrons, and do not discuss the details about the origin of these electrons. The main point of this chapter is how the freshly injected electrons diffuse in the PWN/SNR system. The basic geometry of the system is illustrated in figure 6.1.

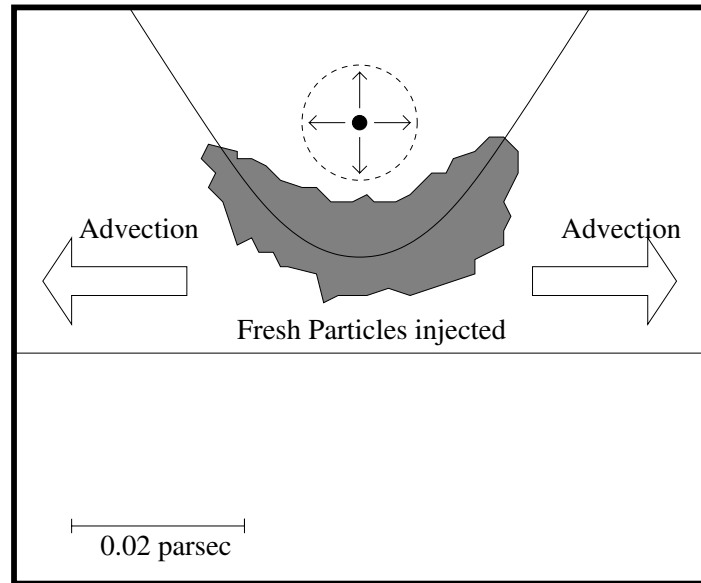


Figure 6.1: Configuration of the system considered in our calculations: the pulsar wind is terminated by a wind shock (dashed line). The pulsar wind nebula itself is bounded by a bow shock. Closeby is the supernova remnant shock. The re-energised particles of the supernova remnant of the freshly injected particles of the pulsar wind nebula have to propagate along this SNR shock in order to be visible at radio frequencies.

6.2.1 Diffusion of radio electrons

General considerations

Relativistic electrons in astrophysical flows radiate part of their energy as synchrotron radiation due to the presence of a magnetic field, B in the plasma. During this emission process a relativistic electron, with Lorentz factor γ , mass m_e and charge e , radiates at a characteristic frequency ν_s (the frequency where the emission spectrum peaks), which equals (Rybicky & Lightman 1979):

$$\begin{aligned}\nu_s &= 0.29 \frac{3\gamma^2 q B}{4\pi m_e c}, \\ &\simeq 4.67 B_{\mu G} E_{\text{GeV}}^2 \text{ MHz.}\end{aligned}\quad (6.1)$$

The associated timescale τ_{loss} , after which half of the energy of the electron has been lost due to synchrotron radiation, equals:

$$\begin{aligned}\tau_{\text{loss}} &= \frac{6\pi m_e c}{\sigma_T B^2 \gamma}, \\ &\simeq 2 \times 10^9 B_{\mu G}^{-3/2} \nu_{\text{MHz}}^{-1/2} \text{ yr.}\end{aligned}\quad (6.2)$$

Here σ_T is the Thomson cross section, $\sigma_T = 6.6 \times 10^{-25} \text{ cm}^2$. The propagation of relativistic particles through the flow of the plasma is a combination of advection by the large-scale flow, and diffusion with respect to this flow, mediated by the (gyro-)resonant interaction with Alfvén waves (e.g. Skilling 1975a&b). For the diffusion mechanism we consider the limit of Bohm diffusion, where the mean free path λ , equals the gyroradius r_g defined as $r_g = pc/qB$, where c is the light speed. The Bohm diffusion coefficient equals $\kappa_B = \frac{1}{3}c\lambda = \frac{1}{3}cr_g$. Expressing κ_B in terms of the characteristic frequency ν_s at which the synchrotron spectrum peaks, the diffusion coefficient can be written as:

$$\kappa_B(\nu) = 7.5 \times 10^{21} \nu_{\text{MHz}}^{1/2} B_{\mu G}^{-3/2} \text{ cm}^2/\text{sec.}\quad (6.3)$$

Now consider particles injected at $t = 0$. The diffusion lengthscale, ΔR_{syn} , at the synchrotron loss time τ_{loss} equals for Bohm diffusion:

$$\Delta R_{\text{syn}} = 9.7 B_{\mu G}^{-3/2} \text{ parsec.}\quad (6.4)$$

Notice that the observing frequency drops out in this expression. These values will be used for reference in the more general case where the mean free path λ satisfies $\lambda \gg r_g$.

Radio electrons from a pulsar wind

Consider the case where the pulsar wind is sufficiently close to the shell of a SNR. We investigate the length scales associated with the injected radio electrons in such a considered configuration. Because of the small size of the PWN, when compared with the SNR, we can approximate the source of radio electrons as a point source in the SNR interior. Normalising the timescale to the crossing time for a pulsar moving at speed V_{psr} with the SNR shell, $R_{\text{snr}}/V_{\text{psr}} \propto 10^4$ years, we can write the diffusion lengthscale for radio electrons as:

$$\Delta R_{\text{radio}} \simeq 2.2 \times 10^{-2} \nu_{\text{MHz}}^{1/4} B_{\mu\text{G}}^{-3/4} (R_{\text{snr}}/V_{\text{psr}})^{1/2} \text{ parsec}, \quad (6.5)$$

where R_{snr} is the radius of the SNR in parsec, V_{psr} is the velocity of the pulsar in units of 100 km/sec, and we again assume Bohm diffusion. This lengthscale is similar to the size of the PWN itself, i.e. the radio electrons are more or less confined to the immediate surroundings of the PWN. In order to diffuse into the SNR over distances as large as the observations seem to imply, we extend our diffusion model in the following way: we make a distinction between diffusion along the magnetic field lines (κ_{\parallel}) and perpendicular to the magnetic field (κ_{\perp}). The mean free path along the magnetic field line then equals $\lambda_{\parallel} = \eta r_g$, with η the gyrofactor, which is related to the turbulence level δB in the magnetic field by $\eta = (\delta B/B)^{-2}$. The diffusion coefficient along the magnetic field lines equals:

$$\kappa_{\parallel} = \eta \kappa_B \quad (6.6)$$

One usually assumes $\eta \gg 1$. Perpendicular to the magnetic field lines we follow Jokipii (1987) and assume that a particle scatters one gyroradius across field lines for every parallel scattering length, so:

$$\kappa_{\perp} = \eta \kappa_{\parallel} / (1 + \eta^2) \simeq \kappa_{\parallel} / \eta \quad (6.7)$$

With this description for diffusion particles diffuse faster along the magnetic field lines then compared with quasi-isotropic Bohm diffusion. Using this description together with the timescale for synchrotron losses, τ_{loss} , one can write the diffusion length scale at time t of the radio electrons as:

Table 1: Investigated systems

| SNR | pulsar | age (in years) | frequency | distance (in parsec) |
|------------|--------------|-------------------|-----------|----------------------|
| CTB80 | PSR 1951+32 | 10^5 | 600 MHz | 2.0 |
| G5.4-1.2 | PSR B1757-24 | 1.6×10^4 | 330 MHz | 2.0 |
| G341.2+0.9 | PSR 1643-43 | 3.3×10^4 | 1.5 GHz | 6.9 |

$$\Delta R_{\parallel} = \Delta R_{\text{syn}} \times \left(\frac{\kappa_{\parallel}}{\kappa_{\text{B}}} \right)^{1/2} \times \left(\frac{t}{\tau_{\text{loss}}} \right)^{1/2} \text{ parsec}, \quad (6.8)$$

with ΔR_{syn} given by equation (6.4). This gives the diffusive lengthscale along the magnetic field, where the diffusion proceeds rapidly.

6.3 Comparison with observations

In this section, we will use equation (6.8) to determine a value for η in order to get to lengthscales ΔR observed in a number of remnants where rejuvenation processes are thought to occur. We make the following two assumptions, both of which lead to a lower limit for the gyrofactor η :

1) the timescale t for the interaction between the pulsar wind and the shell of the remnant is taken to be the age of the remnant, instead of the interaction time which will be less;

2) the diffusion process is assumed to take place in a uniform magnetic field rather than in a curved, position-dependent magnetic field.

We consider three different SNRs, observed at radio frequencies. From the distance to the SNR, the observed frequency and the age one can derive all the parameters of interest needed to derive the length scales of the radio arms, and the minimum value for the gyrofactor η needed to explain these radio arms using the rejuvenation mechanism. The table summarises all the relevant parameters of the considered remnants.

6.3.1 CTB80 and PSR 1951+32

Figure 6.2 shows the SNR CTB80. The radio arms are clearly visible, which started the idea of a rejuvenation mechanism. The radio arms emanate from a more compact core where the pulsar is located, together with the associated PWN. The PWN shows a wake of particles, one expects for a PWN associated with a supersonically moving pulsar. The observation frequency equals 600 MHz. At an assumed distance of ~ 2 kpc (Strom & Stappers, 2000), each radio arm has a lengthscale of ~ 17 parsec. The assumed age of the system equals 10^5 years, derived from the characteristic age of the associated pulsar. With the above parameters one gets $\tau_{\text{loss}}(600 \text{ MHz}) = 8.2 \times 10^7 B_{\mu\text{G}}^{-3/2}$ years. Combining this with equation (6.8), we derive a minimum value for the gyrofactor needed to get the observed lengthscales from field-aligned diffusion of the radio electrons:

$$\eta \geq 2.5 \times 10^3 B_{\mu\text{G}}^{3/2}. \quad (6.9)$$

6.3.2 G5.4-1.2 and PSR B1757-24

The system of G5.4-1.2 was observed recently by Gaensler and Frail (2000). They derived a new limit for the velocity of the pulsar. Their map is at a frequency of 330 MHz. The characteristic age of the pulsar equals 1.6×10^4 yr and the assumed distance to the system is ~ 2.0 kpc. For this distance the radio arms observed in the associated remnant have a length of ~ 15 parsec. From these parameters we derive a value for the loss time $\tau_{\text{loss}}(330 \text{ MHz}) = 10^8 B_{\mu\text{G}}^{-3/2}$ years. Together with equation (6.8) the derived loss time corresponds to

$$\eta \geq 1.4 \times 10^4 B_{\mu\text{G}}^{3/2}. \quad (6.10)$$

6.3.3 G341.2+0.9 and PSR 1643-43

The system of G341.2+0.9 was observed by Frail et al.(1994) at 1.5 GHz. The system is at a distance of ~ 6.9 kpc (Taylor & Cordes 1993) and the pulsar's characteristic age is 32.6 kyr. This implies that the radio arms observed have a size ~ 15 parsec. The synchrotron loss time at this frequency equals $\tau_{\text{loss}}(1.5 \text{ GHz}) = 5.2 \times 10^7 B_{\mu\text{G}}^{-3/2}$ yr. These values when substituted in equation (6.8) yield:

$$\eta \geq 3.6 \times 10^3 B_{\mu\text{G}}^{3/2}. \quad (6.11)$$

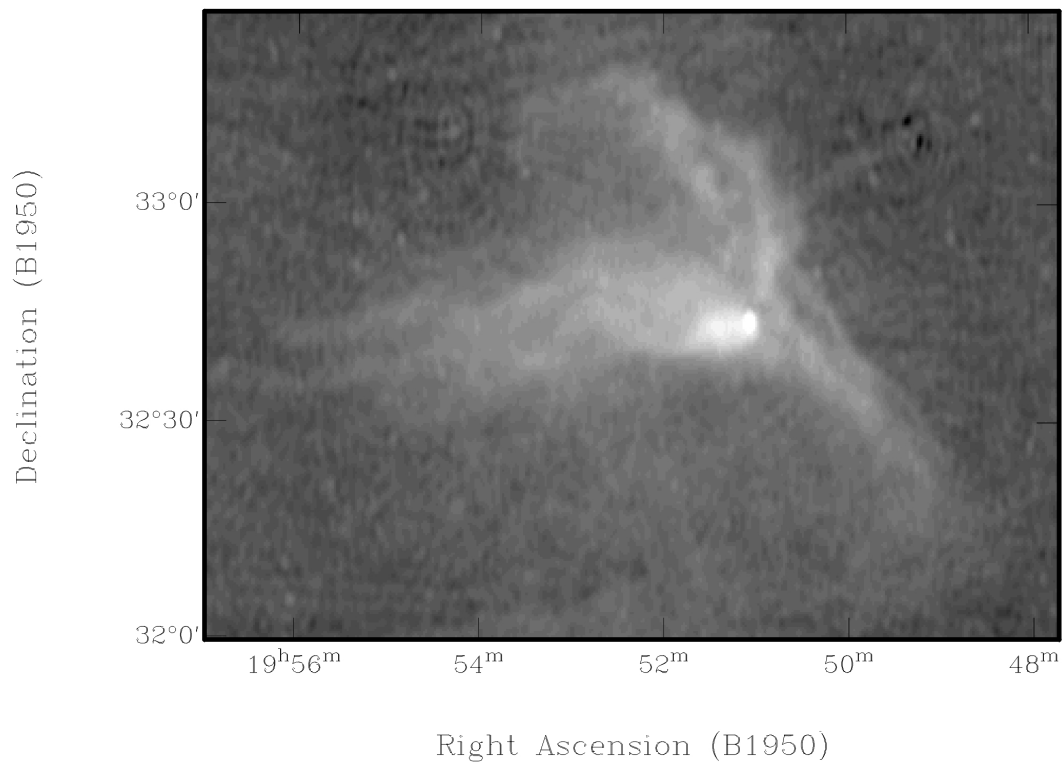


Figure 6.2: *Radio image of the SNR CTB80. The data are from WSRT at a frequency of 600 MHz (R. Strom & B. Stappers 2000).*

Conclusions

We have shown that, in order to explain the observed radio arms in three SNRs by a rejuvenation process as suggested by Shull et al. (1989), one has to introduce a minimum value for the gyrofactor of order $\eta \geq 10^{3-4}$. This means that the level of turbulence in these remnants must be small $\delta B \simeq B/\sqrt{\eta} \simeq 0.01 - 0.03B$. In section 6.5 we investigate the consequences of such a value for the observed radio profiles in a SNR.

6.4 Numerical Simulations

In Chapter 4 of this thesis, we presented results of hydrodynamical simulations of a pulsar wind nebula bounded by a bow shock. In this section we combine the hydrodynamics code with a Monte-Carlo method, which traces the position of test particles injected at the pulsar wind termination shock.

Formally, in order to calculate the propagation and acceleration of particles in astrophysical plasmas, one has to solve a Fokker-Planck equation:

$$\frac{\partial F(\mathbf{Z}, t)}{\partial t} = \frac{\partial}{\partial \mathbf{Z}} \cdot \left(-\dot{\mathbf{Z}} F(\mathbf{Z}, t) + \frac{\partial}{\partial \mathbf{Z}} \cdot [\mathbf{D} F(\mathbf{Z}, t)] \right). \quad (6.12)$$

Here $\mathbf{Z} \equiv (\mathbf{x}(t), \mathbf{p}(t))$ describes the position of the particle in phase space, $F(\mathbf{Z}, t)$ is the particle distribution function of the system at time t , $\dot{\mathbf{Z}}$ is the advection velocity in phase space and \mathbf{D} is the diffusion tensor. It has been shown (e.g. Gardiner 1983, Saslaw 1985) that the Fokker-Planck equation corresponds to the stochastic differential equation (SDE) of the Itô form:

$$d\mathbf{Z} = \dot{\mathbf{Z}}(\mathbf{Z}, t) dt + 2^{1/2} \sqrt{\mathbf{D}} \cdot d\mathbf{W}. \quad (6.13)$$

The term $d\mathbf{W}$ entering in the stochastic part of this equation is a $2N$ -dimensional Wiener process, where N is the number of degrees of freedom in phase space (e.g. MacKinnon & Craig (1991), Krülls & Achterberg (1994)). The Wiener process is chosen at each time step dt from a Gaussian distribution, in such a way that $\langle dW_i \rangle = 0$ and the variance satisfies (in component form) $\langle dW_i dW_j \rangle = \delta_{ij} dt$.

This correspondence between an Itô stochastic differential equation and the Fokker-Planck equation allows for a fast simulation method (Achterberg & Krülls (1992)) capable of calculating the particle acceleration and particle propagation in astrophysical flows. We do not consider particle acceleration in this chapter,

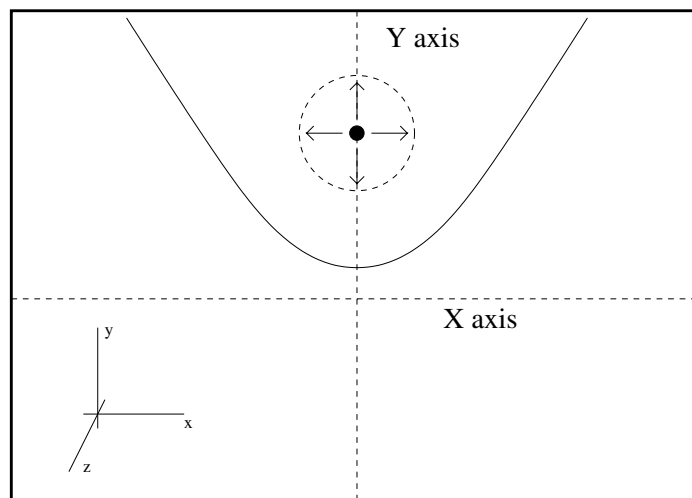


Figure 6.3: Configuration of the system of pulsar wind and bow shock. The magnetic field lines are aligned with the x -axis. Diffusion of electrons along these magnetic field lines proceeds faster than perpendicular to the magnetic field lines ($\eta \gg 1$). Except in the pulsar wind bubble where diffusion is taken isotropic ($\eta = 1$).

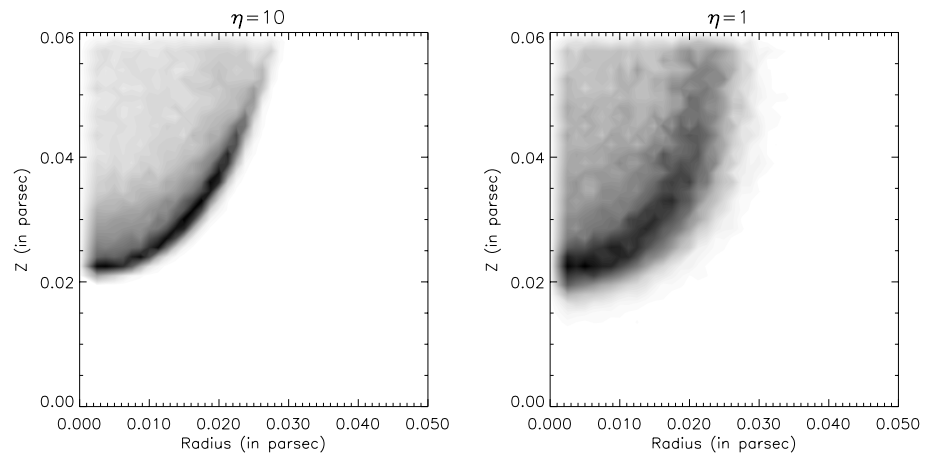


Figure 6.4: Synchrotron map at X-ray frequencies for a simulation with gyrofactor $\eta = 1$ (right) and gyrofactor $\eta = 10$ (left). For a gyrofactor $\eta = 10$, the emission profile become much sharper compared with emission profile with $\eta = 1$.

as we are only interested in the distribution of particles continuously injected at the pulsar wind termination shock. The position of the particles is changed each time step according to:

$$d\mathbf{x} = \mathbf{U}_{\text{fl}} dt + \sqrt{2D(\mathbf{x}) dt} \xi . \quad (6.14)$$

The velocity \mathbf{U}_{fl} is obtained from the hydrodynamics code. The stochastic term $\propto \sqrt{2D(\mathbf{x}) dt}$ uses a random number ξ , drawn from a Gaussian distribution with zero mean and unit variance, in effect writing $dW = \sqrt{dt} \xi$.

The geometry of the pulsar wind-bow shock system is taken to be axially symmetric around the y-axis (see figure 6.3). The magnetic field is taken along the x-axis (see figure 6.3). We employ anisotropic diffusion as described in section 6.2, which means that the Monte Carlo method has to be applied in 3D.

The simulations use a value of the diffusion coefficient $\kappa \sim 10^{28}$, assuming Bohm diffusion. For these values, the corresponding electrons would radiate at X-ray frequencies in a $\sim 10 - 100 \mu\text{G}$ magnetic field. However the simulations here are performed to give a qualitatively result, which can be used to illustrate the effect of a gyrofactor $\eta \neq 1.0$.

We present results from two simulations. In the first simulation the diffusion coefficient is quasi-isotropic ($\eta = 1$), in the second simulation the diffusion is mostly along the magnetic field lines, with a value for the gyrofactor $\eta = 10$. The results are shown in the figures 6.4 and 6.5. Two effects are visible from the comparison between these two cases: 1) When the diffusion is not isotropic, the particles can diffuse further away from their place of injection as compared with particles which diffuse isotropically, as expected. 2) Figure 6.5 on the other hand illustrates that dependent on the angle between the observer and the magnetic field, the effect introduced by the gyrofactor has its maximum effect when the PWN is observed from a direction perpendicular to the magnetic field in which the PWN is embedded.

6.5 Discussion

We have reconsidered the rejuvenation mechanism as proposed by Shull et al. (1989). This was done by deriving values for the gyrofactor, η , needed to get diffusive length scales which are comparable with the observed size of the radio arms in three supernova remnants: CTB80, G5.4-1.2 and G341.2+0.9. A numerical simulation was conducted to see the consequences of a high value for this gyrofactor. The conclusions of this work are as follows:

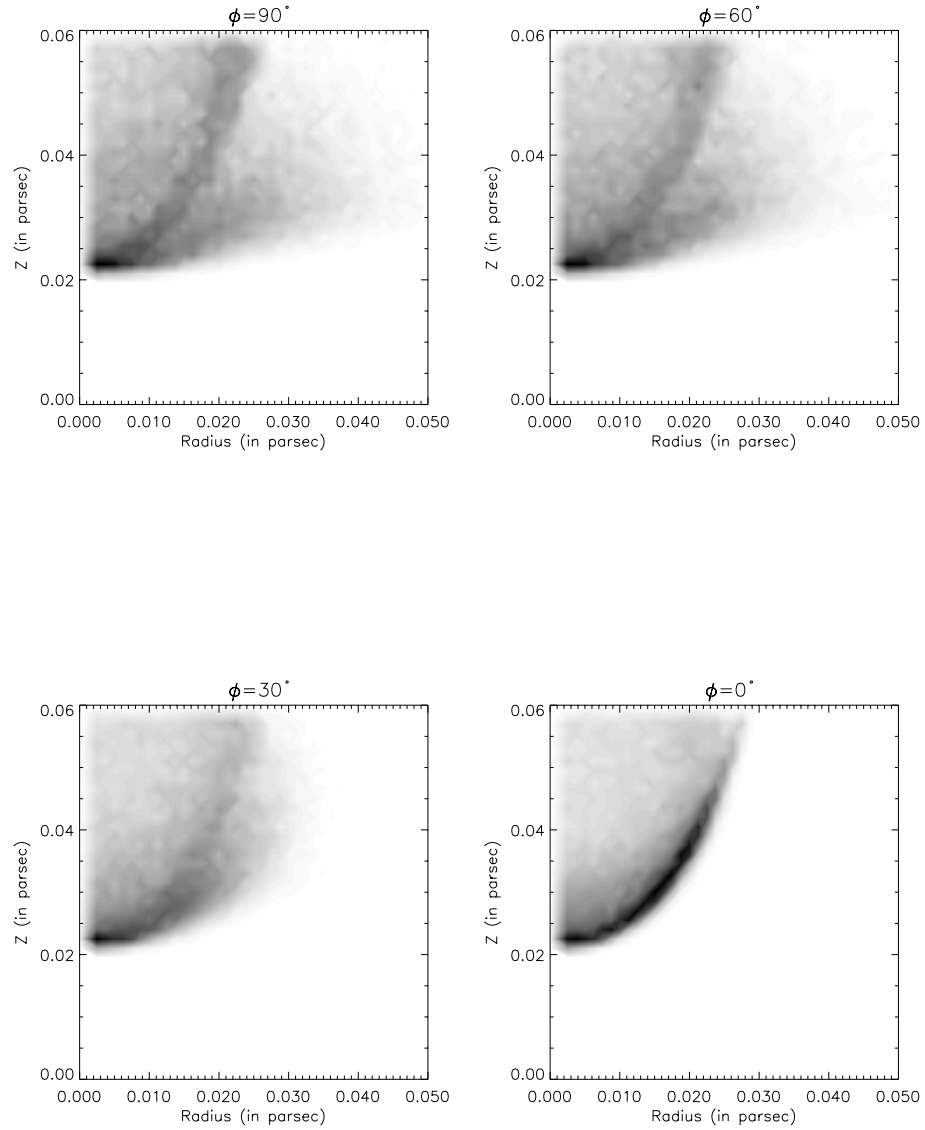


Figure 6.5: Synchrotron map at X-ray frequencies, illustrating the effect of different angles of observation with the gyrofactor, $\eta = 10$. The figure has arm-like features for $\phi = 90^\circ$, which disappear for $\phi = 0^\circ$.

- The gyrofactor has to have a minimum value $\eta \geq 10^{3-4}$ in order to let rejuvenated particles diffuse over length scales, comparable with the observed size of the radio arms;
- As a consequence, this implies that the diffusion of particles perpendicular to the magnetic field proceeds very slowly. Dependent on the orientation of the magnetic field with the shock this influences the precursor of the SNR shock.

Under the circumstances we assumed, i.e. the diffusion time equals the age of the SNR and the diffusion is along a uniform planar field the derived value for the gyrofactor η is a minimum value. The reason is twofold:

- The velocity of the pulsar has to be perpendicular to the magnetic field orientation where the pulsar crosses the shock. If this is not the case the value for the gyrofactor has to be increased.
- The angle of observation has to be such that the system is observed almost perpendicular to the pulsar's velocity, otherwise one sees part of the rejuvenated shell in projection.

We can summarise by mentioning that there are problems with the rejuvenation scenario as an explanation for the brightening of SNR shells to occur and brighten the supernova remnant over large scales. Although energetically there might be no problem, one needs a diffusion mechanism with a gyrofactor in the range $\eta \geq 10^{3-4}$ and a special field geometry. Since there are more SNRs observed where only one shell is brightened at radio frequencies without a pulsar wind connected with the system, it becomes questionable whether the pulsar wind is indeed responsible for the brightening of the shell of a SNR like CTB80, G5.4-1.2 and G341.2+0.9. or whether environmental reasons are responsible.

Bibliography

- [1] Achterberg, A., & Krülls, W.M., 1992, A&A, 265, L13
- [2] Angerhofer, P.E., Strom, R.G., Velusamy, T., Kundu, M.R. 1981, A&A, 94, 313
- [3] Frail, D.A., Goss, W.M., Whiteoak, J.B.Z., 1994 Ap. J. 437, 781
- [4] Frail, D.A., Kulkarni, S.R. 1991, Nature, 352, 759
- [5] Gaensler, B. M., Frail, D. A. 2000, Nature, 406, 158
- [6] Gardiner, C.W. 1983, *Handbook of Stochastic Methods*, Springer Verslag, Berlin, Ch. 4
- [7] Jokipii, J.R. 1987, ApJ, 313, 842
- [8] Krülls, W.M., Achterberg, A., 1994, A&A, 286, 314
- [9] Rybicki, G.B., Lightman, A.P. 1979, *Radiative Processes in Astrophysics*, John Wiley & Sons, New York, Ch. 6
- [10] Saslaw, W.C. 1985, *Gravitational physics of stellar and galactic systems*, Cambridge Univ. Press, p. 18
- [11] Shull, J. Michael, Fesen, Robert A., Saken, Jon M. 1989, ApJ, 346, 860
- [12] Skilling, J. 1975a, MNRAS, 172, 557
- [13] Skilling, J. 1975b, MNRAS, 172, 567
- [14] Strom, R.G., Stappers, B.W. 2000, *Pulsar Astronomy - 2000 and Beyond*, ASP Conference Series, Vol. 202; Proceedings of the 177th Colloquium of the IAU held in Bonn, Germany, 30 August - 3 September 1999. (San Francisco: ASP), Edited by M. Kramer, N. Wex, and N. Wielebinski, p. 509

- [15] Taylor, J. H., Cordes, J. M. 1993, ApJ, 411, 674

Chapter 7

Inferring Initial Spin Periods for Neutron Stars in Composite Remnants

E. van der Swaluw and Y. Wu

abstract

We propose a method to infer the initial spin period of pulsars residing in composite supernova remnants. Such a remnant consists of both a plerionic and a shell type component, corresponding respectively to the pulsar wind nebula driven by the spindown luminosity of the central pulsar, and the blastwave bounding the supernova remnant. Theoretical investigations including hydrodynamical simulations have shown that at late times ($\sim 1,000 - 10,000$ years), a simple scaling law connects the radius of the supernova shell to the radius of the plerion. The energy content of the plerion and the total mechanical energy of the supernova remnant enter into this scaling law. One can use this scaling law to estimate the initial spin period of pulsars residing in composite remnants. We discuss potential pitfalls of this method, including the effect of a small remnant age and of strong radiative losses in the plerion.

7.1 Introduction

Is a typical neutron star born spinning close to break-up ($P_0 \sim 0.8$ ms, Haensel *et al.* (1995)). The answer to this question is of significance for evolutionary scenarios for the angular momentum of neutron star progenitors (Heger *et al.* 2000), as well as for the processes that occur during the stellar collapse preceding a supernova (Spruit & Phinney 1998, Lai & Goldreich 2000). If the initial spin-rate is close to the break-up rate, the nascent neutron star may undergo a Rossby-wave instability (Lindblom, Owen & Morsink 1998) and emit gravitational radiation. Moreover, a rapidly rotating neutron star can obtain a substantial kick velocity through the electromagnetic rocket effect (Harrison & Tademaru 1975). This can provide a natural explanation for the apparent alignment between the spin axis and pulsar proper motion (Lai *et al.* 2000) in the Crab (Caraveo & Mignani 1999) and Vela pulsar (Pavlov *et al.* 2000).

A number of studies have been dedicated to the determination of the initial spin-rates. Those few young pulsars which have measured braking indices and estimated ages seem to possess initial spin periods from 19 ms (Crab, Lyne *et al.* 1993) to 63 ms (PSR B1509-58, Kaspi *et al.* 1994).¹ Since only rapidly rotating pulsars have a measurable braking index, these results are not likely to reveal the initial spin of the general population. For these, Phinney & Blandford (1981) and Vivekanand & Narayan (1981) have developed the pulsar-current analysis. Unfortunately, this method is subject to small-number statistics (Lorimer *et al.* 1993). Analysis based on pulsar luminosity functions (Emmering & Chevalier 1989, Narayan 1987) raised the possibility of 'injection': the majority of the pulsars may be born with periods as slow as several hundred milliseconds. This hypothesis is corroborated by the apparent paucity of plerions around neutron stars (Srinivasan *et al.* (1984)). A plerion derives its energy from a rapidly rotating neutron star. The overall conclusion from pulsar studies seems to favour a slow initial spin rate.

In this chapter, we propose a new method for inferring the initial spin-rates of some neutron stars – the small population that reside within composite supernova remnants. A composite supernova remnant (SNR) includes both a plerionic (filled-centered) component (Weiler & Panagia 1978) and a shell component. The first corresponds to the pulsar wind nebula (PWN), while the latter corresponds to the blastwave of the supernova remnant (SNR) propagating through

¹The LMC x-ray pulsar J0537-6910 (16 ms, Marshall *et al.* 1998) should be born at shorter than 10 ms for reasonable values of the braking index

the interstellar medium (ISM). They are observationally distinguished by a different spectral power-law index at radio frequencies. The dynamics of such a composite system has been extensively studied, e.g. Reynolds & Chevalier (1984); Chevalier & Fransson (1992).

Recently, Van der Swaluw *et al.* (2001) presented hydrodynamical simulations and analytical arguments which explicitly relate the radius of the PWN with that of the SNR. These authors find that the two radii are roughly proportional some time after the initial explosion, with the proportionality constant determined by the ratio of the spin-down energy of the pulsar and the total mechanical energy of the supernova event. This relation forms the theoretical basis for the current Chapter. In this Chapter, we follow Van der Swaluw *et al.* (2001) by restricting ourselves to spherically symmetric systems.

7.2 Evolution of a PWN in a SNR

As a pulsar spins down, its rotational energy is largely deposited into the surrounding medium, driving a relativistic pulsar wind into the tenuous bubble of stellar debris left behind by the supernova blastwave. We approximate the spin-down luminosity of the pulsar wind by that of a rotating magnetic dipole:

$$L(t) = \frac{L_0}{(1 + t/\tau)^2}. \quad (7.1)$$

The total spin-down energy is $E_{\text{sd}} = L_0\tau$. We neglect the dynamical influence of the pulsar wind on the SNR, assuming that E_{sd} is well below the total mechanical energy of the supernova explosion, $E_0 \sim 10^{51}$ erg.

The evolution of a PWN inside a SNR can be divided into two stages (Reynolds & Chevalier, 1984; Chevalier & Fransson, 1992). In the first stage, the PWN expands supersonically within the bubble blown out by the SNR. The second stage commences when the PWN encounters the reverse shock which propagates into the SNR interior, and which signals the end of the free expansion stage. We denote this time by $t = t_{\text{ST}}$. The reverse shock heats up the interior of the SNR and the expansion of the PWN becomes subsonic. In this stage the expansion of the PWN is regulated by the expansion of the SNR, which is described by a self-similar Sedov-Taylor solution. In the following we summarize some relevant results from Chevalier & Fransson (1992) and Van der Swaluw *et al.* (2001).

7.2.1 Analytical Relations

We focus on the subsonic expansion stage of the PWN which occurs when the SNR has relaxed to the Sedov solution. We assume that the pulsar wind has deposited most of its energy into the PWN ($t_{\text{ST}} \gg \tau$). We find that the radius of the PWN (R_{pwn}) scales roughly linear with the radius of the SNR (R_{snr}). This scaling arises from the condition of pressure equilibrium between the PWN interior and the interior of the SNR. We approximate the pressure which confines the PWN by the central pressure of the SNR, using the Sedov solution (Sedov 1958),

$$P_{\text{snr}} \simeq 0.074 E_0 / R_{\text{snr}}^3, \quad (7.2)$$

where E_0 is the total mechanical energy of the SNR. Inside the PWN, pressure is quickly equilibrated due to the high sound speed $\sim c/\sqrt{3}$ of the relativistic fluid. The interior pressure is related to the energy content (E_*) of the PWN by

$$P_{\text{pwn}} \simeq \frac{3(\gamma - 1)}{4\pi} \frac{E_*}{R_{\text{pwn}}^3}, \quad (7.3)$$

where γ is the adiabatic index. Let E_{pwn} be the amount of energy injected into the PWN by the central pulsar. Part of this energy is used to perform work on the surrounding medium as the PWN expands. As a result E_* falls below E_{pwn} . Following van der Swaluw *et al.* (2001), we write $E_* = \eta_2 E_{\text{pwn}}$ with $\eta_2 < 1$ decreasing over time. Imposing pressure equilibrium, we find

$$R_{\text{pwn}} = \bar{C} (E_*/E_0)^{1/3} R_{\text{snr}}, \quad (7.4)$$

where $\bar{C} \simeq 1.02$ for a relativistic fluid ($\gamma = 4/3$) and $\bar{C} \simeq 1.29$ for a non-relativistic fluid ($\gamma = 5/3$).

In absence of radiative losses, the subsonic expansion of the PWN is adiabatic, $P_{\text{pwn}} V_{\text{pwn}}^\gamma = \text{constant}$, where $V_{\text{pwn}} \propto R_{\text{pwn}}^3$ is the volume of the PWN. Combining this relation with equation 7.3, we find that E_* falls off with time as $t^{-3/10}$ for a relativistic fluid. This yields an expansion law for the radius of the PWN, $R_{\text{pwn}} \propto t^{3/10}$, whereas the radius of the SNR scales as in a Sedov solution ($R_{\text{snr}} \propto t^{2/5}$). Roughly, $R_{\text{pwn}} \propto R_{\text{snr}}$.

We introduce two additional dimensionless parameters, η_1 and η_3 , and rewrite equation 7.4 into a form that can be more easily compared with simulations,

$$R_{\text{pwn}}(t) = \eta_3(t) (\eta_1 E_{\text{sd}}/E_0)^{1/3} R_{\text{snr}}(t). \quad (7.5)$$

The parameter η_1 is a constant and relates the total energy input into the PWN, E_{pwn} , to the total spin-down energy of the pulsar, E_{sd} as $E_{\text{pwn}} = \eta_1 E_{\text{sd}}$. This takes into account possible radiative losses in the PWN, and other inefficiencies in the conversion of the spin-down energy into mechanical energy. For instance, a fraction of the neutron star spin-down energy may escape directly from the pulsar as high energy radiation. We set $\eta_1 = 1$ in this chapter, but discuss the case when it is much less than unity. The second parameter is defined as $\eta_3(t) = \bar{C}\eta_2^{1/3} \leq \bar{C}$. The maximum value of η_3 , $\eta_3 = \bar{C}$ is used when we determine the initial spin periods of pulsars driving composite remnants.

Equation 7.5 can be applied formally to the early (supersonic) stage of the PWN evolution. But its meaning and interpretation become unclear. In the following, we demonstrate the behaviour of η_3 throughout the PWN evolution using results from hydrodynamical simulations.

7.2.2 Hydrodynamical Simulations

Van der Swaluw *et al.* (2001) have presented hydrodynamical simulations of a pulsar wind nebula inside a supernova remnant. In these simulations, the gasdynamical equations are integrated in a spherically symmetric configuration, using the Versatile Advection Code (VAC) developed by Gábor Tóth at the Astronomical Institute Utrecht (Tóth and Odstrčil, 1996). Lacking the possibility of treating a relativistic fluid, the pulsar wind has been implemented as a cold non-relativistic wind ($\gamma = 5/3$) with a terminal velocity equal to the speed of light, $v_\infty = [2L(t)/\dot{M}_{\text{pw}}(t)]^{1/2} \simeq c$, where $\dot{M}_{\text{pw}}(t)$ is the mass ejection rate into the pulsar wind bubble, and $L(t)$ is the pulsar spin-down luminosity as given by equation 7.1.

Figure 7.1 presents relevant results from one of these simulations. The thin solid line represents the radius of the PWN as a function of time, while the thicker line shows the behaviour of η_3 . One can clearly distinguish between the supersonic and the subsonic expansion stage in the figure. The numerical parameters adopted in this simulation are listed in the caption. Taking different parameters will not qualitatively change the overall behaviour of the system, but it will affect the early (supersonic) evolution and the moment when subsonic expansion commences (t_{ST}). For example, t_{ST} is later if the supernova explosion is more energetic, if the supernova ejecta mass is larger, or if the interstellar medium density is smaller ($t_{\text{ST}} \propto E_0^{-1/2} M_{\text{ej}}^{5/6} \rho_{\text{ism}}^{-1/3}$, e.g. McKee & Truelove, 1995). Since this is a non-relativistic simulation with $\gamma = 5/3$, we observe $\eta_3 \leq \bar{C} = 1.29$ in the subsonic expansion stage. In our investigation we assume

a maximum value of η_3 of 1.02, as is appropriate for the relativistic fluid.

7.3 Inferring Initial Spin Rates

Writing the spin-down energy as $E_{\text{sd}} = (\Omega_0^2 - \Omega_t^2)I/2$, we obtain the following expression for the pulsar's initial spin period,

$$P_0 = 2\pi \left(\frac{2E_0}{\eta_1 I} \left(\frac{R_{\text{pwn}}}{\eta_3 R_{\text{snr}}} \right)^3 + \Omega_t^2 \right)^{-1/2}, \quad (7.6)$$

where the spin-periods are $P_0 \equiv 2\pi/\Omega_0$, $P_t \equiv 2\pi/\Omega_t$ and I is the moment of inertia of the neutron star. The radius of a PWN relative to its associated SNR shell can be used to infer the initial spin-period of the pulsar, assuming η_1 , η_3 , E_0 and Ω_t are known or can be estimated.

PWN can be observed at radio frequencies. Electrons that produce synchrotron radio-emission have a typical life-time (Rybicki & Lightman (1979)):

$$\tau_{1/2} = \frac{6\pi m_e c}{\sigma_T B^2 \Gamma} \sim 10^5 B_{\text{mG}}^{-3/2} \nu_{\text{MHz}}^{-1/2} \text{ yrs}, \quad (7.7)$$

where σ_T is the Thomson cross-section, Γ is the electron Lorentz factor, ν is the typical synchrotron frequency. The magnetic field B and frequency ν have been scaled by their appropriate values. Such a long life-time implies that radio observations 'see' electrons accelerated during the early energetic stage, when the pulsar deposits most of its rotational energy into the pulsar wind. They therefore delineates the true spatial extent of the plerion. In contrast, X-ray electrons loose their energy quickly. Therefore, the X-ray plerion is produced by electrons recently accelerated near the pulsar. As a result one expects the plerion to be smaller in X-rays.

We have collected from the literature 13 composite supernova remnants. We list the relevant properties of these systems in Table 7.1. The relative sizes of the plerions are taken from radio observations, with the exception of G11.2 – 0.3 and G320.4 – 1.2 (marked by asterisks), where only X-ray plerions have been observed. We apply equation 7.6 to determine the initial spin period for these systems, adopting $\eta_1 = 1.0$, $\eta_3 = 1.02$, $E_0 = 1.0 \times 10^{51}$ erg, $I = 1.4 \times 10^{45}$ g cm² (the value for Crab), and $P_t = 2\pi/\Omega_t = \infty$ in cases where it is unknown. The same results appear in Figure 7.2 as filled triangles. By taking the maximum value for η_3 we probably under-estimate the initial spin rate, but likely by no more

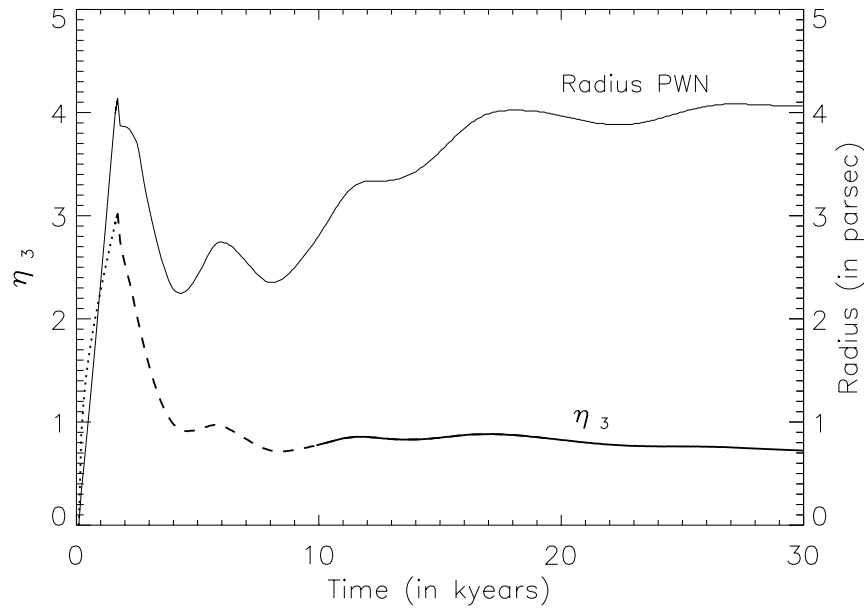


Figure 7.1: Results of numerical simulation showing the time evolution of the pulsar wind nebula. Plotted here are its radius (in units of parsec, thin continued line) and the dimensionless parameter η_3 (thick line). The latter can be dissected into three stages: a supersonic expansion stage when the PWN is bounded by a shock (dotted section), in unsteady transition when undergoing reverberation with the supernova reverse shock (dashed section), and subsonic expansion (solid section). The parameters adopted in this simulation is: maximum spin-down luminosity $L_0 = 5 \times 10^{38}$ ergs/s, spin-down time $\tau = 600$ yrs, supernova explosion energy of $E_0 = 10^{51}$ ergs and ISM density of 10^{-24} g/cm³. For details, see van der Swaluw et al. (2001).

than a factor of 2 judging from Figure 7.1. In the same table we also list the initial spin periods (P'_0) derived for 4 pulsars using braking index measurements.

7.4 Discussion

We have demonstrated a new method for inferring the initial spin rates of pulsars residing in composite supernova remnants. This method uses the ratio of the plerion radius and the radius of the supernova shell, so we dub it as the ‘radius method’. Given that typical plerions and supernova remnants are expected to live for $10^3 - 10^4$ years, we expect that future observations will increase the population to which the radius method can be applied.

This method does not require a knowledge of parameters like the density and magnetic field strength of the ISM, or the distance and age of the SNR. However, for the method to apply, the observed PWN has to be in the subsonic stage of its evolution. If this is not the case, the method systematically over-estimates the initial spin rate (see below). Uncertainties in E_0 , η_3 and Ω_t introduce errors of order unity, as will a deviation from pure spherical symmetry. A more important uncertainty of this new method concerns the influence of synchrotron radiative losses in the plerion, as parametrized by η_1 . We tend to under-estimate the initial spin-rate by ignoring these losses, putting $\eta_1 = 1$. We will illustrate the effect of these uncertainties by considering the 4 systems in Table 7.1, which have known central pulsars, and independent estimates for the initial periods P'_0 based on measurements of the pulsar braking index.

Among these systems, Vela is the oldest and should have entered the subsonic expansion stage. The fact that the Vela pulsar is displaced from the center of the plerion also testifies in favor of an old age. Our method over-estimates Vela’s spin-down energy by a factor of 2 (or even more if the actual η_3 at subsonic stage is smaller than 1.02, see Fig. 7.1) for the stated choice of parameters. It is difficult to pin-down the actual reason for this discrepancy. We give three possible parameter changes which lead to a similar initial spin period for Vela as derived by Lyne et al.(1996): (1) the supernova explosion could be half as energetic as assumed here, (2) the pulsar may be 15 kyr old, and (3) the braking index is as high as 2.4.

The remaining two systems, G11.2 – 0.3 and G320.4 – 1.2, are young (~ 1.5 kyr). Their plerions could still be in the supersonic (free) expansion stage during which the ratio $R_{\text{PWN}}/R_{\text{SNR}}$ should exceed the value in equation 7.4 (see Fig. 7.1 and §2 in van der Swaluw *et al.* 2001). We expect the effective value of η_3

in these systems to be of order, or higher than 1.02, the theoretical maximum value for η_3 during the subsonic expansion stage. For example, taking $\eta_3 = 2$ we find $P_0 = 63$ ms for $G11.2 - 0.3$. A similar correction may have to be applied to $G29.7 - 0.3$ (Kes 75).

In contrast to the systems discussed above, SNR 0540 – 69.3 is the only case in which the spin-down energy is significantly under-estimated for our choice of parameters. The plerion in SNR 0540 – 69.3 is too small if the pulsar was indeed born with an initial spin of 39 ms. Manchester *et al.* (1993) have argued that the radiative loss in this system has reduced the total energy stored in the plerionic magnetic field and relativistic electrons to a mere 4% of the integrated spin-down luminosity of the pulsar. Taking $\eta_1 = 0.04$ we recover a 39 ms initial period, with a value of $\eta_3 = 1.3$. This value of η_3 is reasonable because SNR 0540 – 69.3 is only 760 years old. None of the other 3 systems discussed here requires strong synchrotron losses in the plerion, which makes SNR 0540 – 69.3 unique. Among the associated pulsars, PSR 0540 – 69 is not outstanding either in its surface magnetic field strength or in its spin-down rate. It is likely born the fastest, though not by a large margin.

Along the same line, Atoyan (1999) have argued that in Crab, strong synchrotron losses in its past can account for the observed flat spectra of the radio electrons in the plerion. Currently, the Crab suffers a synchrotron loss of 10% of the spin-down luminosity in the X-ray band, the highest in the sample of Seward & Wang (1988).

Although the effect of radiative losses on the reliability of our results remain unclear, we briefly explore the implications of these results. Our sample (Table 7.1) is likely biased towards fast spinners, which produce plerions that are easier to detect. Even so, all pulsars in our sample seem to be born spinning much below the break-up rate. Moreover, their initial spin-periods do not cluster around $\sim 5 - 10$ ms, a signature of rapid spin-down by the gravitationally radiating Rossby-waves which occur immediately after the supernova collapse (Andersson *et al.* 2000, Wu *et al.* 2001). The long initial periods we find imply an effective angular momentum coupling between the core and envelope of neutron star progenitors until late into their evolution. The scattering in the initial periods could either reflect a different decoupling time in different stars, or a stochastic process that gives rise to the final angular momentum in the neutron star, such as an off-centered kick during the collapse (Spruit & Phinney 1998).

| Supernova Designation | Plerion | | | Pulsar | | | age (kyr) |
|--------------------------|-------------------------------------|-----------------|--------------------|-------------------------------|-------------------------------|------|--------------|
| | $R_{\text{pwn}}/R_{\text{snr}}$ | F_0 (in msec) | P_t (in msec) | P_t (in msec) | P'_0 (in msec) | | |
| G0.9 + 0.1 | 0.25(Helfand & Becker 1987) | 43 | - | - | - | - | - |
| G16.7 + 0.1 | 0.25(Helfand <i>et al.</i> 1989) | 43 | - | - | - | - | - |
| G29.7 - 0.3 | 0.16(Becker & Helfand 1984) | 82 | 325[PSR 1846-0258] | - | - | 0.7 | 0.7 |
| G34.7 - 0.4 | 0.07(Frail <i>et al.</i> 1996) | 197 | 267[PSR 1853+01] | - | - | - | - |
| G293.8 + 0.6 | 0.25(Whiteoak & Green 1996) | 43 | - | - | - | - | - |
| G322.5 - 0.1 | 0.27(Whiteoak 1992) | 39 | - | - | - | - | - |
| G326.3 - 1.8 | 0.28(Kassim <i>et al.</i> 1993) | 37 | - | - | - | - | - |
| G327.1 - 1.1 | 0.25(Sun <i>et al.</i> 1999) | 43 | - | - | - | - | - |
| G351.2 + 0.1 | 0.05(Becker & Helfand 1988) | 484 | - | - | - | - | - |
| G263.9 - 3.3 | 0.24(Milne 1980) | 41 | 89[Vela] | 52(Lyne <i>et al.</i> 1996) | 52(Lyne <i>et al.</i> 1996) | 11.3 | 11.3 |
| G11.2 - 0.3* | 0.15(Vasisht <i>et al.</i> 1996) | 53 | 65 | 63(Torii <i>et al.</i> 1999) | 63(Torii <i>et al.</i> 1999) | 1.6 | 1.6 |
| G320.4 - 1.2* | 0.17(Seward <i>et al.</i> 1983) | 69 | 150[PSR B1509-58] | 63(Kaspi <i>et al.</i> 1994) | 63(Kaspi <i>et al.</i> 1994) | 1.5 | 1.5 |
| SNR0540 - 69.3 | 0.08(Manchester <i>et al.</i> 1993) | 49 | 50.3[PSR 0540-69] | 39(Deeter <i>et al.</i> [10]) | 39(Deeter <i>et al.</i> [10]) | 0.8 | 0.8 |

Table 7.1: List of composite remnants: F_0 is the initial spin period which results from using the method described in this Chapter, P_t is the current spin period of systems which have an identified pulsar and P'_0 is the calculated initial spin period by using the braking index. $R_{\text{pwn}}/R_{\text{snr}}$, initial period

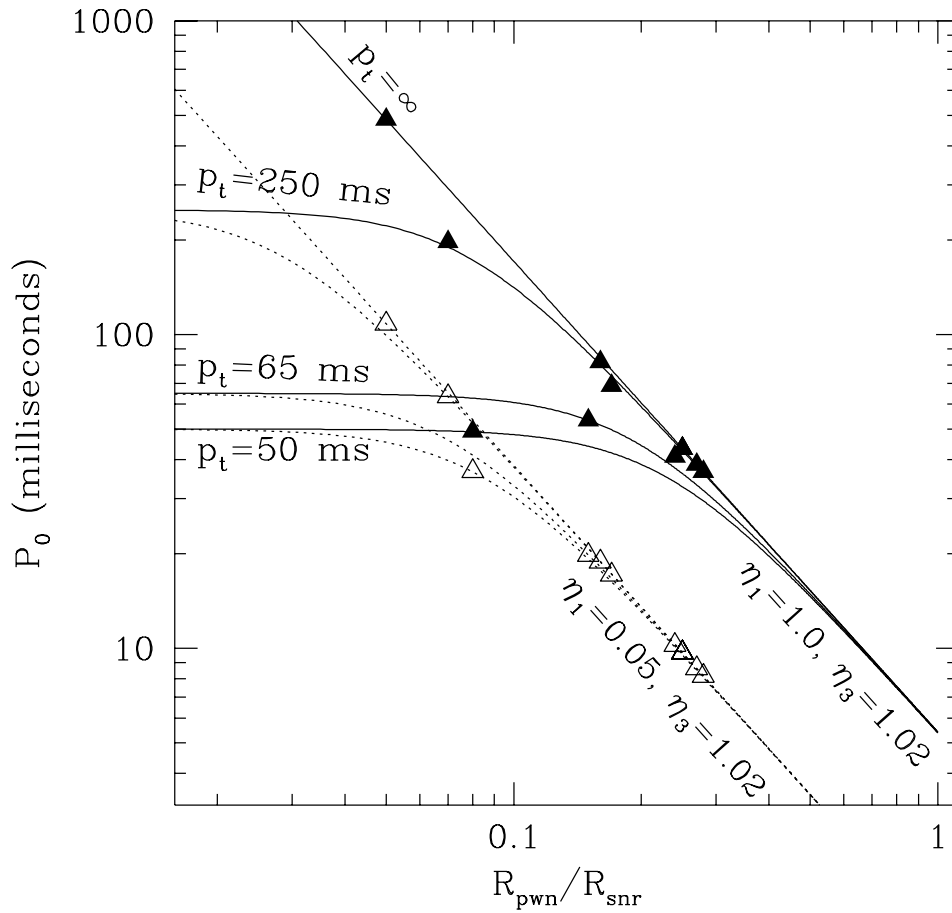


Figure 7.2: Initial spin periods inferred from the ratio $R_{\text{pwn}}/R_{\text{snr}}$ using equation 7.6. When assuming no radiative loss ($\eta_1 = 1$), we obtain solutions as depicted by the family of solid lines, with different lines applicable for different current spin periods, P_t . The family of dashed lines are for $\eta_1 = 0.05$. Filled and open triangles represent systems listed in Table 7.1 for $\eta_1 = 1$ and $\eta_1 = 0.05$, respectively. When $P_0 \leq 4$ ms, the initial rotational energy of the pulsar exceeds the total mechanical energy in the SNR itself. Equation 7.6 fails and the SNR may be blown away by the PWN. None of the systems we examined lies close to this limit.

Bibliography

- [1] Andersson, N., Jones, D. I., Kokkotas, K. D. & Stergioulas, N. 2000, ApJ , 534, L75
- [2] Andrews, M. D., Basart, J. P., Lamb, R. C. & Becker, R. H. 1983, ApJ, 266, 684
- [3] Atoyan, A. M. 1999, AAP, 346, L49
- [4] Bhattacharya, D. & Srinivasan, G. 1987, High Energy Phenomena Around Collapsed Stars, 235
- [5] Becker, R. H. & Helfand, D. J. 1984, ApJ, 283, 154
- [6] Becker, R. H. & Helfand, D. J. 1988, Astron. J., 95, 883
- [7] Blandford, R. & Eichler, D. 1987, Phys. Rep., 154, 1
- [8] Caraveo, P. A. & Mignani, R. P. 1999, AAP, 344, 367
- [9] Chevalier, R.A., Fransson, C., 1992, ApJ, 395, 540
- [10] Deeter, J. E., Nagase, F. & Boynton, P. E. 1999, ApJ, 512, 300
- [11] Emmering, R. T. & Chevalier, R. A. 1989, ApJ, 345, 931
- [12] Frail, D. A., Giacani, E. B., Goss, W. M. & Dubner, G. 1996, ApJ , 464, L165
- [13] Green, D. A. & Scheuer, P. A. G. 1992, MNRAS, 258, 833
- [14] Haensel, P., Salgado, M., & Bonazzola, S. 1995, AAP, 296, 745
- [15] Harrison, E. R. & Tademaru, E. 1975, ApJ, 201, 447

-
- [16] Heger, A., Langer, N. & Woosley, S. E. 2000, *ApJ*, 528, 368
- [17] Helfand, D. J. & Becker, R. H. 1987, *ApJ*, 314, 203
- [18] Helfand, D. J., Velusamy, T., Becker, R. H. & Lockman, F. J. 1989, *ApJ*, 341, 151
- [19] Kassim, N. E., Hertz, P. & Weiler, K. W. 1993, *ApJ*, 419, 733
- [20] Kaspi, V. M., Manchester, R. N., Siegman, B., Johnston, S. & Lyne, A. G. 1994, *ApJ*, 422, L83
- [21] Lai, D. & Goldreich, P. 2000, *ApJ*, 535, 402
- [22] Lai, D., Chernoff, D. F. & Cordes, J. M. 2001, *ApJ*, 549, 1111
- [23] Lindblom, L., Owen, B. J. & Morsink, S. M. 1998, *Physical Review Letters*, 80, 4843
- [24] Lorimer, D. R., Bailes, M., Dewey, R. J. & Harrison, P. A. 1993, *MNRAS*, 263, 403
- [25] Lyne, A. G., Pritchard, R. S. & Graham-Smith, F. 1993, *MNRAS*, 265, 1003
- [26] Lyne, A. G., Pritchard, R. S., Graham-Smith, F. & Camilo, F. 1996, *Nature*, 381, 497
- [27] Manchester, R. N., Staveley-Smith, L. & Kesteven, M. J. 1993, *ApJ*, 411, 756
- [28] Marshall, F. E., Gotthelf, E. V., Zhang, W., Middleditch, J. & Wang, Q. D. 1998, *ApJ*, 499, L179
- [29] McKee, C.F. & Truelove, *Phys.Rep.* 256,157
- [30] Milne, D. K. 1980, *AAP*, 81, 293
- [31] Narayan, R. 1987, *ApJ*, 319, 162
- [32] Pavlov, G. G., Sanwal, D., Garmire, G. P., Zavlin, V. E., Burwitz, V. & Dodson, R. G. 2000, *American Astronomical Society Meeting*, 196, 3704
- [33] Phinney, E. S. & Blandford, R. D. 1981, *MNRAS*, 194, 137

- [34] Rybicki, G. B., Lightman, A. P. 1979, *Radiative Processes in Astrophysics*, John Wiley & Sons
- [35] Reynolds, S.P., and Chevalier, R.A., 1984, *ApJ*, 278, 630
- [36] Sedov L.I., 1959, *Similarity and Dimensional Methods in Mechanics*, Academic, New York
- [37] Seward, F. D., Harnden, F. R., Murdin, P. & Clark, D. H. 1983, *ApJ*, 267, 69
- [38] Seward, F. D. & Wang, Z. R. 1988, *ApJ*, 332, 199
- [39] Spruit, H. C. & Phinney, E. S. 1998, *Nature*, 393, 139
- [40] Srinivasan, G., Dwarakanath, K. S. & Bhattacharya, D. 1984, *Journal of Astrophysics and Astronomy*, 5, 403
- [41] Sun, M., Wang, Z. & Chen, Y. 1999, *ApJ*, 511, 274
- [42] Tóth, G. & Odstrčil, 1996 *J. Comp. Phys.* 128, 82
- [43] Torii, K., Tsunemi, H., Dotani, T., Mitsuda, K., Kawai, N., Kinugasa, K., Saito, Y. & Shibata, S. 1999, *ApJ* , 523, L69
- [44] van der Swaluw, E. Achterberg, A. ,Gallant, Y. A. & Tóth, G. 2001, *astro-ph/0012440*, submitted to *AAP*
- [45] Vasisht, G., Aoki, T., Dotani, T., Kulkarni, S. R. & Nagase, F. 1996, *ApJ* , 456, L59
- [46] Vivekanand, M. & Narayan, R. 1981, *Journal of Astrophysics and Astronomy*, 2, 315
- [47] Weiler K. W.& Panagia N., 1978, *AAP* 70, 419
- [48] Whiteoak, J. B. Z. 1992, *MNRAS*, 256, 121
- [49] Whiteoak, J. B. Z. & Green, A. J. 1996, *AAPs*, 118, 329
- [50] Woltjer L., Salvati M.,Pacini F., Bandiera R., 1997 *A&A* 325, 295
- [51] Wu, Y., Matzner, C. D., Arras, P. 2001, *ApJ*, 549, 1011

Chapter 8

Nederlandse Samenvatting

8.1 Supernova's en supernova restanten

Supernova's zijn een van de meest energetische gebeurtenissen in ons heelal. Dit blijkt alleen al uit het feit dat een aantal supernovae in ons eigen melkwegstelsel met het blote oog is waargenomen, een indicatie van de enorme hoeveelheid energie die vrijgemaakt wordt in zo'n proces. Dit proefschrift, *Supernova Remnants, Pulsar Wind Nebulae and their Interacion*, gaat in essentie over de processen die zich afspelen na deze kosmische explosie.

Er zijn twee verschillende mechanismen, die tot een supernova explosie kunnen leiden. In het eerste geval markeert een supernova explosie het einde van het leven van een zware ster: de brandstof van de ster is uitgeput, en de ster stort onder zijn eigen gewicht in. Bij deze ineenstorting wordt er een enorme hoeveelheid energie vrijgemaakt, die uiteindelijk de opgebrande ster doet exploderen. In het tweede geval is het exploderende object een witte dwerg. Deze kleine, compacte sterren zijn de fossielen van sterren die nog niet opgebrand zijn, maar waar de temperatuur te laag bleef om de kernfusie van de aanwezige koolstof en zuurstof op te starten. In die gevallen waarbij de witte dwerg deel uit maakt van een dubbelster systeem, kan er in dit soort objecten ook een explosie veroorzaakt worden. Dit gebeurt als de begeleidende ster massa overdraagt naar de witte dwerg, waardoor de temperatuur in de witte dwerg zodanig wordt verhoogd dat de koolstof en de zuurstof in deze objecten explosief ontvlamt.

Voor beide mechanismen geldt dat de materie van de exploderende ster helemaal of gedeeltelijk wordt weggeslingerd. Dit resulteert in een expanderende bol heet gas in de interstellaire ruimte, *een supernova restant*. De expansie zal het

supernova restant langzaam laten afkoelen, in een periode die duizenden jaren beslaat. Het verschil tussen beiden mechanismen zit hem in de mogelijkheid tot het vormen van een compact object: een neutronen ster of zelfs een zwart gat. Dit gebeurt alleen bij de explosies die het leven van een zware ster beëindigen. Het compacte object bestaat uit de kern van de ster, waarvan het materiaal niet is weggeslingerd, maar door de eigen zwaartekracht wordt bijeengehouden. Het gevormde compacte object kan een *neutronenster* zijn, met een massa van de Zon, en een straal van slechts 10 kilometer. Een neutronenster kan zich manifesteren als een pulserende radiobron aan de hemel, een *pulsar*. Een meer exotisch eindproduct is een zwart gat. Dat geval zal echter niet worden beschouwd in dit proefschrift.

8.2 Pulsars en pulsar winden

Een pulsar is een snel roterende neutronenster met een enorm hoog magneetveld. Dit magneetveld heeft een remmende werking op de rotatiesnelheid van de pulsar, waardoor de *rotatie-energie* van de pulsar continue zal afnemen. Een deel van de verloren rotatie-energie wordt, via een ingewikkeld en nog steeds onbegrepen proces, omgezet in een *pulsar wind*. Deze pulsar wind bestaat uit hoog energetische deeltjes, voornamelijk electronen en positronen, die zich met vrijwel de snelheid van het licht voortbewegen.

Op deze manier injecteert de pulsar een deel van zijn rotatie-energie in de bel heet gas van het supernova restant. Algemeen wordt aangenomen dat deze extra geïnjecteerde energie slechts een fractie is van de totale explosie-energie die al in het restant aanwezig is. Hierdoor zal de pulsar wind weliswaar het supernova restant niet wegblazen, maar wel een soort van vingerafdruk achterlaten in het restant. Deze vingerafdruk manifesteert zich als een *pulsar wind nevel*: de pulsar wind *blaast* een bel van *extreem heet* gas in het relatief koelere gas van de supernova restant.

8.3 De interactie tussen een pulsar wind nevel en een supernova restant

Het eerste hoofdonderwerp van dit proefschrift is de interactie die ontstaat tussen een pulsar wind nevel, en het omringende supernova restant na de supernova explosie. Bij explosies waar de weggeslingerde materie van de ster niet sferisch

symmetrisch is verdeeld, krijgt de pulsar bij zijn geboorte een snelheid, en wel zodanig dat de *totale* impuls aanwezig in het systeem, de impuls van neutronen ster en de weggeslingerde materie, behouden blijft. Door dit effect zijn er ruwweg twee gevallen te onderscheiden in de interactie tussen een pulsar wind nevel en een supernova restant.

In het eerste geval is het supernova restant nog heel erg jong, maximaal een paar honderd jaar. In dit geval bevindt de pulsar zich nog ruwweg in het midden van het supernova restant bevinden, op de plek waar destijds de explosie plaatsvond. De door de pulsar wind gevormde nevel bevindt zich daarom vrijwel in het midden van het supernova restant.

In het tweede geval, dat optreedt als de snelheid van de pulsar voldoende groot is, heeft de pulsar zich al verplaatst naar de rand van het supernova restant. De pulsar heeft in feite de rand van het uitdijende restant ingehaald.

In dit proefschrift worden, door middel van hydrodynamische simulaties, de interacties tussen de pulsar wind nevel en het supernova restant in beide gevallen beschreven. In het eerste geval tonen deze berekeningen duidelijk de koppeling die aanwezig is tussen de verschillende fasen in de evolutie van het supernova restant, en de ontwikkeling van de pulsar wind nevel. In het tweede geval tonen de berekeningen hoe de pulsar door de schil van het supernova restant heenbreekt, waarna de pulsar (inclusief de pulsar wind nevel) zich door de interstellaire ruimte heen zal gaan bewegen.

8.4 Supernova restanten: kosmische deeltjesversnellers

Het tweede hoofdonderwerp van dit proefschrift is de deeltjesversnelling rond de schokken die de rand van een supernova restant, en van een pulsar wind markeren. Een schok is een overgangslaag, die zich door een gas heen beweegt, en daarbij het instromende gas comprimeert, door drukkrachten wordt versnelt en door wrijving wordt verhit. In de jaren '70 ontdekten een aantal onderzoekers onafhankelijk van elkaar dat een schok kan fungeren als een deeltjesversneller. Een schok rond een supernova restant kan een geladen deeltje versnellen tot een typische energie van $\sim 10^{14-15}$ eV. Ter vergelijking, de door mensen gemaakte versnellers op een instituut als CERN komen tot een energie van $\sim 10^{12}$ eV.

Opgemerkt dient te worden dat het mechanisme voor het versnellen van deeltjes in bovengenoemde schokken, en in Aardse deeltjesversnellers, compleet verschillend is.

Net zoals rond een pulsar is er aan de randen van een supernova restant ook een magneetveld aanwezig. De veldsterkte is weliswaar vele malen zwakker: het gaat hier om het interstellair magnetisch veld van slechts een micro-Gauss. Door de aanwezigheid van dit zwakke magneetveld stralen de versnelde deeltjes een deel van hun bij de schok gekregen energie weg. Deze straling wordt synchrotron straling genoemd, en treedt altijd op als een hoog energetisch deeltje zich beweegt in een magneetveld.

In het proefschrift worden resultaten getoond die zogenaamde *synchrotron kaarten* leveren. Deze kaarten tonen een supernova restant, zoals die waargenomen zou worden op frequenties die corresponderen met Röntgen straling. De berekeningen die gedaan zijn om deze kaarten te produceren combineren de resultaten van een hydrodynamische berekening, die de dynamische evolutie van een supernova restant volgt, met een code die de versnelling en het transport van deeltjes in en rond het restant simultaan berekent. Bij onze berekeningen heeft de dynamica van deze versnelde deeltjes echter geen invloed op de hydrodynamische berekeningen, een met de huidige stand van de reken-techniek noozakelijke vereenvoudiging.

8.5 Ter afsluiting

Het huidige proefschrift biedt een aantal technieken die gebruikt kunnen worden om systemen als supernova restanten en pulsar wind nevels te bestuderen vanuit theoretisch oogpunt. Alhoewel het huidige beeld dat wetenschappers hebben van supernova restanten aardig coherent begint te worden, is een dergelijke situatie voor pulsar winden, en de daarmee geassocieerde nevels, nog lang niet bereikt. Ik vermoed daarom dat onderzoek van deze systemen in de toekomst nog de nodige verassingingen zal opleveren.

Curriculum vitae

Ik ben geboren op 4 augustus 1971 te 's-Hertogenbosch. Aan het Maurick College in Vught heb ik acht jaar doorgebracht, waar ik eerst HAVO en vervolgens VWO doorlopen heb. In 1991 ben ik begonnen aan de studie sterrenkunde aan de Universiteit Utrecht. Mijn afstudeeronderzoek heb ik echter aan de Universiteit in Leiden gedaan, onder leiding van Prof. Dr. Vincent Icke. Het onderzoek handelde over de fluctuaties in de achtergrondstraling van het heelal.

Begin 1997 ben ik als promovendus begonnen bij Prof. Dr. Bram Achterberg. Tijdens mijn promotie heb ik diverse workshops and conferenties bezocht. Tijdens de workshop *The relationship between neutron stars and supernova remnants (1998)* heb ik voor de eerste keer mijn werk kunnen presenteren aan vakgenoten. Daarna heb ik diverse keren voordrachten gegeven tijdens workshops van *The AstroPlasmaPhysics TMR Netwerk*, vergaderingen van het *M(assaal) P(arallel) R(eken) project* en colloquia.

Ik ben op 1 februari 2001 begonnen als onderzoeker op het Dublin Institute of Advanced Studies onder begeleiding van Prof. Dr. Luke O'C Drury.

Dankwoord

Na vier jaar werken is er dan toch een proefschrift uit komen rollen. Het werk hierin is zeker niet allemaal alleen gedaan, en ik wil een aantal mensen bedanken voor steun, hulp, advies en bijdragen.

Eerst zijn er een aantal mensen, die een persoonlijk *dank-je-wel* verdiend hebben:

Bram Achterberg, jou wil ik als eerste bedanken. Ik heb enorm veel van jou geleerd in de afgelopen vier jaar. Ik beschouw het als een enorme gunst om onder jouw begeleiding een proefschrift te hebben mogen schrijven. Bovendien ging dit alles gepaard met een enorme prettige samenwerking, waarbij we ook veel lol hebben gehad.

Yves Gallant, thank you for all the discussions we have had in the last four years. I have learnt a lot from you getting into the field of SNRs and PWNe.

Luke Drury, thanks a lot for inviting me twice at the Dublin Institute of Advanced Studies (DIAS) in Dublin and the several interesting discussions we have had. It has been a pleasure to finish my thesis and continue as a postdoctoral researcher at DIAS!

Alexandre Marcowith, thanks a lot for all the interesting discussions we have had (and will continue to have) on hydrodynamics and SDEs. It has been a pleasure to work with you!

Yanqin Wu, while you were in Utrecht, we started to chat about initial spin periods of pulsars. After a few months there was another chapter for my thesis! Thanks for the nice collaboration.

John Kirk, thank you for inviting me in Heidelberg for a week to discuss hydrodynamics and SDEs. It was an inspiring week.

Rony Keppens, bedankt voor de assistentie bij het gebruik van de *Versatile Advection Code*. Dankzij jouw hulp is hoofdstuk 4 toch nog opgenomen in het proefschrift: twee dagen werk op Rijnhuizen, en het was voor elkaar!

Het gehele proefschrift maakt gebruik van de *Versatile Advection Code*. De *Versatile Advection Code* is voortgekomen uit het M(assaal) P(arallel) R(eken) project. Graag wil ik met name Hans Goedbloed en Gábor Tóth bedanken voor de moeite die ze genomen hebben om mij te betrekken bij de MPR activiteiten. Ik heb een goede herinnering aan de MPR vergaderingen.

Verder wil ik Wim Hermsen, Ferdi Hulleman, Vincent Icke, Marten van Kerkwijk, Lucien Kuiper Jan Kuipers, Richard Strom, Frank Verbunt, en Jacco Vink bedanken die allemaal op een bepaalde manier hebben bijgedragen aan de totstandkoming van dit proefschrift.

Furthermore I wish to thank the following people with whom I have had interesting discussions in the last four years: John Dickel, Turlough Downes, Sam Falle, Bryan Gaensler, Kurt van der Heyden, Norbert Langer. Don Melrose, Etienne Parizot, Shinpei Shibata, and Ben Stappers.